TECHNISCHE UNIVERSITÄT WIEN
Vienna University of Technology

MASTER THESIS

# Mapping of stoichiometric inhomogeneities in field-stressed $Li_{(0.29\pm\delta)}La_{0.57}TiO_3$ electrolytes

carried out for the purpose of obtaining the degree of Master of Science (MSc),

submitted at TU Wien, Faculty of Technical Chemistry,

by

**Lisa LAA**

Mat.Nr.: 11771113

under the supervision of

Univ.Prof. Dipl.-Ing. Dr.techn. Andreas Limbeck

Univ.Ass. Dipl.-Ing. Dr.rer.nat. Andreas Nenning

Univ.Prof. Dipl.-Phys. Dr.rer.nat. Jürgen Fleig

Institute of Chemical Technologies and Analytics, E164

# Abstract

The intermittent nature of renewable electricity production as well as electro-mobility requires electrochemical storage of electrical energy. Lithium-ion batteries (LIBs) are the dominant technology due to their high energy densities and low self-discharge. However, liquid electrolytes, which are used in commercial LIBs, are flammable and extremely sensitive towards humidity. A promising alternative is the perovskite-type solid electrolyte $Li_{(0.29\pm\delta)}La_{0.57}TiO_3$ (LLTO) that can be applied to all-solid-state LIBs. The exact voltage stability limit and decomposition kinetics of this material are, however, unknown and the mapping of stoichiometric inhomogeneities in field-stressed LLTO is a powerful tool for a better understanding of these mechanisms.

In this thesis, the stoichiometry of non-polarized and polarized LLTO electrolytes was investigated by laser ablation inductively coupled plasma mass spectroscopy (LA-ICP-MS). Therefore, qualitative measurements of LLTO were performed and elemental distribution images were created. For the study of stochiometric changes during polarization, quantification of lithium (Li) is necessary, so matrix-matched standards were prepared. Quantitative LA-ICP-MS measurements of under different pressures polarized LLTO substrates were conducted. Moreover, various voltages (2.5 V – 8 V) were applied to LLTO substrates, subsequently investigating the effects using quantitative LA-ICP-MS analysis.

The conducted measurements showed an excess of Li at the surface-near region of the investigated LLTO samples, irrespective of the applied field stress. The enrichment in this area could be removed by pre-ablation or leaching in an ultrasonic bath. In qualitative measurements of polarized LLTO, a local Li depletion beneath the anode is observed. Furthermore, pressed pellets with various quantities of lithium oxide ($Li_2O$), lanthanum oxide ($La_2O_3$) and titanium oxide ($TiO_2$) were found to be suitable for quantification. Quantitative measurements indicated that atmospheric pressure polarization results in a confined lithium accumulation at the cathodic terminal. In comparison, polarization in a high vacuum ($10^{-5}$ mbar) led to a non-detectable lithium enrichment in a larger area surrounding the cathode. Furthermore, it was found that there is a direct correlation between the height of the applied voltage and the depth of the propagation in the depletion zone.

The obtained results help to increase the knowledge about ion conductivity which is decisive for the application of LLTO as a solid electrolyte.

# Kurzfassung

Da die Gewinnung von elektrischer Energie durch erneuerbare Energiequellen unregelmäßig erfolgt und häufig mit Energiespitzen verbunden ist, ergibt sich die Notwendigkeit einer möglichen elektrochemischen Energiespeicherung der elektrischen Energie. Zusätzlich ist dies auch in Bezug auf Energiespeicherung für Elektromobilität von Interesse. Aufgrund ihrer hohen Energiedichten und geringen Selbstentladung sind Lithium-Ionen-Sekundärbatterien derzeit die vorherrschende Technologie im Bereich der elektrochemischen Speicherung. Jedoch sind flüssige Elektrolyte, welche in kommerziell erhältlichen Lithium-Ionen-Sekundärbatterien verwendet werden, leicht entzündlich und feuchtigkeitsempfindlich. Eine vielversprechende Alternative für konventionelle organische Elektrolyte sind Perowskit Feststoffelektrolyte $Li_{(0.29\pm\delta)}La_{0.57}TiO_3$ (LLTO). Der genaue Spannungsstabilitätsbereich und die Zersetzungskinetik des Materials sind allerding experimentell noch unbekannt. Das Abbilden von stöchiometrischen Inhomogenitäten von feldbelastetem LLTO stellt eine effektive Methode da, um ein besseres Verständnis dieser Mechanismen zu erlangen.

In dieser Diplomarbeit wird die Stöchiometrie von unbelasteten sowie von feldbelasteten LLTO-Substraten durch Massenspektrometrie mit induktiv gekoppeltem Plasma (engl. ICP-MS) untersucht. Der Probenabtrag bei den festen LLTO-Substraten erfolgte über Laser Ablation (engl. LA). Um die LLTO-Substrate zu analysieren, wurden qualitative Messungen durchgeführt und daraus Elementverteilungsimages erstellt. Für die Untersuchung der stöchiometrischen Veränderungen, welche durch Anlegen von Spannung entstehen, ist die Quantifizierung von Lithium (Li) unerlässlich, deshalb wurden matrix-angepasste Standards hergestellt. Quantitative LA-ICP-MS Messungen von unterschiedlich feldbelasteten LLTO-Substraten und von in unterschiedlichen Atmosphären feldbelasteten LLTO-Substraten wurden durchgeführt.

Die durchgeführten Messungen zeigten eine prinzipielle Anreicherung an Lithium in oberflächennahen Schichten der untersuchten LLTO-Substrate. Dieser Lithiumüberschuss konnte durch Vorbehandlung in einem Ultraschallbad oder durch vorangegangene Ablation reduziert beziehungsweise entfernt werden. In den qualitativen Messungen von feldbelasteten LLTO-Substraten wurde eine Li-Verarmung unterhalb der Anode festgestellt. Weiters wurde herausgefunden, dass gepresste Pellets mit unterschiedlichen Mengen an Lithiumoxid ($Li_2O$), Lanthanoxid ($La_2O_3$) und Titandioxid ($TiO_2$) für die Quantifizierung geeignet sind. Quantitative Messungen zeigten, dass Feldbelastung in Atmosphärendruck zu einer örtlich begrenzten Lithiumakkumulierung im Bereich der Kathode führte, während sich Feldbelastung unter reduziertem Druck ($10^{-5}$ mbar) in Form einer geringeren bis nicht-detektierbaren Li-Anreicherung in diesem Bereich auswirkt. Schlussendlich wurde gezeigt, dass die Höhe der angelegten Spannung die Ausbreitungstiefe der Lithiumverarmungszone unterhalb der Anode beeinflusst.

Die erhaltenen Ergebnisse helfen das Wissen über die ionische Leitfähigkeit in LLTO, welches ausschlaggebend für die Anwendung von LLTO als Feststoffelektrolyt ist, zu erweitern.

# Danksagung

Während der Anfänge meiner schulischen Ausbildung, geprägt durch eher holprige Leistungen, konnte ich mir nicht vorstellen, je ein Studium zu beginnen, geschweige denn abzuschließen. Nichtsdestotrotz hat sich meine Einstellung im Laufe der Zeit geändert und ich bin nach meiner Matura voller Vorfreude in das Studium gestartet. Die Motivation und Freude waren an manchen Tagen größer, an anderen Tagen wiederum kaum erkennbar, jedoch bis zum jetzigen Zeitpunkt eigentlich immer vorhanden. Dies ist auf einige wenige Punkte zurückzuführen, und zwar auf das Interesse an Naturwissenschaften sowie auf einige Menschen, mit denen ich während dieser Zeit in Kontakt gestanden bin. An dieser Stelle ist es daher an der Zeit, mich bei einigen Personen zu bedanken, ohne die ich nicht so weit gekommen wäre.

An erster Stelle möchte ich mich bei Andreas Limbeck bedanken, der es mir überhaupt erst ermöglicht hat, in seiner Forschungsgruppe zu arbeiten und Interesse an der Thematik zu entwickeln. Bereits vor meiner Diplomarbeit hatte ich unter ihm die Möglichkeit, mich im Zuge eines Wahlpraktikums und einer Bachelorarbeit mit anorganischer Spurenanalytik zu beschäftigen. Durch die Arbeit konnte ich mich nicht nur fachlich, sondern auch persönlich weiterentwickeln.

Außerdem möchte ich mich bei Andreas Nenning und Jürgen Fleig für die Möglichkeit bedanken, meine Diplomarbeit im Zuge einer Kooperation zwischen zwei Forschungsgruppen zu absolvieren. Die Zusammenarbeit hat immer hervorragend funktioniert, sei es bei der Herstellung der Proben, beim Besprechen der Ergebnisse oder bei teils langwierigen Erklärungen elektrochemischer Prozesse.

Neben den bereits genannten Personen möchte ich mich auch bei allen anderen Mitgliedern beider Forschungsgruppen für die Unterstützung bedanken. Die manchmal mehr und manchmal weniger produktive, dafür umso amüsantere Zeit mit den zeitgleich arbeitenden DiplomandInnen Michaela Porkert, Veronika Zeller, Marlene Nadvornik, Nicole Rosza und Alexander Holzer möchte ich besonders hervorheben.

Mein Dank gebührt auch meinen Studienkolleginnen Sabine Kitting-Muhr, Lara Maltrovsky und Stephanie Krall, die während des Studiums zu Freunden wurden. Neben den gemeinsamen Stunden in diversen Laborübungen, bleiben mir die gemeinsamen sportlichen Aktivitäten (Laufeinheiten, Wanderungen und Tennistrainings) sowie etliche Unterhaltungen in Erinnerung, während denen ich universitären Stress ausblenden konnte. An dieser Stelle möchte ich auch nicht auf meine ehemalige Schulkollegin und Internatszimmermitbewohnerin Raphaela Kirisits vergessen, die mir ebenfalls immer zur Seite stand.

Zu guter Letzt möchte ich mich bei meinen Eltern Eva und Reinhard und bei meinem Bruder Dominik bedanken. Sie haben mich stets unterstützt und standen mir andauernd mit einem offenen Ohr zur Seite. Ohne sie wäre mir ein Studium nicht möglich gewesen.

# Contents

# Index of abbreviations

| | |
|---|---|
| LIB | lithium-ion battery |
| LLTO | lithium lanthanum titanate |
| LA | laser ablation |
| ICP | inductively coupled plasma |
| MS | mass spectrometry |
| Li | lithium |
| $Li_2O$ | lithium oxide |
| $La_2O_3$ | lanthanum(III) oxide |
| $TiO_2$ | titanium(IV) oxide |
| LiSICON | lithium super ionic conductor |
| LLZO | lithium lanthanum zirconium oxide |
| XRD | X-ray diffraction |
| Ca | calcium |
| Sr | strontium |
| Ba | barium |
| t | Goldschmidt tolerance factor |
| $r_A$ | radius of the A cation |
| $r_B$ | radius of the B cation |
| $r_X$ | radius of the X anion |
| La | lanthanum |
| Ti | titanium |
| NMR | nuclear magnetic resonance |
| 3D | three-dimensional |
| VTF | Vogel-Tamman-Fulcher |
| LCO | lithium cobalt oxide |
| LMO | lanthanum manganite |
| NMC | lithium nickel manganese cobalt oxide |
| NCA | lithium nickel cobalt aluminium oxide |

| | |
|---|---|
| EC | ethylene carbonate |
| DMC | dimethyl carbonate |
| DEC | diethyl carbonate |
| EMC | ethyl methyl carbonate |
| PC | propylene carbonate |
| ε | permittivity |
| $LiPF_6$ | lithium hexafluorophosphate |
| HF | hydrogen fluoride |
| ASS | all-solid-state |
| NASICON | sodium super ionic conductor |
| LLZO | lithium lanthanum zirconium oxide |
| LiPON | lithium phosphorus oxynitride |
| Excimer | excited dimer |
| Nd:YAG | neodymium-doped yttrium aluminium garnet |
| IR | infrared |
| KTP | potassium titanyl phosphate |
| LBO | lithium triborate |
| BBO | beta barium borate |
| UV | ultraviolet |
| KrF | krypton fluoride |
| ArF | argon fluoride |
| He | helium |
| Ne | neon |
| RF | radio frequency |
| m/z | mass-to-charge ratio |
| TOF | time-of-flight |
| AC | alternating current |
| DC | direct current |
| SEM | secondary electron multiplier |
| XPS | X-ray photoelectron spectroscopy |

| | |
|---|---|
| SIMS | secondary ion mass spectrometry |
| EDXS | energy-dispersive X-ray spectroscopy |
| CRM | certified reference material |
| DCI | dual concentric injector |
| Pt | platinum |
| Au | gold |
| $Li_2CO_3$ | lithium carbonate |

# 1 Introduction

Today's rapid economic growth is accompanied by high consumption of fossil energy, which has led to environmental pollution problems. To tackle this issue, the use of renewable energy with energy storage as a key component becomes increasingly important. Lithium-ion batteries (LIBs) are the most dominating energy storage devices due to their high energy densities, high power densities, and low self-discharge [1-4].

At present, lithium-ion batteries are mainly based on liquid electrolytes. However, these liquid electrolytes, which are used in commercially available LIBs, are flammable and extremely sensitive towards humidity [1, 5]. Promising alternatives to the liquid organic electrolytes are solid electrolytes that can be applied to all-solid-state LIBs. Different solid electrolytes have been investigated in greater detail, such as Lithium Super Ionic Conductor ($Li_{14}Zn(GeO_4)_4$, LiSICON) [6] or garnet-type solid electrolytes ($Li_7La_3Zr_2O_{12}$, LLZO) [7, 8].

Besides the above mentioned investigated solid electrolytes, the perovskite-type lithium lanthanum titanate $Li_{3x}La_{(2/3)-x}TiO_3$ (LLTO) can also be applied to all-solid-state LIBs. This material has attracted much attention due to its high bulk ionic conductivity of $10^{-3}$ S cm$^{-1}$ at room temperature [9-11]. LLTO was reported in 1987 by Belous et al. [12] and in 1993 by Inaguma et al. [10]. In addition to its high ionic conductivity, LLTO has excellent electrochemical and physical properties. The negligible electronic conductivity, the large electrochemical stability window, and thermal stability makes LLTO an appropriate candidate for all-solid-state LIBs [13, 14]. Besides the strengths of this material, LLTO, however, possesses new challenges in the application as solid electrolyte. Easily reducible $Ti^{4+}$ ions in LLTO can lead to increased electronic conductivity and, hence, to a short circuit of the LIB [15, 16]. In crystalline LLTO the lithium-ion conductivity is limited through the grain boundaries, which often have an ionic conductivity below $10^{-5}$ S cm$^{-1}$ at room temperature [17, 18], and must be further optimized for application [19].

Structural properties of LLTO are well investigated by the means of powder X-ray diffraction (XRD) [20]. Ionic conductivity mechanisms in LLTO are studied using $^7$Li-NMR techniques [21] and conductivity measurements. However, the exact voltage stability limit and decomposition kinetics of this material are unknown.

The aim of this thesis is to develop an appropriate analytical method for the mapping of stoichiometric inhomogeneities in $Li_{(0.29\pm\delta)}La_{0.57}TiO_3$ electrolytes, where field stress was applied, for a better understanding of decomposition mechanisms in LLTO. Qualitative, as well as quantitative LA-ICP-MS analysis of non-polarized and polarized LLTO substrates are performed. For quantitative measurements matrix-matched standards are necessary, which were consequently prepared.

# 2 Theoretical Aspects

## 2.1 Material to be examined – lithium lanthanum titanate (LLTO)

### 2.1.1 Perovskite structure

Lithium lanthanum titanates (LLTO) are known as perovskite-type materials. Perovskites have the general formular of $ABX_3$, whereby A is usually a large cation, B a medium-sized cation and X an anion (typically oxygen). Figure 2-1 shows the typical structure of the cubic perovskite $ABX_3$. The chemical and physical properties depend on the structure and the exact composition of the material. Thereby, essential properties can be controlled by the structure, which makes perovskites very interesting materials. [22] Perovskite-type alkaline-earth titanates ($ATiO_3$, A = Ca, Sr, Ba) have attracted widespread attention in the late 20th century because of their properties, for instance dielectricity and ferroelectricity [23]. Nowadays, also the electrochemical properties, such as electron and ion conductivity and surface catalytic properties of perovskite-type materials that contain transition metals on the B-site are of wide interest for catalytic applications or in solid oxide fuel cell electrodes [24].

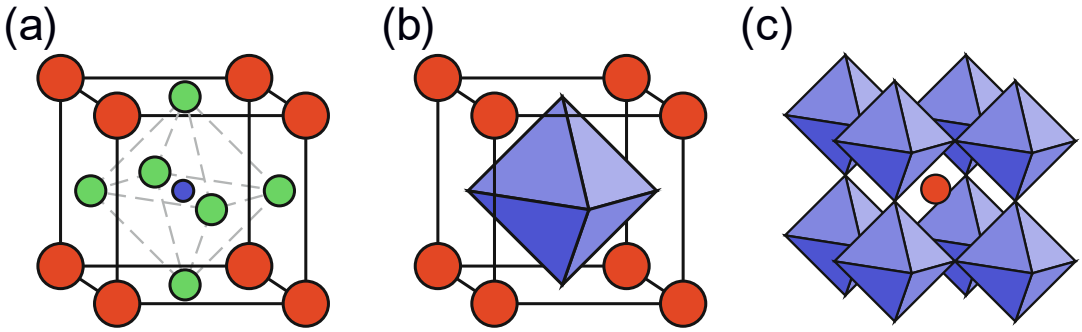


*Figure 2-1: Cubic perovskite structure $ABX_3$ – (a) atom positions with A-ions at the cell origin; (b) $BX_6$ octahedral coordination polyhedron; and (c) $BX_6$ octahedral polyhedron framework with A-ions at the cell origin.*

In the ideal perovskite structure, the ionic radii of A, B and X-ions must be in the right relation to one another. The relationship between the ionic radii and the degree of distortion can be described with the Goldschmidt tolerance factor *t*, which can be calculated using equation 2.1. *t* is called the tolerance factor, $r_A$ is the radius of the A cation, $r_B$ is the radius of the B cation and $r_X$ is the radius of the X anion. [22]

$$t = \frac{r_A + r_X}{\sqrt{2}\,(r_B + r_X)} \qquad (Equation\ 2.1)$$

The tolerance factor enables the prediction of the structure of the perovskite, the stability, and the distortion of the crystal structure. If the tolerance factor *t* lies in the range of 0.9 – 1.0 a cubic perovskite structure is quite likely. If $t > 1$, a hexagonal or tetragonal structure is preferred, which is the case when A-ions are too big or B-ions are too small. The tolerance factor decreases if the A-ions are smaller than the holes between the $BX_6$ octahedra. This leads to a cation displacement and tilting of corner-sharing $BX_6$ octahedra and therefore, to an orthorhombic structure. [25]

The perovskite-type lithium lanthanum titanates have a highly disordered A-site lattice, where La- and Li-ions as well as vacancies share the A-site. In order to fulfil the charge neutrality, the average cation charge on the A-site must be 2+. Consequently, LLTO perovskites have the general formular $Li_{3x}La_{(2/3)-x}\square_{(1/3)-2x}TiO_3$, where x may be in the range of: $0.04 < x < 0.16$. The relatively large amount of vacant A-sites in LLTO is the key property that enables quite fast Li-ion conduction. Different structures of LLTO have been reported, such as cubic unit cells, tetragonal unit cells, hexagonal unit cells and orthorhombic perovskite-type distorted cells. The real crystal structure depends on the amount of lattice vacancies and the synthesis method [23, 26, 27]. Especially the cubic and the tetragonal perovskite structure have received much attention due to their higher ionic conductivity, which makes them suitable for the application as a solid electrolyte in Li-ion batteries. The crystal structures of the cubic and the tetragonal perovskite structure are shown in Figure 2-2. Due to the lower activation energy of the A-sites compared to the 3c-sites, the $Li^+$-ions occupy the A-sites. In the cubic structure A-site ions ($La^{3+}$ and $Li^+$) and vacancies are randomly distributed in octahedral channels. In contrast, in the tetragonal structure the $La^{3+}$ ions are unevenly distributed, which leads to the tilting of $TiO_6$ octahedra. [26, 27]

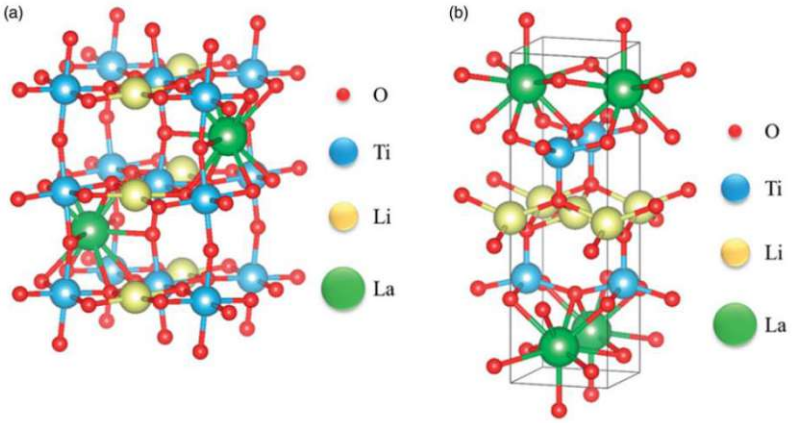


*Figure 2-2: Crystal structure of (a) cubic LLTO and (b) tetragonal LLTO [26]*

### 2.1.2 Conductivity properties of LLTO

The highest bulk lithium-ion conductivity of $1*10^{-3}$ S $cm^{-1}$ at room temperature was established at the $x \sim 0.11$ member of LLTO ($Li_{3x}La_{(2/3)-x}\square_{(1/3)-2x}TiO_3$). However, the overall ionic conductivity suffers from the low grain boundary conductivity. The mechanism of lithium-ion conduction is still disputable, depending on different structural parameters. For example, the A-sites ordering, the concentration of A-site vacancies and the lattice parameters strongly

influences the lithium-ion conductivity. More A-site vacancies lead to increased free space for the migration of lithium-ions and subsequently to higher ionic conductivity. The lithium content in LLTO determines the number of A-site vacancies, so the conductivity depends on the composition of LLTO. Higher lattice parameters result in a larger bottleneck size and therefore site percolations of lithium-ions get easier. [1, 23, 26]

In Figure 2-3 one mechanism of $Li^+$ migration is shown based on the planar representation of the crystal structure of LLTO. First of all, lithium-ions migrate from the A-site to vacancies, due to the lower activation energy compared to the 3c-sites. Subsequently, the lithium-ions percolate between adjoining vacant A-sites through a bottleneck. The bottleneck is situated between two adjacent A-sites, surrounded by four oxygen ions. By nuclear magnetic resonance (NMR) experiments, it was investigated that the lithium-ions move only in the ab-plane at temperatures < 200 K. Nevertheless, at temperatures > 200 K, lithium-ions can also migrate along the c-axis, indicating a 3D diffusion behaviour. [23, 26]

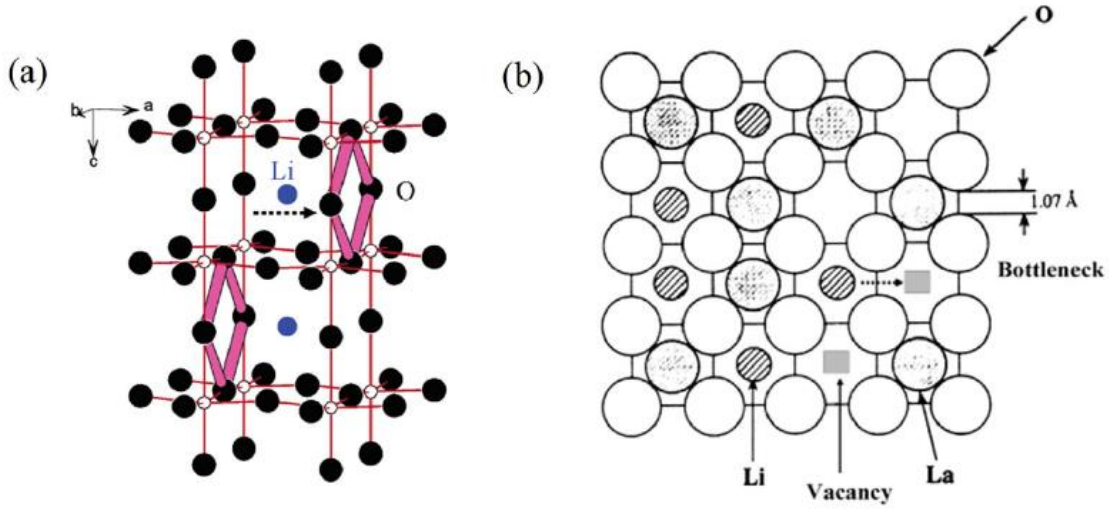


*Figure 2-3: Schematic representation of the migration of lithium-ions in crystalline LLTO. (a) shows the $Li^+$ migration along the ab-plane through bottlenecks, and (b) shows a planar representation of the crystal structure of LLTO. [23]*

The conductivity behaviour at room temperature is described as thermally activated in most literature. The dependence of ionic conductivity on temperature is defined as a non-Arrhenius behaviour. However, at temperatures > 127 °C, it is found that the relationship is a Vogel-Tamman-Fulcher (VTF) type relationship. Then the conductivity mechanism is known as a thermally assisted mechanism. [23, 26]

The electronic conductivity of LLTO depends strongly on the Li chemical potential. After synthesis, the Li chemical potential in LLTO is around 3 V vs. $Li^0$. Then, the electronic conductivity is in the range of $5*10^{-9}$ to $1*10^{-8}$ S $cm^{-1}$ at room temperature. So, the electronic conduction is negligible to the total ionic conduction in LLTO. However, at a potential lower than 1.8 V vs. Li metal, additional Li-ions partly fill the vacant sites, and Ti-ions (B-site ions) would be reduced from $Ti^{4+}$ to $Ti^{3+}$. The additional electrons lead to a strongly increased electronic conductivity. [26]

### 2.1.3 Current status of Li-ion batteries with liquid and solid electrolytes

Lithium lanthanum titanates (LLTO) can potentially be used as a solid electrolyte in all-solid-state lithium-ion batteries (LIBs). LIBs are one of the most dominant and promising energy storage devices due to their high energy densities, high power densities, low self-discharge, and long cycle life's.

Figure 2.4 shows a schematic representation of a lithium-ion battery with the set-up and the basic principles of a LIB. Between the two electrodes (1,2) is an ion-conducting electrolyte (3). A separator (4) between the anode and cathode prevents contact between the electrodes especially in case of mechanical stress. In commercially available LIBs lithium cobalt oxide ($LiCoO_2$, LCO) is used as positive electrode material. However, commercial alternatives for LCO are lithium manganese oxide ($LiMn_2O_4$, LMO), lithium nickel manganese cobalt oxide ($LiNi_{1/3}Mn_{1/3}Co_{1/3}O_2$, NMC) and lithium nickel cobalt aluminium oxide ($LiNi_{0.8}Co_{0.15}Al_{0.05}O_2$, NCA). Usually, the negative electrode is made of graphite ($LiC_6$). On the one hand, Li metal electrodes would enable a higher potential difference, but otherwise lithium metal is prone to dendrite growth. This leads to electrical contact between the anode and cathode and finally to a short circuit. [28, 29]

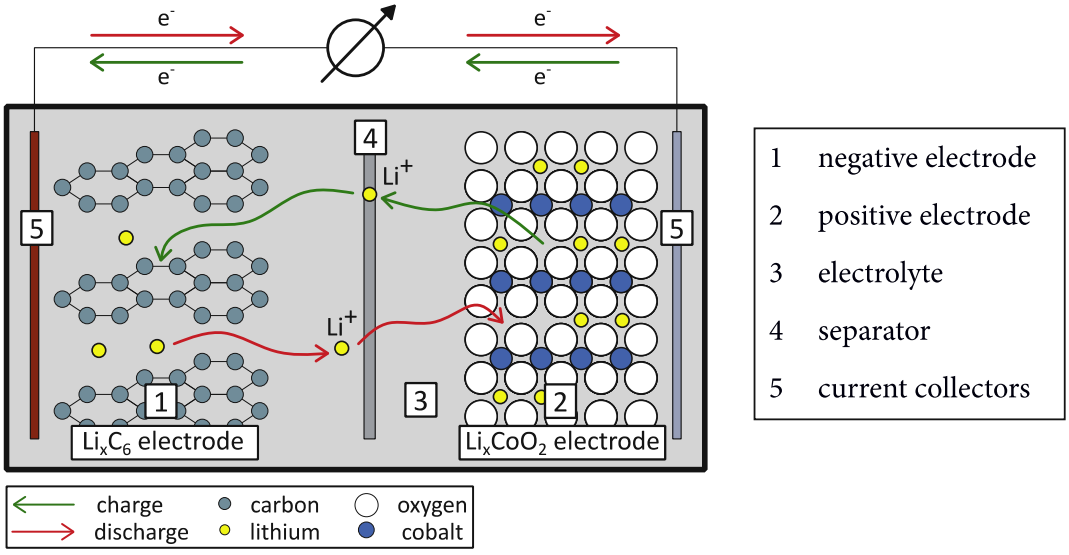


*Figure 2-4: Schematic representation of a lithium-ion battery (LIB)*

An electrolyte is an ionically conducting medium. Without this medium the lithium-ions cannot pass between the electrodes. Both, the volume between the cathode and the anode and the pores are filled and connected with the electrolyte. The electrolyte has today not only the task to transport ions from one side to the other, but must also fulfil a multitude of different requirements. [29, 30]

The main task of the electrolyte is to transport the lithium-ions back and forth between the electrodes. Furthermore, the electrolyte must be chemically and electrochemically stable - it should not react with the electrodes or other cell components. Stability related to the whole voltage range is also essential. Ionic conductivity should be provided at room temperature, but at the same time over a large temperature range. The electrolyte must ensure that the electrons are not transported through it, but rather via the current collectors. Hence, the electrolyte must

be an ion conductor with negligible electronic conductivity. Besides these requirements, the electrolyte should be safe, which means non-toxic and non-flammable, and additionally low cost. [29, 30]

Currently, almost exclusively non-aqueous electrolytes are employed in commercially available LIBs. Today's liquid non-aqueous electrolytes are made of three components: organic aprotic solvents, conducting salts and additives. Often a combination of the following substances is used as organic solvent: ethylene carbonate (EC), dimethyl carbonate (DMC), diethyl carbonate (DEC), ethyl methyl carbonate (EMC) or propylene carbonate (PC). Mixtures of EC and DMC are standard today. Pure EC should be avoided due to its high viscosity and melting point (36 °C). Apart from viscosity and melting point, permittivity ε is also an important property, which must be considered. A high permittivity ensures that lithium salts can be dissolved in large amounts. In a mixture with DMC, EC enables the dissolving of lithium salts because of its high permittivity and DMC decreases the viscosity and the melting point. At the moment, commercial LIBs are commonly equipped with lithium hexafluorophosphate ($LiPF_6$) as conducting salts. $LiPF_6$ is used due to its electrochemical stability allowing voltages up to 4.8 V vs. $Li/Li^+$, its high conductivity and its ability to prevent aluminium corrosion of the current collector. Challenges with these salts are that they are prone to hydrolysis, which leads to the formation of hydrogen fluoride (HF). $LiPF_6$ will degrade at higher temperatures (> 70 °C).

Besides these non-aqueous liquid electrolytes, polymeric electrolytes are in utilization in commercially available LIBs. Here, the lithium salts are dissolved in a polymer matrix instead of a liquid organic solvent. Polymer electrolytes are considered safer alternatives to liquid non-aqueous electrolytes due to their reduced volatility and its superior stability also at higher temperatures.

A major aspect of commonly available LIBs including liquid organic or polymeric electrolytes is the safety of these cells. Due to the importance of energy storage in LIBs and the exsisting drawbacks of the electrolytes mentioned above, research is being conducted into alternatives for currently available electrolytes. A safer alternative, which recently has received much attention, is the solid-state electrolyte-based LIB. LIBs based on liquid-free (solid) electrolytes are known as all-solid-state (ASS) LIBs. Next to the advantage concerning the safety aspect, ASS-LIBs possess several other advantages over commercialized LIBs.

In all-solid-state LIBs, the liquid organic electrolyte is replaced by an inorganic solid electrolyte. The absence of the flammable liquid increases the safety of ASS-LIBs compared to conventional LIBs. Furthermore, inorganic solid electrolytes have high thermal stability and electrochemical stability. Due to these properties this kind of electrolyte may be compatible with high-performance electrode materials. The possible utilization of these electrode materials, such as metallic anodes or high-potential cathode materials, could lead to increased energy densities. The reactivity of solids is much lower compared to liquids, hence longer lifetimes are expected for all-solid-state LIBs. [31, 32]

*Table 2.1: Comparison of the ionic conductivity in commonly reported electrolytes (at room temperature)*

| Species | Li-ion conductivity (S $cm^{-1}$) | Literature source |
|---|---|---|
| 1 M $LiPF_6$ in EC/DMC | $1.15*10^{-2}$ | [33] |
| PEO-$LiClO_4$ | $1*10^{-5}$ | [34] |
| LiPON (amorphous) | $2.3*10^{-6}$ | [35] |
| Perovskite-type LLTO | $1.53*10^{-3}$ (bulk) | [36] |
| Garnet-type LLZO | $1.3*10^{-3}$ | [37] |

Potential solid electrolytes in ASS-LIBs are crystalline inorganic Li-ion conductors. The used inorganic solids can be divided into four groups: (i) Li-ion conducting A-site deficient perovskite solid solutions (LLTO), (ii) LISICON and thio-LISICON-type Li-conductors, (iii) NASICON-type Li-ion conductors, and (iv) garnet-type Li-ion conductors (LLZO). However, besides crystalline materials, also composite inorganic Li-ion conductors and amorphous inorganic Li-ion conductors (LiPON) are investigated as possible solid electrolytes. [6, 23, 27]

However, there are also aspects in which the currently used electrolytes are superior to solid-state electrolytes. As can be seen from Table 2.1, the lithium-ion conductivity of a non-aqueous liquid electrolyte (1 M $LiPF_6$ in EC/DMC) is at least one order of magnitude higher than that of inorganic solid electrolytes, such as LLTO and LLZO. Metal anodes are problematic in liquid electrolyte-based LIBs due to the formation of Li dendrites which grow between the electrodes and form an electron-conducting connection, which causes a short-circuit. It was expected that this would be no problem in solid-state electrolytes. Nevertheless, Porz et al. (2017) have shown the ability of deposited lithium also to penetrate solid materials [38]. A further important challenge is that physical contact between the electrolyte and potential porous electrode materials must be present. Liquid electrolytes can infiltrate such porosities. However, solid electrolytes have hereof a disadvantage due to their lower flexibility and viscosity. [31] In summary, Li-ion batteries with solid electrolyte still face several challenges that need to be solved in order to exploit the advantages of higher safety and energy density with Li-metal electrodes. An important property of Li-ion electrolytes is the electrochemical stability window, which defines the electrode potential range in which the electrolyte is stable and has an ionic transference number close to 1. For LLTO, this window was so far investigated by first-principles calculations [39], but experimental investigations on the electrolyte breakdown are scarce. This work sheds some light on the degradation mechanism and stability window of LLTO electrolytes by field-stressed experiments with inert metal electrodes and subsequent laser ablation inductively coupled plasma mass spectrometry (LA-ICP-MS) analysis of Li-stoichiometry variations.

## 2.2 Analytical tool – laser ablation inductively coupled plasma mass spectrometry (LA-ICP-MS)

### 2.2.1 Laser ablation (LA)

The core part of a laser ablation (LA) device is, as its name implies, a laser and its optics which allows to modify the beam shape and energy. Besides that, the device consists of an ablation chamber, where the laser light is focussed onto the sample surface in order to ablate material. Furthermore, a connection between the ablation chamber and the following analytical device, which can be ICP-MS, but also other analytical techniques, is necessary. In the case of LA-ICP-MS, the task of the connection between the LA device and the ICP-MS instrument is to introduce the generated particle aerosol into the plasma of the ICP-MS.

Laser light has some unique characteristics compared to light from other light sources, making it very interesting for technological applications. These properties are monochromaticity, directionality, coherence, and high intensity. Furthermore, pulsed operation is possible with a laser. Due to the wave-particle dualism, light can be described as a wave, to be exact as an electromagnetic wave. Every wave in a laser beam has nearly the same direction, wavelength, and phase. So, the light generated by a laser is highly coherent. [40]

Laser is an acronym for light amplification by stimulated emission of radiation. Laser light is generated through the process of stimulated emission. A photon is only absorbed by an atom or molecule if the energy of the photon is equivalent to the energy gap between its ground state and its excited state. Then, there are two mechanisms, which lead to the decay of the excited state and the emissions of photons: spontaneous emission and stimulated emission. Both cases, as well as the process of absorption of a photon are shown in Figure 2-5 using a simplified energy diagram. At spontaneous emission, the photon spontaneously returns to the ground state and emits a photon. While in stimulated emission another photon, which has the same energy as the absorbed photon, interacts with the excited photon. The interaction leads to an emission of two photons, the stimulated photon, which is the former excited photon, and the second photon, which is not absorbed by the atom or molecule. The, in the case of a laser, interesting difference between spontaneous and stimulated emission is that there is an amplification of the emission due to the higher number of photons after stimulated emission. Additionally, in the case of stimulated emission, the emitted photons, which as mentioned before can be described as waves, have the same energy, and therefore the same wavelength compared to the stimulating light. The photons generated by stimulated emissions are emitted in the same direction as the stimulating photons. Hence, stimulated emissions produce light with the above-mentioned properties, which is used in lasers. For completeness, it should be mentioned that those spontaneous emissions of photons occur in random directions. [40, 41]

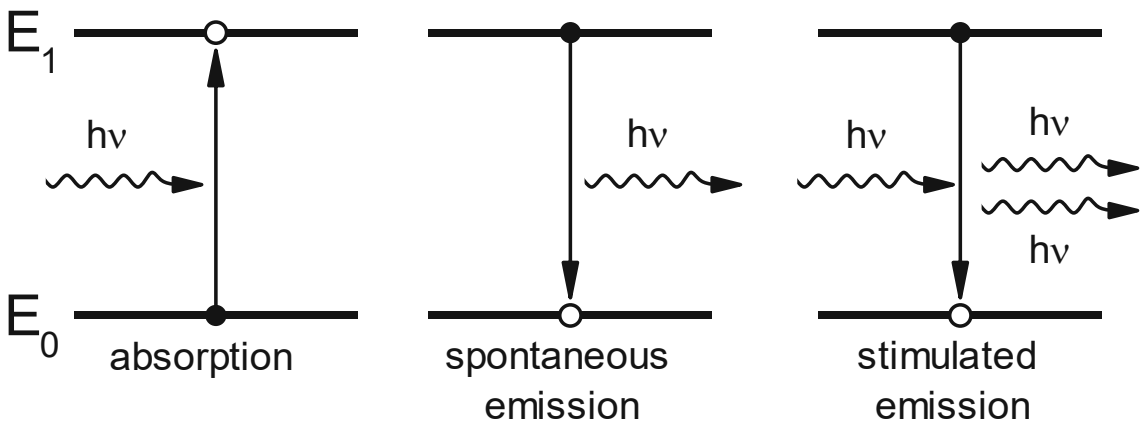


*Figure 2-5: Processes, which take place during excitation and the decay of excited states*

Only excited photons can be emitted through stimulated emissions. However, as Boltzmann's law predicts, most photons in thermal equilibrium are in the ground state while only a few photons are in higher energetic excited states. To achieve light amplification a population inversion must be obtained. This means that the majority of the photons has to be in an excited state. A population inversion is gained by creating a non-equilibrium situation. Therefore, energy must be introduced into the system from an external source. This can be done by electrical pumping or optical pumping. In electrical pumping, the laser medium is placed in an electron beam, or an electric discharge is created. Different from the schematic representation in Figure 2-5, there are commonly three or four energy levels which participate in the process of creating a population inversion. [40, 41]

Another important part which is necessary for the amplification of light is the resonator. The task of the resonator is to reflect the photons, so that they pass several times through the laser medium. In doing so increasing stimulated emissions occur and hence light is amplified. Typically, two mirrors are used. One is 100 % reflective whereas the other only transmits a small fraction of the light. [40, 41]

In a laser ablation device, different kinds of lasers can be used. Usually, solid-state lasers or excimer lasers are implemented. The most common representative of solid-state lasers is the neodymium-doped yttrium aluminium garnet laser (Nd:YAG laser). The laser medium in such a solid-state laser is composed of a passive host material (YAG) and an active ion (Nd). In the active ion, neodymium, stimulated emission happens and hence laser light is generated. In Nd:YAG lasers, pumping is carried out by optical pumping via a lamp or diode, and the laser can be operated pulsed or continuously. For the pulsed operating mode Q-switching is necessary. In a Q-switched laser the quality of the resonator will be reduced, with the result that the population inversion reaches its maximum. The stored energy will be released, after achieving a maximal population inversion, within a short time by changing the quality of the resonator and the whole energy is emitted in the form of one single pulse. The wavelength of laser light from a Nd:YAG laser is 1 064 nm (IR region). However, with nonlinear optics the wavelength can be changed. Therefore, second harmonic generation crystals, such as potassium titanyl phosphate (KTP), lithium triborate (LBO) or beta barium borate (BBO), are applied. If photons at IR wavelength get into the crystal, nonlinear processes lead to a doubling of the frequency of these photons. In this process not all photons get converted. As a

consequence, the energy per photon is higher due to the shorter wavelength, nevertheless the intensity of the radiation is less. In LA devices often Nd:YAG lasers with a wavelength of 266 nm or 213 nm in the UV range are utilized. [40, 42, 43]

Apart from Nd:YAG lasers, also excimer lasers are applied to LA devices. These lasers are of big interest due to their high-energy, ultraviolet (UV) output. Compared to Nd:YAG lasers, no transformation of produced light to ultraviolet light, which leads to losses in intensity during the nonlinear processes, is needed. The setup of an excimer laser is different to the lasers mentioned above. They run under high pressure, so the pumping has to happen through a transverse discharge or with high-energy electron beams. The energy, which must be added during pumping, must be very high. Hence the laser light is only stable if the laser is operated in a pulsed manner. Apart from the setup the laser medium and the achievement of population inversion are completely different. As laser medium gaseous excimer molecules are used. These are molecules, which are only stable when they are in an excited state. If the excitation decays, the bonds between the atoms break apart and the molecules dissociate. So, the requirement of population inversion is fulfilled simply through the dissociation of excimer molecules in the ground state. In LA devices applied excimer molecules usually are krypton fluoride (KrF*, $\lambda$ = 248 nm) or argon fluoride (ArF*, $\lambda$ = 193 nm). The laser medium consists of the two gases of the excimer molecules and of a buffer gas (He, Ne), which enhances heat dissipation due to its high thermal conductivity. The pumping of the laser medium to obtain population inversion is the challenging part of excimer lasers. High electrical energy must be deposited in a short time. Therefore, often a two-stage power supply is employed. In the first step the energy storage system is charged. Then, the stored energy is switched to the laser head. [40, 42]

### 2.2.2 Inductively coupled plasma – mass spectrometry (ICP-MS)

Inductively coupled plasma (ICP) mass spectrometry (MS) is a commonly used technique for trace element analysis in many different research and application fields, such as environmental, earth and life sciences, and material, chemical and semiconductor industries. The application of ICP-MS is wide-ranging, due to its low detection limits (ng/g – pg/g), its high dynamic range (up to 9 orders of magnitude), and its isotopic capability, as well as its multielement characteristics. [44, 45]

Generally speaking, in ICP-MS usually an aerosol is introduced into a plasma. In the plasma, different processes occur, during which the introduced aerosol gets dried, atomized, and ionized. The ions are separated by a mass filter and then detected. Today, several different designs of ICP-MS instruments are available. Despite this variety, they share many similar components, and the typical setup of an ICP-MS instrument is shown in Figure 2-6. The setup of an ICP-MS device typically consists of a sample introduction system, a plasma torch, an interface, ion optics, a mass analyzer, and a detector. [44, 45]

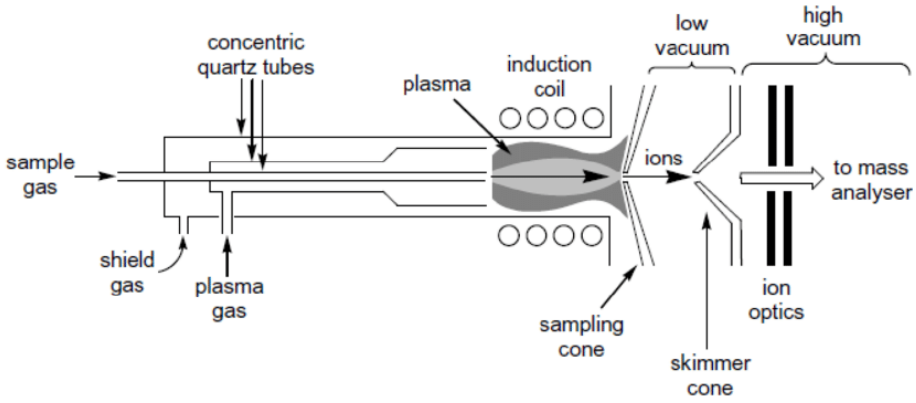


*Figure 2-6: Representation of a plasma torch and an interface of an ICP-MS instrument [46]*

The introduction system of an ICP-MS instrument is the first essential part of the device. The main task of the introduction system is the aerosol generation and the droplet selection. It consists of a nebulizer and a spray chamber if a liquid sample is introduced in the system. The sample solution is pumped, for example with a peristaltic pump, into the nebulizer, where it is converted with a nebulizing gas (typically argon) into a small droplet aerosol. The subsequent spray chamber eliminates all large droplets except those that are small enough for introduction into the plasma ion source. For this purpose, there exists different kinds of nebulizer and spray chamber designs. Frequently integrated designs are concentric, cross-flow, and micro-flow nebulizers and double-pass or cyclonic spray chambers. Moreover, gaseous and solid samples can also be introduced into the ICP-MS. For a solid introduction small sample particles are generated via laser ablation (LA) and these nanoparticles are brought into the plasma through a carrier gas. [44]

The next step is the atomization and ionization of analytes in the ICP torch. The plasma ion source generates the plasma and transfers the analytes into charged ions. The main parts of the plasma ion source are the plasma torch, the radiofrequency (RF) coil and the power supply. The ICP torch is composed of three concentric tubes: an outer tube, a middle tube, and a sample injector tube. The setup of such an ICP torch is illustrated in Figure 2-7. Between the outer and the middle tube, the gas, which forms the plasma, passes through. A second gas flow (auxiliary gas) passes between the middle tube and the sample injector, and a third gas flow (nebulizer gas) transports the sample droplets from the sample introduction system to the centre of the plasma. The plasma torch is fixed horizontally and is positioned centrally in the RF coil. In the plasma torch the liquid droplets are dried and vaporized to a gas. These gaseous particles are then atomized and ionized due to the high energy (T ~ 6 000 °C) of the plasma. Because of the high energy all bonds are broken, and for most elements most of the atoms are ionized. Compared to low-energy ion sources, there is a loss of information about molecular mass and molecular structure. [47, 48]

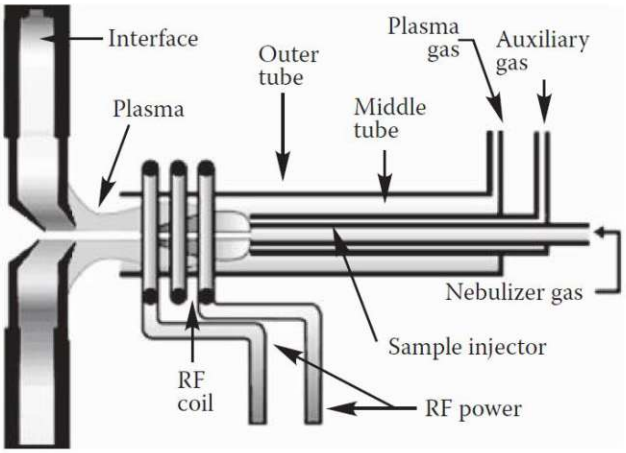


*Figure 2-7: Detailed view of a plasma torch and a RF coil [48]*

The in the plasma generated ions are guided through the interface and afterwards to the lens system. The plasma operates at atmospheric pressure, however, for the mass filter, a high vacuum is required. The purpose of the interface is to enable pressure reduction between the plasma and the mass separation device. The transition from atmospheric pressure to high vacuum is achieved through two inverted funnel-like devices, which are known as cones. These cones can be seen in Figure 2-6 as well as in Figure 2-7. They have an aperture of approximately 1 mm in diameter, so that ions can pass through these cones. Both cones are water-cooled due to the high temperature of the plasma. Between the cones, a fine vacuum (1-2 mbar) prevails, which is created by a rotary vane pump. The regions after the cones are evacuated to an (ultra) high vacuum ($10^{-7}$ mbar) by a turbomolecular pump. If the gas pressure in this and the following areas is too high, the mean free path is too short, and the ions will collide and hence release their charge. The generated ions are able to arrive at the mass spectrometer without interruption due to the interface. Before entering the mass analyzer, the ion optics consisting of multiple electrostatic lenses prevents them from diverging. Therefore, electrostatic lenses with different specific voltages are utilized. Additionally, the ion beam is often deflected before the ions are separated in order to separate neutrals and photons from the ion beam. [48]

The mass separation device is responsible for ensuring that the charged ions are separated according to their mass-to-charge ratio (m/z ratio). In ICP-MS this separation can be achieved using multiple mass spectrometer instruments. Commonly applied kinds of devices are the quadrupole mass filter, time-of-flight mass spectrometers (TOF-MS), and magnetic sector systems. The quadrupole mass filter, which is also used in the experimental set-up of the performed measurements, consists of four rods, which allow only the preselected mass-to-charge ratio to pass through. Direct current (DC) and alternating current (AC) of radiofrequency (RF) are applied on opposite pairs of the rods. When using the proper combination of direct and alternating current, only ions with the selected m/z ratio pass through the rods. After the separation process, the detector, in most cases a secondary electron multiplier (SEM), counts the arriving ions. The ions, which enter the detector, strike the first dynode's active surface, and secondary electrons are released. Then the electrons are accelerated to the next dynode releasing a greater number of electrons. The amplification of electrons is repeated until a measurable pulse is created. By detecting these pulses, the system counts the ions which arrive at the first dynode. [47, 48]

### 2.2.3 Solid sampling and analysis by LA-ICP-MS

Laser ablation inductively coupled plasma mass spectrometry (LA-ICP-MS) is a widely used analysis technique for direct solid sampling. Due to the sensitivity of ICP-MS the measurement of major, minor and trace elements in solid samples is possible. LA-ICP-MS is a connection of the above-described techniques: the sampling is carried out via laser ablation (LA), and the analysis of the sample atoms is achieved via inductively coupled plasma mass spectrometry (ICP-MS).

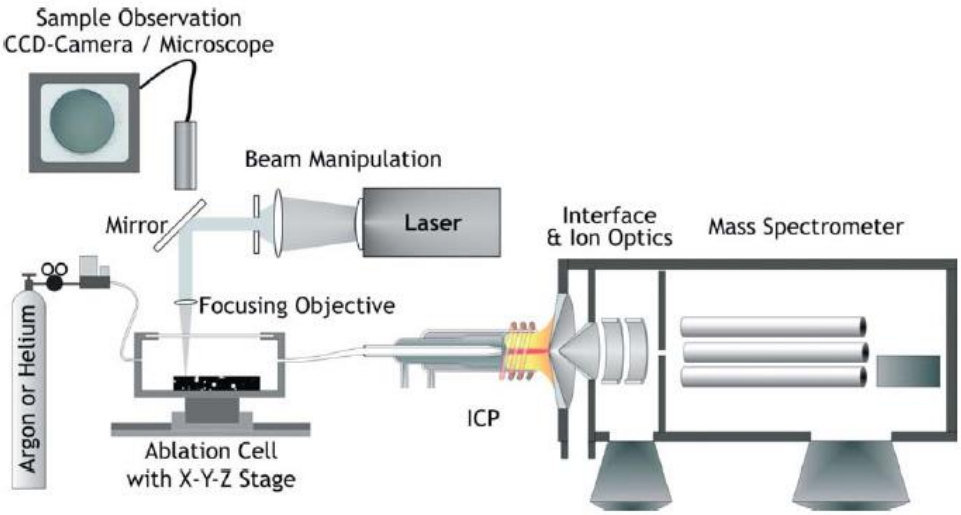


*Figure 2-8: Schematic illustration of the setup of a laser ablation inductively coupled plasma mass spectrometry (LA-ICP-MS) system [49]*

Figure 2-8 shows a potential setup of a LA-ICP-MS system consisting of a LA device, including the laser and an ICP-MS instrument. The detailed structure of a laser is explained in *2.2.1 Laser ablation (LA)*, and the components of an ICP-MS instrument, as well as the processes in these components, are described in *2.2.2 Inductively coupled plasma – mass spectrometry (ICP-MS)*. Hence, these devices are not explained in greater detail at this point. However, the ablation process, advantages of LA-ICP-MS, as well as challenges of this technique are mentioned here.

In LA-ICP-MS, the sample is placed in a so-called ablation chamber/ablation cell, which is purged with a carrier gas (He or Ar). Different designs of ablation chambers are used in LA, for example, there are special designs for imaging applications, which leads to a faster wash-out behaviour. For solid sampling a pulsed laser beam is focused on the sample surface. Because of the high energy of the laser pulse, the material gets ablated, and the removed material is transported to the plasma of the ICP-MS. Ablation means that a fraction of the solid sample is converted into particles and gaseous constituents. The ablation process depends on a multitude of instrumental parameters, such as the wavelength of the laser radiation, the duration of the laser pulse, the applied atmosphere (He or Ar) but also sample related parameters such as the composition of the sample matrix, and many other factors. As previously mentioned, after ablation, the sample aerosol is transported with a carrier gas flow into the plasma of the ICP-MS. In the plasma the material is atomized and ionized, and subsequently, the ions are analysed by a mass separation device. [49, 50]

In laser ablation devices Nd:YAG solid-state lasers and excimer lasers are commonly used. Excimer lasers have a high-power UV output with a good electrical efficiency compared to Nd:YAG lasers, which need non-linear processes to gain laser radiation with wavelengths in the UV range. A shorter wavelength in LA-ICP-MS means that there is a higher energy density for the breaking of bonds during the ablation process. The thermal alteration of the material is reduced if using shorter wavelengths. Not only the ablation process itself depends on the wavelength, but also plasma shielding. Plasma shielding occurs when the initial photons of the laser pulse generate a plasma, and the following photons cause an expansion of the plasma plume. The expanded plasma absorbs photons, acting as a protective shield for the sample surface. The absorption of photons in plasma depends on the wavelength and longer wavelengths have a greater absorption. So, radiation with shorter wavelengths leads to a more efficient ablation. A further advantage is that excimer lasers have a flat-top laser-beam energy profile compared to most Nd:YAG lasers, which have a Gaussian laser-beam energy profile. If the laser-beam energy profile is Gaussian-shaped, the ablation crater gets cone-like after more laser pulses. Depth resolution and fractionation will be influenced by the shape of the ablation crater. Besides the wavelength of the laser beam, the duration of the laser pulse also has a major influence on the ablation behaviour. Femtosecond laser pulses improve the ablation efficiency compared to nanosecond lasers. Furthermore, plasma shielding and thermal effects are reduced when using femtosecond lasers. [49, 50]

An interesting advantage in the application of LA-ICP-MS is that solid samples can be examined directly. Solid sampling brings several advantages compared to liquid sampling. However, there are also challenges in LA-ICP-MS. Starting with the strengths of this technique, for the direct analysis of the solid material no sample preparation is required. In liquid sampling a part of the solid sample must be dissolved in acids, organic solvents, or other liquids. These digestions of solid samples for the subsequent liquid analysis can be very time consuming. Moreover, several novel high-performance materials, such as ceramics, are often not easily dissolvable and require significant amounts of high purity reagents. Additionally, the manual handling during digestion can lead to contaminations and to loss of volatile compounds. Due to the direct measurements of the solid sample via LA-ICP-MS, the above-described drawbacks can be avoided. Besides the benefits concerning sample preparation, LA-ICP-MS is able to obtain spatially resolved information of the sample, including laterally elemental distribution and the distribution within the depth. In contrast, in liquid sampling this information gets lost during the dissolution process. Because of this, in liquid analysis only the bulk concentrations are investigated, while by using LA-ICP-MS also surface and interface analysis can be performed. Depth profiles and elemental distribution images are commonly conducted experiments to investigate solid samples.

Except for LA-ICP-MS, other solid surface analysis techniques, such as X-ray photoelectron spectroscopy (XPS), secondary ion mass spectrometry (SIMS), and energy-dispersive X-ray spectroscopy (EDXS), are available. In LA-ICP-MS no high vacuum is required compared to XPS, SIMS, and EDXS. Furthermore, the sensitivity of LA-ICP-MS is for most elements much higher than the sensitivity in the above-mentioned techniques. Compared to XPS, SIMS, and EDX, bulk analysis is possible in addition to spatially resolved analysis by increasing the beam size and the laser fluence. By ablating into depth, the sample composition at the surface can be compared with that in the bulk. [51]

However, LA-ICP-MS not only offers advantages, but also poses challenges that limit the applications of this technique. It is a big issue that the measured signal intensities are not exactly representative to the sample composition due to the matrix effects (as in the most solid sampling techniques), elemental fractionation, differences in transport efficiency and so on. Elemental fractionation can proceed during the ablation process itself, the transport to the plasma, as well as during vaporization, atomization and ionization within the plasma. A variety of reasons lead to these effects, depending on the process in which it occurs. During the ablation process, thermal properties and particle size distribution are important parameters. So, if the measured composition deviates from the real composition of the sample due to such non-stoichiometric effects, this affects the accuracy of this method [49, 50]. Additionally, it makes the signal of a particular element strongly dependent on the matrix of the sample. This leads to difficulties in quantitative analysis. Quantification by external calibration using certified reference materials (CRMs) is a reliable approach, which circumvents the matrix dependence by having the same matrix in standards as well as in sample. However, CRMs are usually not available for novel materials. Therefore, a multitude of alternative quantification strategies has been developed. Commonly used approaches are the use of in-house prepared matrix-matched standards, external calibration in combination with signal normalization to an internal reference element, and “solid-liquid” calibration with a dual flow system. In summary, several quantification strategies have already been developed, but quantitative analysis can still be very challenging and time-consuming in many cases. [52]

# 3 Experimental

## 3.1 Samples und Reagents

For the investigations LLTO ($Li_{0.29}La_{0.57}TiO_3$) substrates (Toho Titanium Company, Japan), with a nominal composition of 1.14 wt.% Li, 44.72 wt.% La, 27.04 wt.% Ti and 27.11 wt.% O, in different sizes were used. The utilised reagents for the standard preparations are listed in Table 3.1. Tuning of the LA-ICP-MS instrument was performed using NIST 612 trace metals in glass standard (National Institute of Standards and Technologies, USA), and the LA-ICP-MS instrument was operated with helium (≥ 99.999 %; Messer) and argon (≥ 99.999 %, Messer).

*Table 3.1: Used reagents for standard preparation*

| Reagent | Formula | Purity | Manufacturer |
|---|---|---|---|
| Lanthanum(III) oxide | $La_2O_3$ | 99.999 % | Sigma-Aldrich |
| Lithium lanthanum titanate (LLTO) | $Li_{0.29}La_{0.57}TiO_3$ | - | Toho Titanium |
| Lithium carbonate | $Li_2CO_3$ | 99.997 % | Sigma-Aldrich |
| Lithium oxide | $Li_2O$ | - | - |
| Titanium(IV) oxide | $TiO_2$ | 99.995 % | Alfa Aesar |

## 3.2 Instrumentation

### 3.2.1 Laser ablation (LA) device

An excimer-based laser ablation system (imageGEO193, Elemental Scientific Lasers, United States) was used for solid sampling. The excimer laser utilizes argon, fluorine, and helium (buffer gas) as laser medium and operates at a wavelength of 193 nm in the UV range. Laser pulses in the duration of nanoseconds were produced by this LA instrument. The laser was controlled via the software “Active View 2”, which had been delivered together with the instrument. As ablation chamber an analytical cup (TwoVol3, Elemental Scientific, United States) was used.

### 3.2.2 Inductively coupled plasma – mass spectrometry (ICP-MS) device

An ICP-MS device (iCAP Q, ThermoFisher Scientific, Germany) equipped with a quadrupole mass analyser was used for the LA-ICP-MS measurements. The data evaluation was conducted by the software "Qtegra", which had been delivered together with the instrument.

### 3.2.3 Coupling of LA and ICP-MS

The connection between the LA device and the ICP-MS instrument was achieved by using a polymeric tube (Tygon®, inner diameter: 1.6 mm) and a dual concentric injector (DCI, Elemental Scientific, United States). The DCI consist of two tubes: an inner capillary in which the sample aerosol and the helium (from laser) flow and an outer tube with an argon flow (make-up gas). This construction reduces signal broadening during transport leading to advantages regarding wash-out time, spatial resolution in imaging and sensitivity.

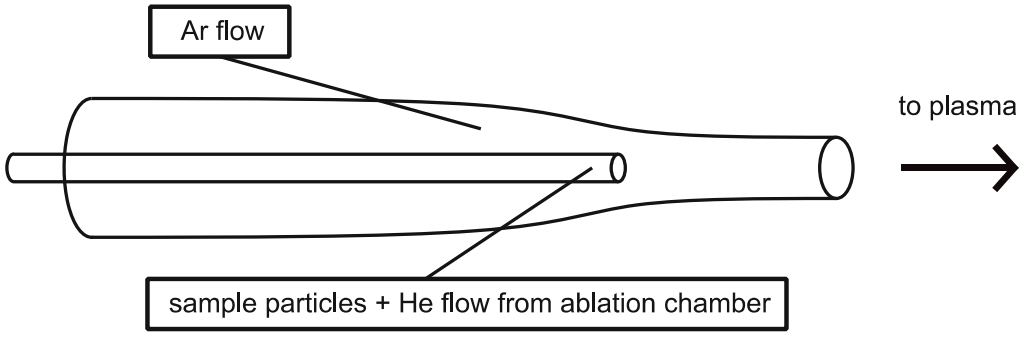


*Figure 3-1: First-generation Dual Concentric Injector (DCI)*

The measurements were performed with two different designs of the DCI, the first-generation DCI can be seen in Figure 3-1 and the second-generation DCI can be seen in Figure 3-2. The first-generation DCI had to be put into an injector and the plasma torch. The following model consists of a single piece that is previously assembled.

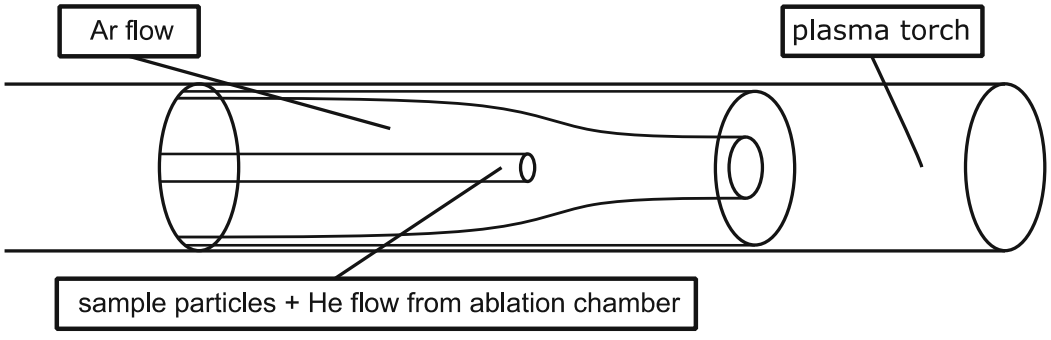


*Figure 3-2: Second-generation Dual Concentric Injector (DCI)*

## 3.3 Optimization experiments using LA-ICP-MS

Prior to sample analysis, tuning of the ICP-MS parameters has been performed for maximal signal intensity of $^{7}Li$, $^{115}In$ and $^{238}U$ using NIST 612 trace metals in glass standard (National Institute of Standards and Technologies, USA) .Before starting the measurements of LLTO substrates via LA-ICP-MS, some preliminary experiments had to be performed to optimize the measurement parameters. Finding the optimal measurement parameters is essential to receive reliable, reproducible, and accurate measurement results. The following measurement parameters were optimized through different experiments: laser fluence, beam size, helium flow, and overlap. Besides the measurement parameters, the isotopes, which were measured when analysing LLTO, had to be selected based on their abundance and interferences with other elements.

### 3.3.1 Laser fluence

To figure out which laser fluence is appropriate for the determination of lithium (Li), lanthanum (La), and titanium (Ti) in LLTO via LA-ICP-MS, line scans with different laser fluences were carried out. The experiments started with a laser fluence of 0.50 J $cm^{-2}$ and ended at 2.50 J $cm^{-2}$ laser fluence, in this range measurements were performed at intervals of 0.25 J $cm^{-2}$. Before the signal collection, pre-ablation (5 lines, 1.5 J $cm^{-2}$) was performed due to the removal of inhomogeneities in surface-near layers. The ablated lines had a length of about 3 000 µm, which results in a signal duration of approximately 5 s with the corresponding measurement parameters (see Appendix Table 0.1).

### 3.3.2 Helium flow

The helium flow influences the wash-out behaviour of the measured isotopes. Therefore, the helium flow had to be optimized for a minimal wash-out time. At this measurement, line scans (3 000 µm line length) with different helium flows were performed, and the wash-out times were compared. The corresponding measurement parameters are shown in Table 0.2 in the appendix.

### 3.3.3 Overlap

During the qualitative LA-ICP-MS measurements of LLTO substrates, the need for a diminution of the overlap due to the high ablation rates was discovered. With a smaller overlap, material is removed less often per sample location. Thus, a lower ablation depth per line is achieved in total. In these experiments, the repetition rate, the spot size, and the scan speed were varied, as these parameters affect the ablation rate. Table 0.3 in the appendix shows the corresponding operating parameters.

## 3.4 Preparation of field-stressed LLTO substrates

The aim of the sample preparation is to produce samples on which voltage can be applied in order to investigate the stability window of LLTO. Therefore, Li-ion blocking electrodes of platinum (Pt) and in later experiments of gold (Au), were sputtered onto the surface of LLTO sheets. Afterwards, a voltage was applied to these electrodes.

### 3.4.1 Sputter deposition (SD)

The circular electrodes out of Pt and Au were produced by a DC magnetron sputter coater (MED 020, Bal-tec) and a shadow mask with holes between 700 and 1 000 µm diameter. Sputtering was performed for 380 seconds in the case of Pt, and for 200 seconds in the case of Au. The resulting electrodes had a thickness of about 200 nm and a diameter of 1 mm. An overview of a LLTO substrate after sputtering electrodes and a detail of an electrode can be seen in Figure 3-3.

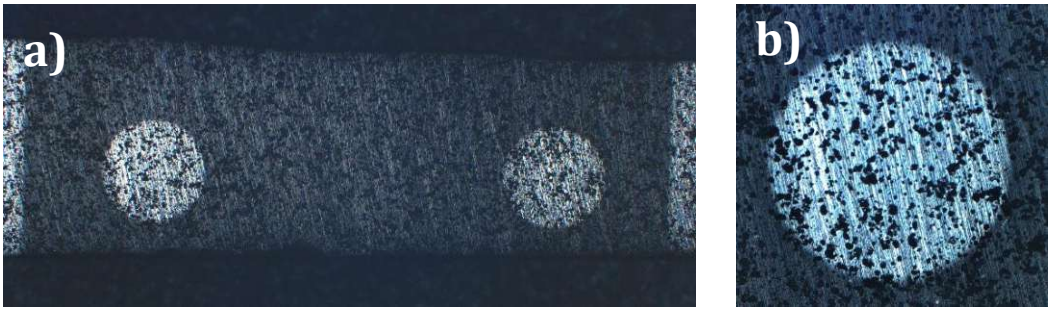


*Figure 3-3: Pt-electrodes produced by sputter deposition: (a) overview of sputtered electrodes on a LLTO substrate, and (b) detail of an electrode*

### 3.4.2 Polarization

Voltage was partly applied inside an evacuated vacuum chamber ($10^{-5}$ mbar) and in the case of one experiment in atmospheric pressure. The polarizations were performed under different voltages, temperatures, and durations for various experiments. An overview of the polarization conditions can be found in Table 3.2. A schematic representation of the setup of the polarization experiment and the processes occurring during polarization can be seen in Figure 3-4.

*Table 3.2: Overview of the conditions during polarization*

| Experiment (#) | Voltage (V) | Temperature (°C) | Duration (min) | Pressure (mbar) |
|---|---|---|---|---|
| E1 | 5-10 | 100 | 90 | $10^{-5}$ |
| E2 | 10 | 100 | 90 | $10^{-5}$ |
| E3 | 10 | 120 | 90 | $10^{+3}$ |
| E4 | 2.5 | 160 | 1080 | $10^{-5}$ |
| E5 | 4 | 150 | 120 | $10^{-5}$ |
| E6 | 6 | 150 | 120 | $10^{-5}$ |
| E7 | 8 | 150 | 120 | $10^{-5}$ |

When the applied voltage is beyond the electrochemical stability window of LLTO, $Li^+$ ions migrate from the anode to the cathode. Lithium depletion should occur at the anode, and the excess $Li^+$ ions should accumulate at the cathode. During the polarization experiments at higher voltages, electro-colouration ("blackening") in the cathodic region was observed (see Figure 3-5). The excess charge of the $Li^+$ ions that partially fill the A-site vacancies is balanced by reducing $Ti^{4+}$ ions to $Ti^{3+}$ ions. The additional electrons lead to higher light absorption and thus greyish colouration. A further problem for the application as a solid-state electrolyte in LIBs is that these electrons of $Ti^{3+}$ ions provide electrical conductivity.

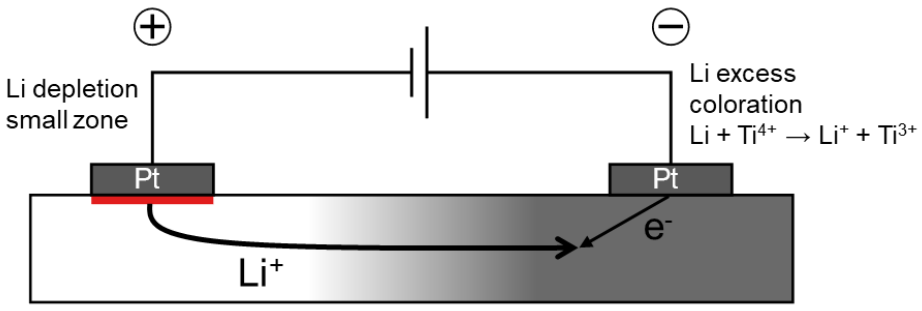


*Figure 3-4: Schematic setup of the polarization experiments*

The electrical current between the electrodes is most likely partially electronic and partially ionic. An upper boundary for the number of transported Li-ions can be calculated when we assume that the electrolyte between the excess and depletion zones remains fully blocking for electronic carriers, according to Faraday's law:

$$\Delta n(Li^+) \leq \frac{\int Idt}{F}, \qquad (Equation\ 3.1)$$

where F is Faraday's constant.

When we furthermore consider that the maximum change in Li concentration in the depletion zone is 0.29 p.f.u. (initial Li amount), we can give an estimation for an upper boundary of the Li depletion zone volume $V_{dep}$.

$$V_{dep} \approx \Delta n(Li^+) * \frac{V_m}{0.29} \qquad (Equation\ 3.2)$$

Where $V_m$ is the molar volume of LLTO (35 $cm^3\ mol^{-1}$), and accordingly the depth of the Li depletion zone $d_{dep}$

$$d_{dep} \approx \frac{\int Idt \cdot V_m}{0.29\ F A_{anode}} \qquad (Equation\ 3.3)$$

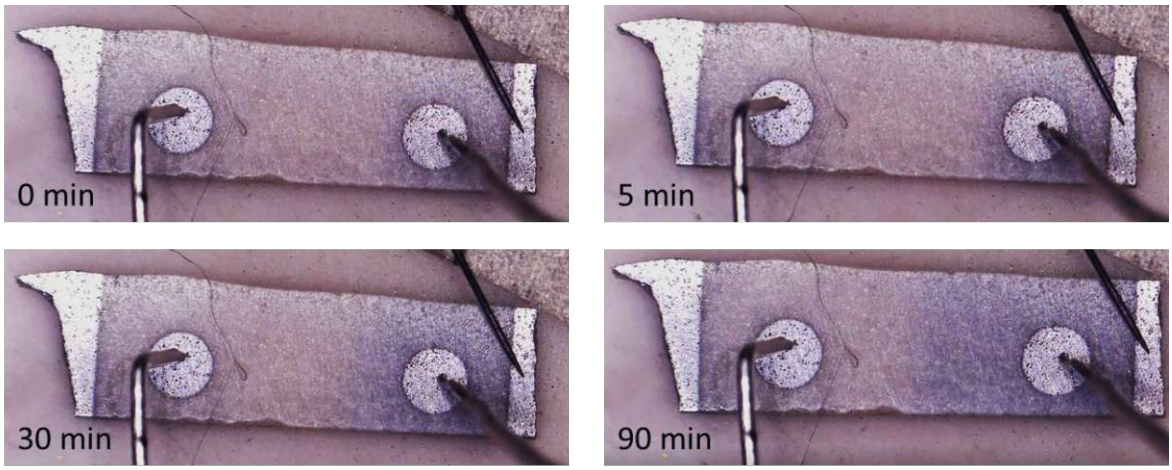


*Figure 3-5: Blackening of the cathodic region*

## 3.5 Qualitative LA-ICP-MS measurements of LLTO substrates

### 3.5.1 Non-polarized LLTO substrate

A qualitative measurement of a non-polarized LLTO substrate was performed via LA-ICP-MS. Therefore, line scans without spaces between the lines were carried out to create an image. The size of the image was 3 082 µm x 1 060 µm. The corresponding operating parameters of LA and ICP-MS are shown in Table 3.3. After ablating the first layer, four further layers were removed by LA and the signal was recorded. The ablation rate to the corresponding operating parameters was approximately 500 nm/layer, which was measured with a profilometer (DektakXT®, Bruker, United States). Hence, in total, a layer of 2.5 µm was removed and examined.

*Table 3.3: Operating parameters of LA and ICP-MS during qualitative imaging of LLTO substrates*

| Laser ablation | | Inductively coupled plasma mass spectrometry | |
|---|---|---|---|
| Laser fluence | 1.50 J $cm^{-2}$ | RF power | 1 550 W |
| Beam size | 20 µm | Auxiliary gas flow | 0.80 mL $min^{-1}$ |
| Repetition rate | 200 Hz | Cool gas flow | 13.85 mL $min^{-1}$ |
| Overlap | 17 µm | Nebulizer gas flow | 0.95 L $min^{-1}$ |
| Scan speed | 600 µm $s^{-1}$ | Dwell time per mass | 10 ms |
| He flow | 800 mL $min^{-1}$ | Measured Isotopes | $^{6}Li$, $^{46}Ti$, $^{138}La$ |

### 3.5.2 Polarized LLTO substrate

Besides the qualitative measurement of a non-polarized LLTO substrate, also a qualitative investigation of a field-stressed LLTO substrate was performed. The polarization conditions correspond to the conditions of experiment "E1" in Table 3.2. The operating parameters of LA and ICP-MS are the same as in the investigation of non-polarized LLTO substrates and are shown in Table 3.3. Here also line scans without spaces between the lines were performed to create an elemental distribution image. The image size was 5 355 µm x 620 µm, and in total, three layers were ablated.

## 3.6 Removal of Li accumulation in surface-near layers

During the qualitative measurements, increased Li signals in surface-near areas of native LLTO substrates were detected. Details of the lithium accumulation are described in 4.3 *Removal of the Li accumulation in surface-near layers*. Therefore, strategies for the removal of the Li accumulation in the first layer were developed, to achieve a stable signal and to be able to detect the lithium depletion beneath the anode already in the first ablated layer. Two different approaches to remove the Li accumulation in surface-near layers were developed: (i) pre-ablation with low laser fluence before the actual ablation and (ii) leaching of LLTO substrates in water in an ultrasonic bath. Both approaches and the combination of them have been applied to LLTO samples.

### 3.6.1 Pre-ablation

In order to find out whether the approach of pre-ablation is expedient or not, only point measurements were initially carried out. First, a pre-ablation was performed on one measurement point on the LLTO substrate surface by directing three laser pulses with low laser fluence at the same position. Next, the proper ablation at this spot with the normally used higher laser fluence (1.50 J $cm^{-2}$) was performed, and the signal was recorded. This procedure was repeated four times at different positions to obtain better statistics. Pre-ablation experiments with the lowest possible laser fluence 0.09 J $cm^{-2}$, 0.15 J $cm^{-2}$, and 0.30 J $cm^{-2}$ were conducted. For the evaluation, the area of the signal was integrated and used at this point.

To evaluate this approach pre-ablation with low laser fluence was applied during an imaging experiment. The first three layers of a LLTO substrate were ablated with a laser fluence of 0.15 J $cm^{-2}$ and afterwards the proper ablation with a laser fluence of 1.50 J $cm^{-2}$ while the signal was recorded. This procedure was repeated without pre-ablation to compare the two obtained elemental distribution images. The size of the image was 1 352 µm x 320 µm. The operating parameters of LA and ICP-MS can be found in Table 0.5 in the appendix.

### 3.6.2 Leaching in an ultrasonic bath

The second approach to remove the Li accumulation in surface-near areas was to leach the LLTO substrates in an ultrasonic bath resulting in the removal of water-soluble lithium compounds. After leaching, the samples were dried using compressed air. Elemental distribution images after leaching the LLTO substrates for 0 seconds, 30 seconds, and 60 seconds in water in an ultrasonic bath were created and compared. Here, the first three layers were ablated. The image size was about 1 367 µm x 380 µm, and the measurement parameters are shown in Table 0.6 in the appendix.

### 3.6.3 Combination of both approaches and aging effects

To conclude this issue, a comparison of both approaches and an additional combination of both were conducted. Moreover, a one week-aged LLTO substrate, which was leached before to remove the Li excess from the sample surface, was also investigated. For the comparison, three different LLTO substrates were prepared. One untreated LLTO substrate was used as reference and for the pre-ablation approach, a second LLTO substrate was leached 60 seconds in an ultrasonic bath. The last LLTO substrate was leached again under the same conditions, but one week before measuring. Per sample five line scans were carried out whereby each time 10 layers were ablated. The operating parameters can be seen in Table 0.7 in the appendix.

## 3.7 Preparation of solid standards for quantitative LA-ICP-MS analysis

Matrix-matched solid standards were prepared for quantitative LA-ICP-MS analysis. The solid standards were produced by weighing out the appropriate powders, homogenising by grinding or mixing in a mortar, and pressing with a monoaxial compactor. For this purpose, two approaches were developed. On the one hand, lithium carbonate ($Li_2CO_3$) in different amounts was added to LLTO powder and on the other hand, the oxides of lithium, titanium, and lanthanum ($Li_2O$, $TiO_2$, and $La_2O_3$) were mixed. A schematic representation of the general processes during standard preparation is shown in Figure 3-6. The total sample amount of every pellet was approximately 0.50 g and the dimensions were 1.3 cm in diameter and a height of about 2 mm.

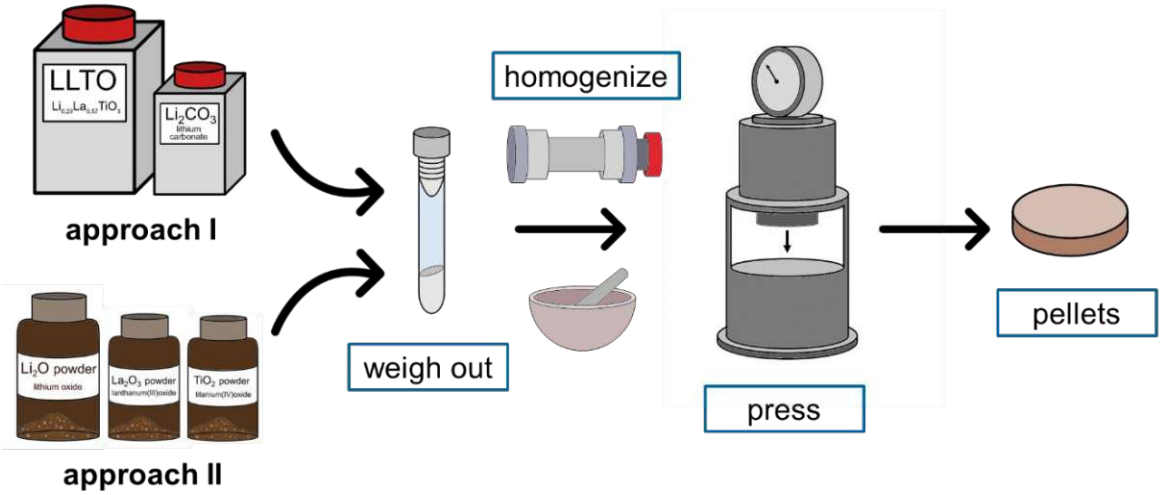


*Figure 3-6: Overview of the processes in the quantification approaches*

### 3.7.1 Optimization of standard preparation

To find out which standard preparation processes lead to as homogenous solid standards as possible, different orders of methods of powder pre-treatment were performed. In total, three pellets with the same amount of lithium but with different preparation steps were produced. For the first solid standard, the powders (LLTO and $Li_2CO_3$) were grounded individually, weighed out and homogenized in a mortar. Next, both powders were weighed out and grounded in a mill simultaneously. For the last pellet, the milling step was skipped, and the powders were only homogenized in a mortar after weighing out. For the measurement of the three solid standards, line scans using LA-ICP-MS were conducted. The measurement parameters of this experiment can be seen in Table 0.8 in the appendix.

### 3.7.2 LLTO powder spiked with lithium carbonate

Seven matrix-matched standards with a lithium concentration between approximately 1 and 3 wt.% were prepared according to the following procedure. Pre-dried LLTO- and $Li_2CO_3$ – powders (Sigma-Aldrich, United States, 99.997 % purity) were transferred to test tubes (polystyrene, VWR) in the appropriate quantities and weighed. Then, the mixed powders were grounded for 2 minutes with a frequency of 25 Hz using an oscillating mill (MM 400, Retsch, Germany). Finally, the powder was pressed for 3 minutes at 10 bar in the monoaxial compactor. The accurate lithium concentrations of the produced standards can be found in Table 0.11 in the appendix.

To evaluate homogeneity of the standards and the quality of this quantification approach, line scans of the matrix-matched standards were performed using LA-ICP-MS. The first four layers were removed through pre-ablation. Afterwards, five layers were evaluated for quantification. The operating conditions can be seen in Table 0.9 in the appendix.

### 3.7.3 Lithium oxide, titanium dioxide, and lanthanum oxide

As mentioned before, in the second quantification approach, lithium oxide ($Li_2O$), titanium(IV) oxide ($TiO_2$), and lanthanum(III) oxide ($La_2O_3$, Sigma-Aldrich, United States, 99.999 % purity) were used for producing matrix-matched standards. The pellets were prepared in the same way as in the approach described above. Five standards with a lithium concentration of 0 wt.% to 2 wt.% were prepared, with the intervals between the standards being approximately 0.5 wt.%. The exact lithium concentrations of the prepared pellets can be found in Table 0.12 in the appendix.

The solid standards were measured with LA-ICP-MS. Here, four pre-ablation layers were removed, and the following two layers were used for quantification. One layer consists of 10 single lines with a gap of 45 µm between the lines. Three patterns were measured per pellet. The operating parameters of LA and ICP-MS are shown in Table 0.10 in the appendix.

## 3.8 Quantitative LA-ICP-MS measurements of field-stressed LLTO substrates

### 3.8.1 Comparison of in vacuum and atmospheric pressure field-stressed LLTO substrates

For the quantitative LA-ICP-MS measurements, seven matrix-matched solid standards were produced. The pellets were produced out of $Li_2O$, $TiO_2$, and $La_2O_3$ in the same way described in 3.7 *Preparation of solid standards for quantitative LA-ICP-MS analysis*. Standards with lithium concentrations in the range of 0.0 wt.% to 1.5 wt.% were prepared. Besides the standards, the

field-stressed LLTO sample was prepared as described in 3.4 *Preparation of field-stressed LLTO substrates*. The conditions during polarisation can be taken from Table 3.2: *Overview of the conditions during polarization* and correspond to the conditions of experiments "E2" and "E3". The essential difference between the two samples is the atmosphere in which the polarization experiments were conducted.

Matrix-matched standards and both field-stressed LLTO substrates were analysed by LA-ICP-MS using the same operating parameters, which are shown in Table 3.4. On every standard one line scan was performed at five different locations on the pellet. Seven lines were ablated into the depth per position, whereby the first two lines were discarded for quantification. One ablated line has a length of 4 mm. Elemental distribution images of the field-stressed LLTO substrates were created. The size of the measured images of both samples was 2 639 µm x 1 140 µm. In total, ten layers of the substrates were ablated, and the generated signal was recorded.

*Table 3.4: Operating parameters of LA and ICP-MS during quantitative imaging of field-stressed LLTO substrates I*

| **Laser ablation** | | **Inductively coupled plasma mass spectrometry** | |
|---|---|---|---|
| Laser fluence | 1.25 J $cm^{-2}$ | RF power | 1 550 W |
| Beam size | 20 µm | Auxiliary gas flow | 0.80 mL $min^{-1}$ |
| Repetition rate | 100 Hz | Cool gas flow | 14.0 mL $min^{-1}$ |
| Overlap | 10 µm | Nebulizer gas flow | 0.75 mL $min^{-1}$ |
| Scan speed | 1 000 µm $s^{-1}$ | Dwell time per mass | 10 ms |
| He flow | 800 mL $min^{-1}$ | Measured Isotopes | $^{6}Li$, $^{46}Ti$, $^{138}La$ |

### 3.8.2 Comparison of field-stressed LLTO substrates with different applied voltages

As before, seven matrix-matched standards with lithium concentrations in the range of 0.00 wt.% to 1.50 wt.% were prepared (as described in 3.7.3 *Lithium oxide, titanium dioxide, and lanthanum oxide*). For each measurement new standards were prepared due to the instability of the produced pellets in ambient atmosphere. At this point, different voltages (2.5 V, 4.0 V, 6.0 V, and 10.0 V) were applied to the LLTO substrates. The polarization conditions can be found in Table 3.2: *Overview of the conditions during polarization* (E4 – E7).

The measurements of the matrix-matched solid standards were done in the following way: line scans on four different positions of every pressed pellet were performed, and ten layers were ablated. For the purpose of quantification, the first five layers were discarded due to lithium enrichment in surface-near layers. In order to investigate the depth of the lithium depletion

zone beneath the anode, depth profiles of the different field-stressed LLTO substrates were measured. In every layer, an area of approximately 800 µm x 200 µm was ablated. Additionally, an elemental distribution image of sample E4, which was polarized with a voltage of 2.5 V, was produced.

*Table 3.5: LA and ICP-MS operating parameters during the analysis of LLTO substrates polarised with different voltages*

| **Laser ablation** | |
|---|---|
| Laser fluence | 1.25 J $cm^{-2}$ |
| Beam size | 20 µm |
| Repetition rate | 100 Hz |
| Overlap | 10 µm |
| Scan speed | 1 000 µm $s^{-1}$ |
| He flow | 800 mL $min^{-1}$ |

| **Inductively coupled plasma mass spectrometry** | |
|---|---|
| RF power | 1 550 W |
| Auxiliary gas flow | 0.80 mL $min^{-1}$ |
| Cool gas flow | 14.0 mL $min^{-1}$ |
| Nebulizer gas flow | 0.72 L $min^{-1}$ |
| Dwell time per mass | 10 ms |
| Measured Isotopes | $^{6}Li$, $^{46}Ti$, $^{138}La$ |

# 4 Results and Discussion

## 4.1 Optimization experiments using LA-ICP-MS

This chapter describes which isotopes were selected for the succeeding measurements. Moreover, the influence of the laser fluence, the helium flow in the LA device, and the overlap of the laser pulses on the recorded signals were examined. After these initial experiments, optimal operating parameters for further measurements were chosen. Additionally, the porosity of LLTO is shown by microscopic images of the surface, and the resulting problems regarding the spot size and possible solutions are discussed.

### 4.1.1 Selected Isotopes

The nominal composition of LLTO ($Li_{0.29}La_{0.57}TiO_3$) before polarizing is made up of 1.14 wt.% lithium, 44.72 wt.% lanthanum, 27.04 wt.% titanium, and 27.11 wt.% oxygen. That means lanthanum, titanium, and oxygen are major components of LLTO, whereas lithium is a minor constituent. In LLTO, none of the examined elements are present in traces, therefore, signal intensities are generally very high. To protect the detector from oversaturation, isotopes with a low natural abundance were selected for the measurements. More precisely, the following isotopes were chosen: $^{6}Li$ (7.40 % abundance), $^{46}Ti$ (8.00 % abundance), and $^{138}La$ (0.09 % abundance). Furthermore, the first ionisation energy of all interesting elements lies in the same low range between 5.3 eV and 5.6 eV. So, no troubles with low ionisation probabilities during the ionisation in the plasma because of high ionisation energies were expectable.

### 4.1.2 Spot size

When looking at a microscopic image of a LLTO substrate, as shown in Figure 4-1, it can be observed that the surface and the bulk material are porous. The pore sizes are different and lie in the range of 5 µm to > 25 µm. This material property must be taken into account regarding a suitable choice of the laser spot size. If the spot size is smaller than most pores, the signal will be very unstable. For example, in such a pore, one species can be adsorbed better, and then the signal fluctuates strongly dependent on whether the laser is focused on a pore or not. First attempts were made with a spot size of 5 µm and 10 µm in diameter. However, it turned out that these spot sizes were too small to receive a stable signal. A stable signal is gained during experiments with a spot size of 20 µm in diameter. Besides the increase in the spot size, there exists another method to obtain a stable signal. Normalization of the lithium signal to the lanthanum signal leads to a more stable signal due to the compensation of different amounts of ablated material. So, a spot size of 20 µm in diameter and normalization of the signal was used for the following experiments to obtain accurate results.

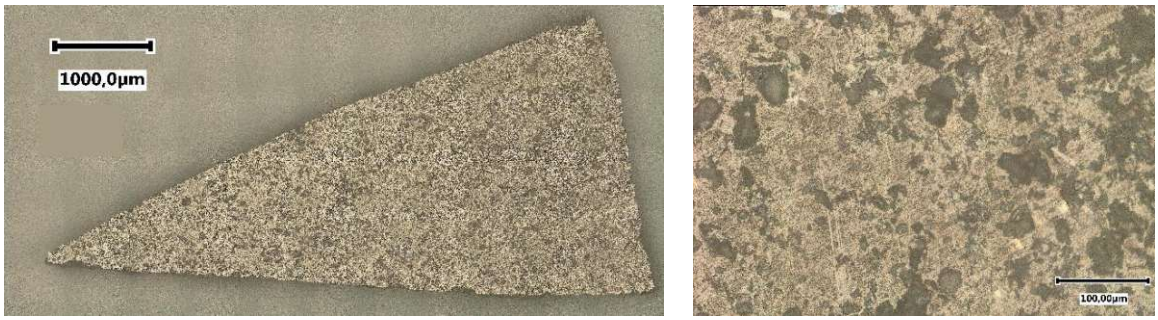


*Figure 4-1: Microscopic images of an LLTO substrate*

### 4.1.3 Laser fluence

During the optimization of the laser fluence for further measurements, line scans were performed with pre-ablation, using laser fluences between 0.5 J cm$^{-2}$ and 2.5 J cm$^{-2}$. Significant results of this study can be found in Figure 4-2 and Figure 4-3. Figure 4-2 shows on the left side the measured $^{6}$Li signal intensity at different laser fluences. The higher the laser fluences, the higher the lithium signal intensities. Higher laser fluence means a higher energy per area for ablation, leading to a higher amount of ablated material. When more material is removed from the sample and introduced into the plasma, more ions of one species are detected and therefore, the signal intensity of this species increases. This trend is shown in Figure 4-2 for the lithium signal and was also observed for the titanium and lanthanum signal.

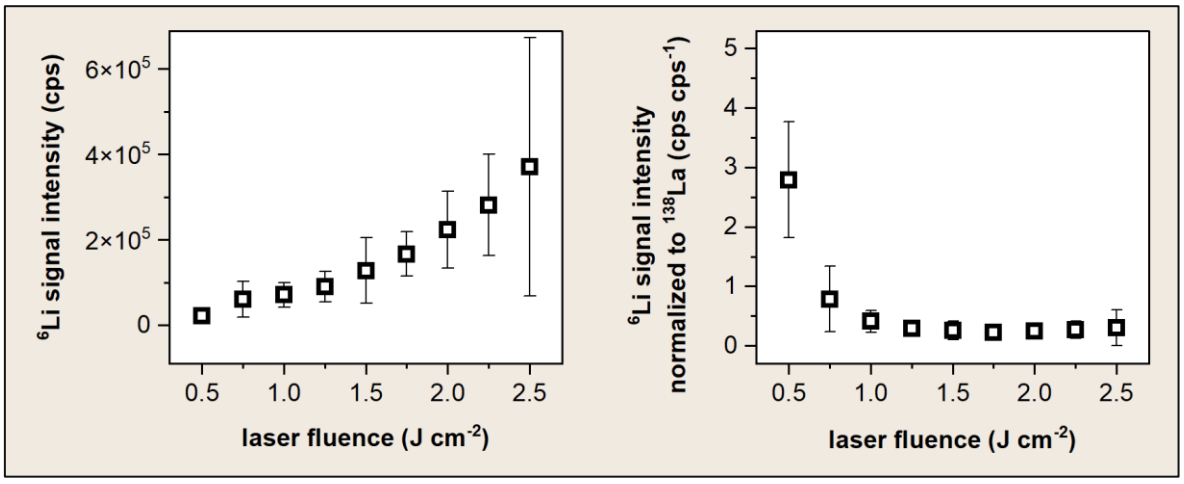


*Figure 4-2: Influence of the laser fluence on the lithium signal. In this study, experiments with different laser fluences between 0.5 J cm$^{-2}$ and 2.5 J cm$^{-2}$ were performed. On the left side, there can be seen the $^{6}$Li signal in dependence on the laser fluence, and on the right side, the $^{6}$Li signal is normalized to the $^{138}$La signal.*

As mentioned before, normalizing the signal of one element species to another is a standard method to adjust varying amounts of ablated material. So, in Figure 4-2, on the right side, the normalized $^{6}$Li signal is shown. Here, the lithium signal is normalized to the $^{138}$La signal. In this graph, it is visible that the laser fluence influences the normalized lithium signal. At laser fluences above approximately 1.0 J cm$^{-2}$, the signal is stable, and the laser fluence does not seem to affect the normalized signal. The error bars in the figure are the results of the signal

standard deviation of a line scan. However, if the laser fluence is reduced below this threshold (< 1.0 J cm$^{-2}$), the normalized lithium signal increases. Through normalization and if a suitable laser fluence is chosen the size of the error bars is minimized. In Figure 4-3, the $^{138}$La signal is normalized to the $^{46}$Ti signal. Here, the normalized signal is stable at all measured laser fluences, even at laser fluences below 1.0 J cm$^{-2}$. From this, it can be concluded that if the laser fluence is too low, lithium is preferentially removed compared to lanthanum and titanium and thus a normalized signal suggests a lithium surplus which does not exist in this form. For further measurements, this means that the laser fluence must be above the limit of 1 J cm$^{-2}$. The following experiments were performed with a laser fluence of 1.50 J cm$^{-2}$, since this value leads to sufficiently high signals. Later measurements were performed with a laser fluence of 1.25 J cm$^{-2}$ due to the exchange of the mass spectrometer's detector and, therefore, higher sensitivities. These investigations show that it is crucial to thoroughly optimize the laser fluence to avoid under- or over determination of certain elements. So, the selection of a proper laser fluence should not be underestimated.

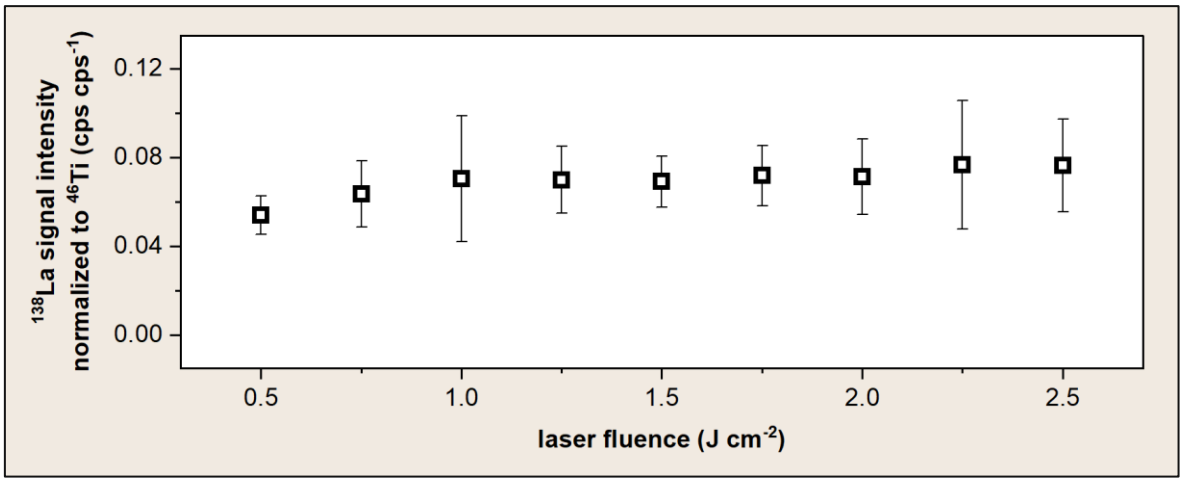


*Figure 4-3: Outcomes of the normalized lanthanum signal in dependence on the laser fluence*

### 4.1.4 Helium flow rate

To figure out the influence of the helium flow rate in the LA device on the wash-out behaviour and the signal intensity, line scans at different helium flows were performed. Helium flow rates between 300 mL min$^{-1}$ and 1 000 mL min$^{-1}$ in steps of 100 mL min$^{-1}$ were investigated. Some of the results are shown exemplarily in Figure 4-4.

It was observed that the wash-out time is at a minimum in the range of 700 mL min$^{-1}$ to 900 mL min$^{-1}$ helium flow. In this range, the wash-out time is approximately 50 ms. When reducing the helium flow below 700 mL min$^{-1}$, the wash-out time is significantly increased. For example, if the helium flow is decreased from 700 mL min$^{-1}$ to 600 mL min$^{-1}$, the wash-out time is doubled, and if the helium flow is further reduced to 600 mL min$^{-1}$, the wash-out time is increased by a factor of three. However, helium flow rates above 900 mL min$^{-1}$ do not lead to any improvement in the wash-out time, as can be seen in Figure 4-4. Therefore, additional measurements were carried out with helium flow rates in the range of 700 mL min$^{-1}$ to 900 mL min$^{-1}$.

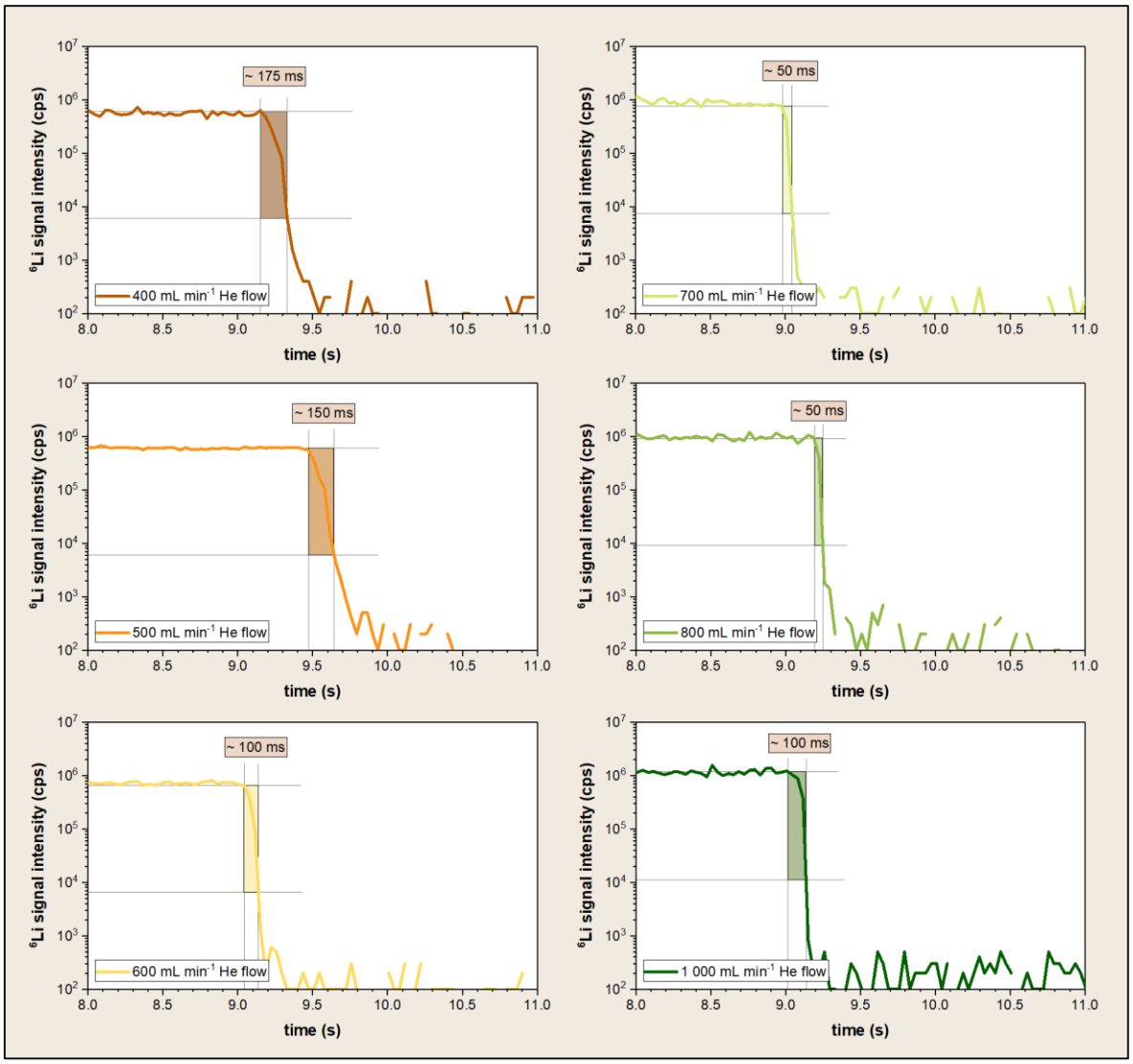


*Figure 4-4: Line scans with a LA-ICP-MS instrument at different helium flow rates in the LA device were performed. Helium flow rates in the range of 300 mL min$^{-1}$ to 1 000 mL min$^{-1}$ in steps of 100 mL min$^{-1}$ were investigated. An optimal helium flow was observed between 700 mL min$^{-1}$ and 900 mL min$^{-1}$. Both at lower and at higher helium flow rates, the wash-out times increase. The change in lithium signal intensity, as well as titanium and lanthanum signal intensities with increasing helium flows, are negligible.*

During these experiments, no significant differences in the lithium signal intensity for different helium flow rates were observed. In the range of 700 mL min$^{-1}$ and 1 000 mL min$^{-1}$ He flow, the $^{6}$Li signal intensity is approximately $10^{6}$ counts per second and below a helium flow of 700 mL min$^{-1}$, the signal intensity is negligibly lower. Besides the lithium signal intensity of $^{6}$Li, the change of the $^{46}$Ti and the $^{138}$La signal with the helium flow rate is also negligible. The further experiments were performed using a He flow rate of 800 mL min$^{-1}$.

### 4.1.5 Overlap

The first measurements were performed using the measurement parameters of method 1, which can be seen in Figure 4-5. It was determined that the ablation depth of this setting was roughly 500 nm per layer. The overlap was reduced to enhance the depth resolution and to enable a better investigation of the depletion zone beneath the anode. Additionally to decreasing the overlap, the repetition rate was decreased to keep the scan speed below 2 000 µm $s^{-1}$. The measurement parameters of the four tested approaches can be seen in Figure 4-5.

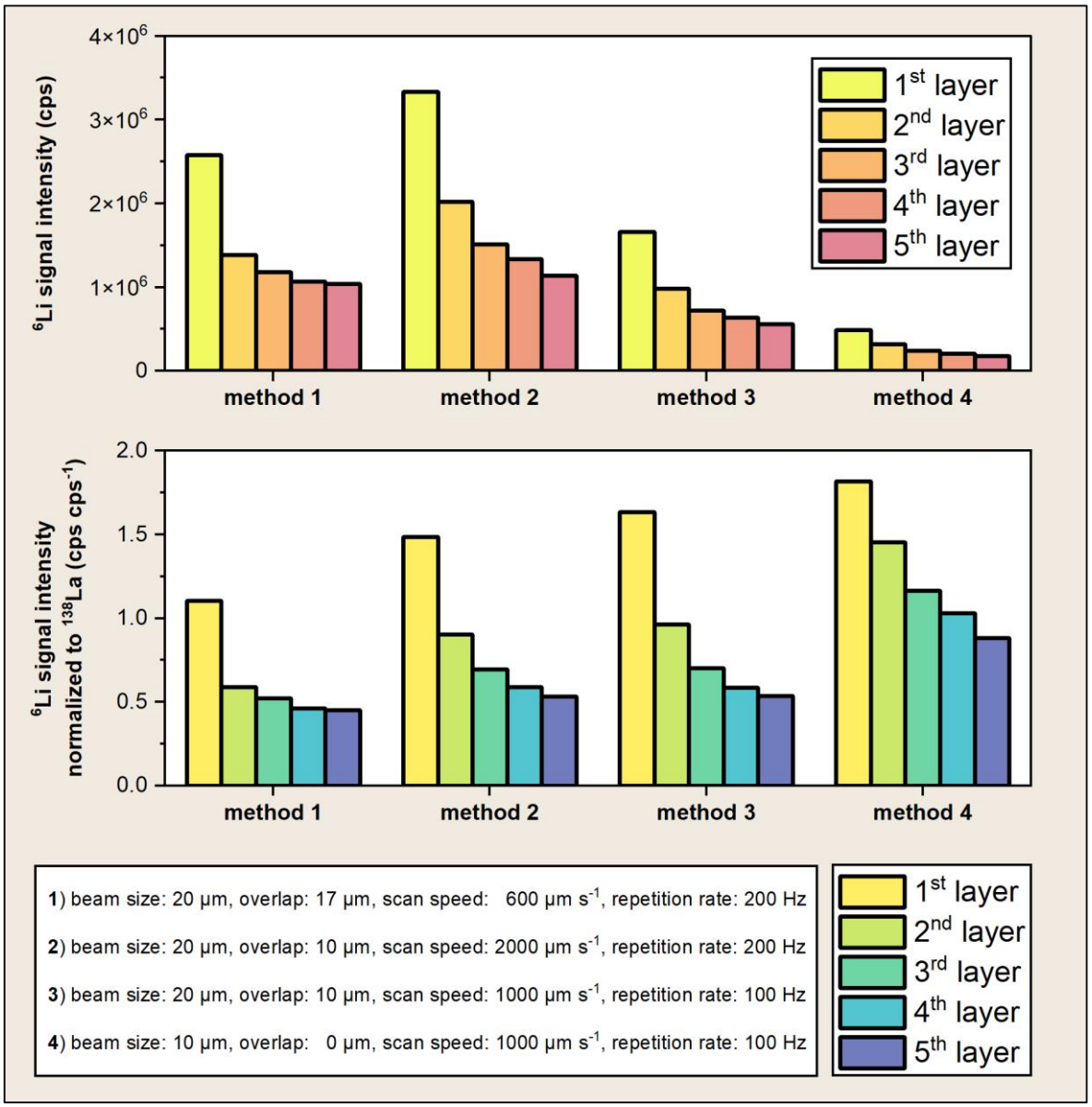


*Figure 4-5: Improvement of the depth resolution through changing of the overlap and other measurement parameters. four different methods, which are listed in the table below, were applied and examined. Five layers of LLTO substrate were ablated, and the $^6$Li signal intensity (upper diagram) and the normalized $^6$Li signal intensity (lower diagram) were compared.*

The upper diagram in Figure 4-5 shows the $^{6}Li$ signal intensity of the first five layers for the four methods, while the normalized $^{6}Li$ signals are shown in the lower diagram. The upper graph exhibits that method 2 removes the most material, and therefore no improvement in the depth resolution can be achieved using these parameters. The methods 3 and 4 lead to lower amounts of ablated material compared to method 1 and hence to a lower ablation rate per layer and a better depth resolution.

The lower graph in Figure 4-5 shows that if the lithium signal is normalized, the signal after the removal of the first few layers (Li excess) is independent of the change in the measurement conditions. The 3$^{rd}$ and the 4$^{th}$ layer of methods 1-3 possess approximately the same normalized signal. Due to the significantly lower ablation rate in method 4, more layers would need to be removed to remove the lithium excess and to reach normalized values as low as in method 1-3. The qualitative measurements were performed with the measurement parameters of method 1, but later measurements were carried out with a reduced overlap and a reduced repetition rate, as in method 3, as this led to a significant improvement in depth resolution. Profilometric measurements of the ablation rate revealed that 100 nm material is removed per layer using the third method, while the ablation rate in the first method is 500 nm per layer.

## 4.2 Qualitative LA-ICP-MS measurements of LLTO substrates

### 4.2.1 Results of non-polarized LLTO substrates

Elemental distribution images of non-polarized LLTO substrates were created after LA-ICP-MS measurements. The images of the $^{6}Li$ signal intensity and the normalized $^{6}Li$ signal are shown in Figure 4-6.

It can be seen from the $^{6}Li$ images (Figure 4-6) that the first ablated layer indicates a lithium accumulation compared to the further ablated layers. The signal intensity in the first layer is in the range of $5x10^{5}$ cps and in the following layers are between $1x10^{5}$ and $3x10^{5}$ cps. The $^{6}Li$ signal is stabilized after removing the first layer (~ 500 nm). The normalized $^{6}Li$ images also show a higher signal in the first layer. A higher normalized signal can arise because, on the one hand, the lithium amount is more elevated and on the other hand, the lanthanum amount is lower. From the second to third layer onwards, both the $^{6}Li$ signal and the normalized $^{6}Li$ signal ratio become stable. To determine the reason for a higher normalized lithium signal, the normalized $^{46}Ti$ signal is depicted in Figure 4-7. No enrichment can be found in the normalized $^{46}Ti$ image, the Ti/La ratio is constant over all layers. These findings reveal that there is no change in the lanthanum and the titanium stoichiometry. However, there is an apparent lithium enrichment in the first 500 nanometres. After removing this surface-near lithium accumulation by ablation, stable signals are obtained. The reasons for this lithium enrichment and solutions to remove this are explained in greater detail in 4.3 *Removal of the Li accumulation in surface-near layers*.

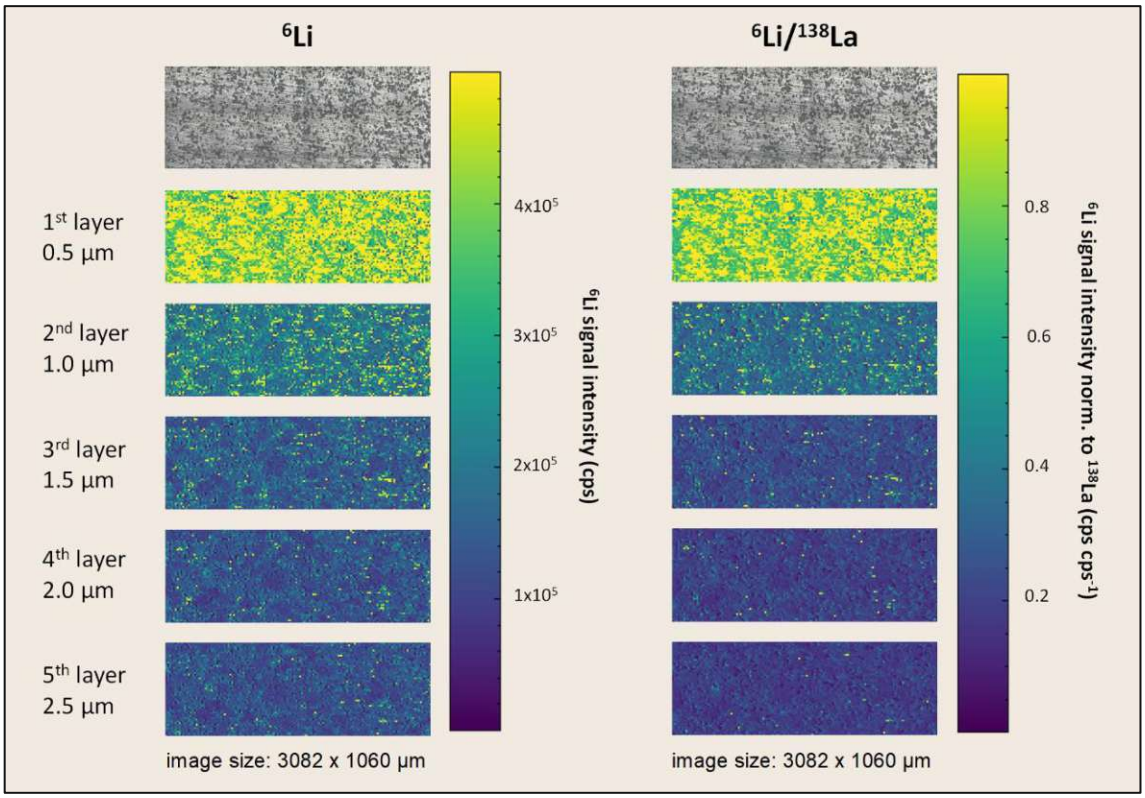


*Figure 4-6: Images of non-polarized LLTO substrates. The $^{6}$Li signal is shown on the left side and the $^{6}$Li to $^{138}$La signal ratio is depicted on the right side. In both cases, the lithium accumulation in the first layer is clearly visible. After removing the first layer, both signals get stable.*

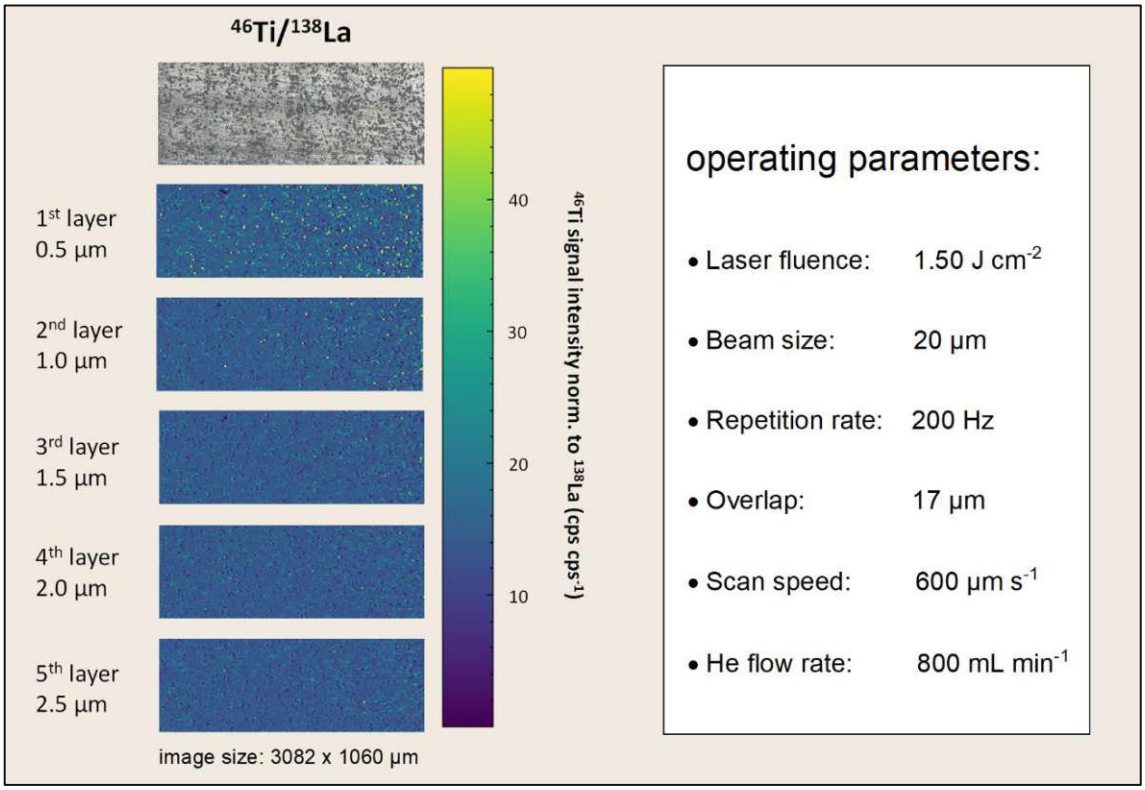


*Figure 4-7: Images of the $^{46}$Ti to $^{138}$La signal ratio. In sum, five layers of 500 nm, each were ablated by LA and analysed using ICP-MS. Here, no accumulation of titanium or lanthanum can be determined. The signal is approximately constant over all five ablated layers. These findings confirm that there is a lithium accumulation in the first layer and not a lanthanum depletion. On the right side, an overview of the operating parameters of LA is listed.*

### 4.2.2 Results of polarized LLTO substrates

Additionally, to the previously analysed non-polarized LLTO substrates, several field-stressed LLTO substrates were investigated after application of different bias voltages at slightly elevated temperatures. The first sample (named E1) was polarized at increasing voltages of 5 – 10 V at a temperature of 100 °C for 90 minutes. Three layers of the polarized LLTO substrates were examined. The results are shown in form of elemental distribution images in Figure 4-8, here, the $^{6}$Li signal normalized to $^{138}$La is depicted. A lithium depletion beneath the anode was expected after applying a voltage higher than the calculated stability window of LLTO. Besides the lithium depletion at the anode, a homogenous enrichment of lithium in a larger area around the cathode was presumed. The effect of lithium depletion can be seen in the images in Figure 4-8. There is a significant lithium depletion visible in the area under the Pt-anode in the first and the second layer. In the third layer, no clear depletion is obtained. However, lithium accumulation around the cathode is not detected. It is possible that the enrichment is not in a small, strongly enriched area underneath the cathode but instead in a large, weakly enriched area, as suggested from the rather diffuse and large coloration area. The change in concentration is then so small that the electrochemically induced Li enrichment is small compared to the surface-near Li enrichment and the precision of the method is insufficient, and therefore, no lithium accumulation could be measured. Additionally, as mentioned above, during the qualitative investigation of non-polarized LLTO, a lithium accumulation in surface-near layers of polarized LLTO was detected. Due to the lithium accumulation and the consequent, strongly varying lithium signal in the first layer, the identification of lithium depletion in the first layer is slightly obscured. Based on those problems, in chapter 4.3 *Removal of the Li accumulation in surface-near layers* methods to remove this lithium accumulation are discussed. In later imaging experiments methods for the removal of the lithium excess were applied.

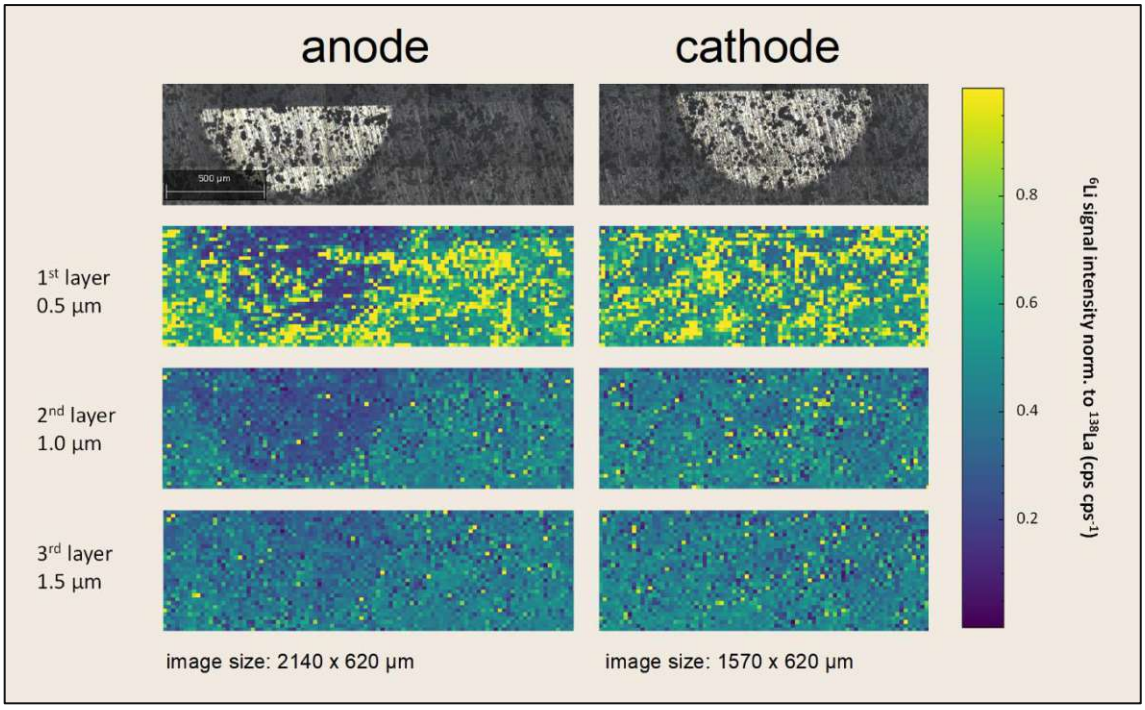


*Figure 4-8: Elemental distribution images of a field-stressed LLTO substrate. In the image, the normalized $^{6}$Li signal is depicted. Beneath the anode, a clear lithium depletion in the first and second layers is obtained.*

### 4.2.3 Comparison between polarized and non-polarized LLTO substrates

This chapter summarises the results of the qualitative investigation of non-polarized LLTO as well as the findings of the measurement of the polarized LLTO substrate. Compared to the chapters above, the results of the measurements are not shown in the form of elemental distribution images but in the form of profiles. The outcomes of the qualitative investigations are displayed in Figure 4-9.

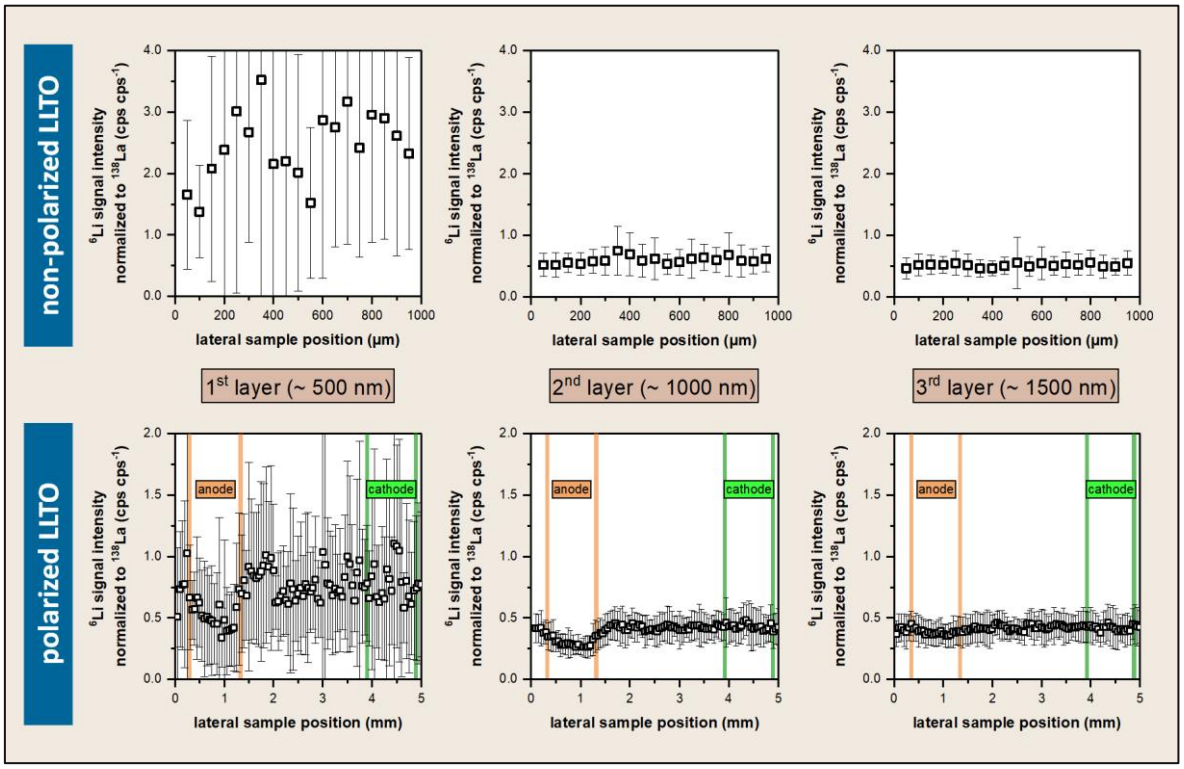


*Figure 4-9: Outcomes of the qualitative measurements of a non-polarized as well as a polarized LLTO substrate. The results of the first three layers of both investigated samples are shown in the form of profiles. In both cases, non-polarized and polarized, a lithium enrichment in the first layer was obtained. Beneath the anode of the polarized LLTO sheet, a lithium depletion zone occurs in the first two ablated layers (conforms to a depth of approximately 1 µm).*

Beginning with the results of the non-polarized LLTO substrate, in the first layer, a lithium enrichment compared to the following layers was obtained. Besides this lithium accumulation, the lithium signal varies strongly, which can be seen from the huge error bars. After the removal of the first layer, the following layers show lower and constant normalized lithium signal ratios of about 0.4 to 0.5. For the polarized LLTO substrate, the lithium accumulation in the first layer is also visible. However, it is slightly lower. As mentioned above, due to the signal instability, the lithium depletion beneath the anode is challenging to recognise in the first layer. However, in the second layer, the lithium depletion was obtained. A lithium accumulation around the cathode could not be determined from the measurement findings.

To get a better overview of the local lithium depletion beneath the anode, it is zoomed into the area of the anode. The enlargement of the lithium depletion zone in the second layer can be seen in Figure 4-10. Beyond the area under the anode, the normalized lithium signal is about 0.4, and in the area below the anode, the signal ratio is approximately 0.25. So, the lithium

depletion is clearly visible in the second layer of the polarized LLTO sheet. In the third layer, no significant lithium depletion zone was found. Thus, the depth of the lithium depletion zone can be estimated as approximately 1 µm.

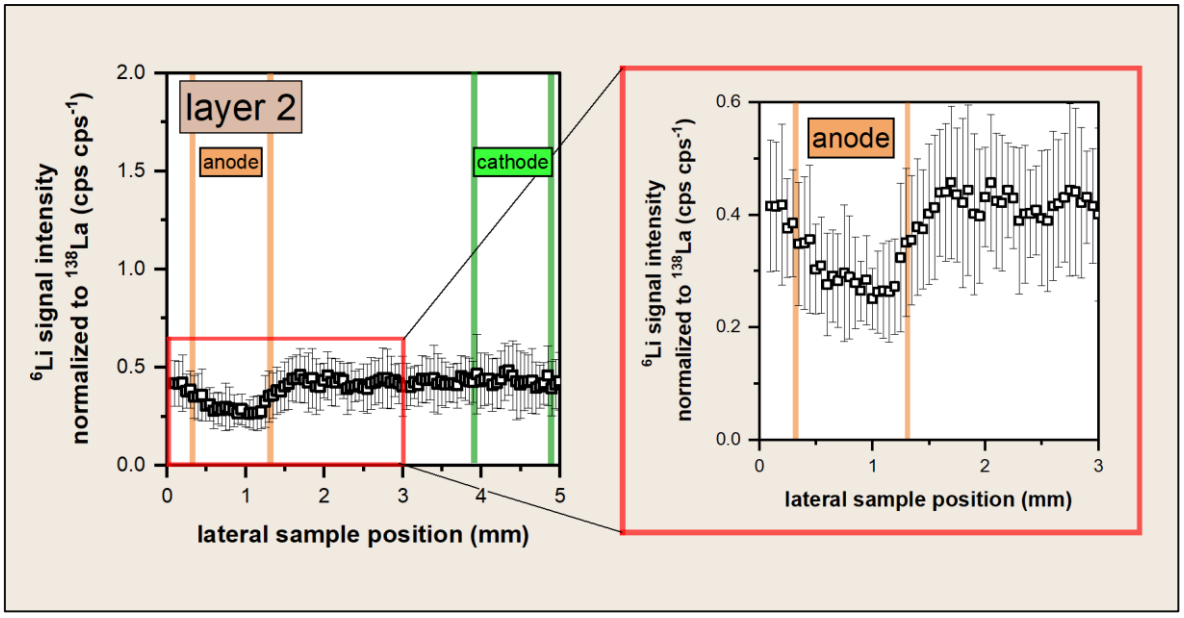


*Figure 4-10: Enlargement of the area beneath the anode of the qualitative investigation of a polarized LLTO substrate. The predicted lithium depletion beneath the anode is in the second layer, clearly present. The signal ratio decreases from 0.4 outside the zone below the anode to as low as approximately 0.25 beneath the anode.*

## 4.3 Removal of the Li accumulation in surface-near layers

As described in the results of the qualitative study, a lithium enrichment in the surface-near layers (approximately first 500 nm) of non-polarized as well as polarized LLTO substrates was observed. Besides the lithium accumulation, the lithium signal is strongly fluctuating in this area. Due to these effects, the lithium depletion in field-stressed LLTO samples is hard to observe in the first few layers. Thus, in this chapter, attempts are described which were made to remove this lithium excess and identify the origin of the accumulation on the surface.

### 4.3.1 Pre-ablation of LLTO substrates

Based on a myriad of preliminary experiments, it was assumed that ablation using low laser fluences leads to an amplified removal of lithium compared to lanthanum and titanium, presumably due to preferred removal of Li-rich secondary phases at the surface. To confirm this assumption, sample spots on LLTO substrates were measured using a laser fluence of 1.50 J cm$^{-2}$ without pre-ablation and likewise after pre-ablation with different laser fluences. The results of these preliminary investigations are shown in the form of a bar chart in Figure 4-11.

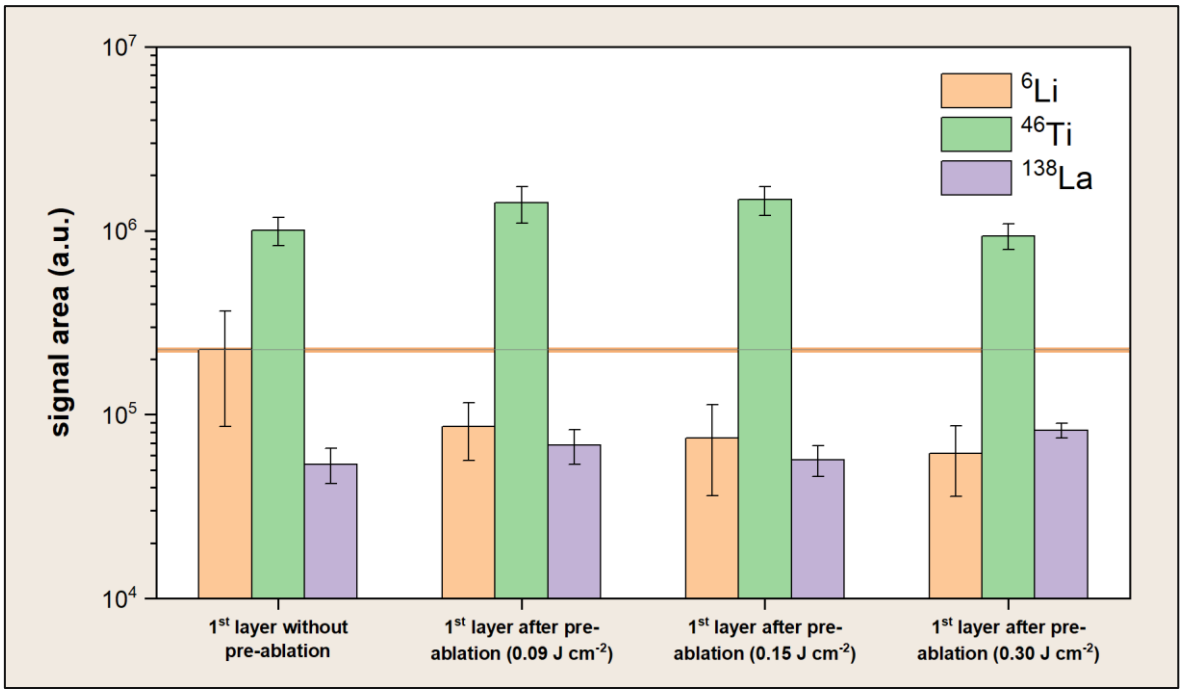


*Figure 4-11: Spot measurements on an LLTO substrate without pre-ablation as well as with pre-ablation. Pre-ablations with different laser fluences were performed. By this method, the lithium enrichment in surface-near layers is partly removed, which is evident from the reduced Li signal after pre-ablation.*

The first three bars in the figure above belong to the area of the integrated lithium, titanium, and lanthanum signals when a spot on the untreated (without pre-ablation) LLTO substrate was ablated and measured. So, the integrated $^6$Li signal of this measurement is taken as the reference amount of ablated lithium. The orange line in Figure 4-11 represents a reference value, allowing better comparison of the results of further measurements.

The essential findings of these preliminary experiments are that when pre-ablation is performed before the actual ablation and signal recording, the lithium signal decreases and hence the lithium excess in surface-near layers is reduced. The lithium signal reduction can be clearly seen in the figure above through the gap between the orange line and the orange bars. Noteworthy, the ablation of La and Ti is minimal at low fluence, as shown previously by the fluence optimization experiments.

The outcomes of these pre-ablation experiments indicate that through ablation using low laser fluences, preferably lithium is removed compared to titanium and lanthanum. The titanium and the lanthanum signal are fairly constant regardless of pre-treatment. In addition, hardly any information is lost through pre-ablation with such a low laser fluence since minimal layer thicknesses are ablated.

To further investigate the effectiveness of this approach for the elimination of the lithium surface enrichment and to make it visually more comprehensive, further measurements were carried out, and elemental distribution images were created. Therefore, two sample areas, one area with pre-treatment in the form of pre-ablation (three layers with a laser fluence of 0.15 J cm$^{-2}$ were pre-ablated) and one area without pre-ablation, were analysed.

The results of these measurements can be seen in Figure 4-12. There is a clear difference between the first layer without pre-ablation and the first layer with pre-ablation. The normalized lithium signal is significantly higher in the sample area without pre-ablation than in the sample area where a pre-ablation was performed before measuring. Furthermore, no clear differences between the images of the following layers were observed. Besides the elemental distribution images of the five ablated layers, microscopic images of the analysed sample before and after ablation are shown in Figure 4-12.

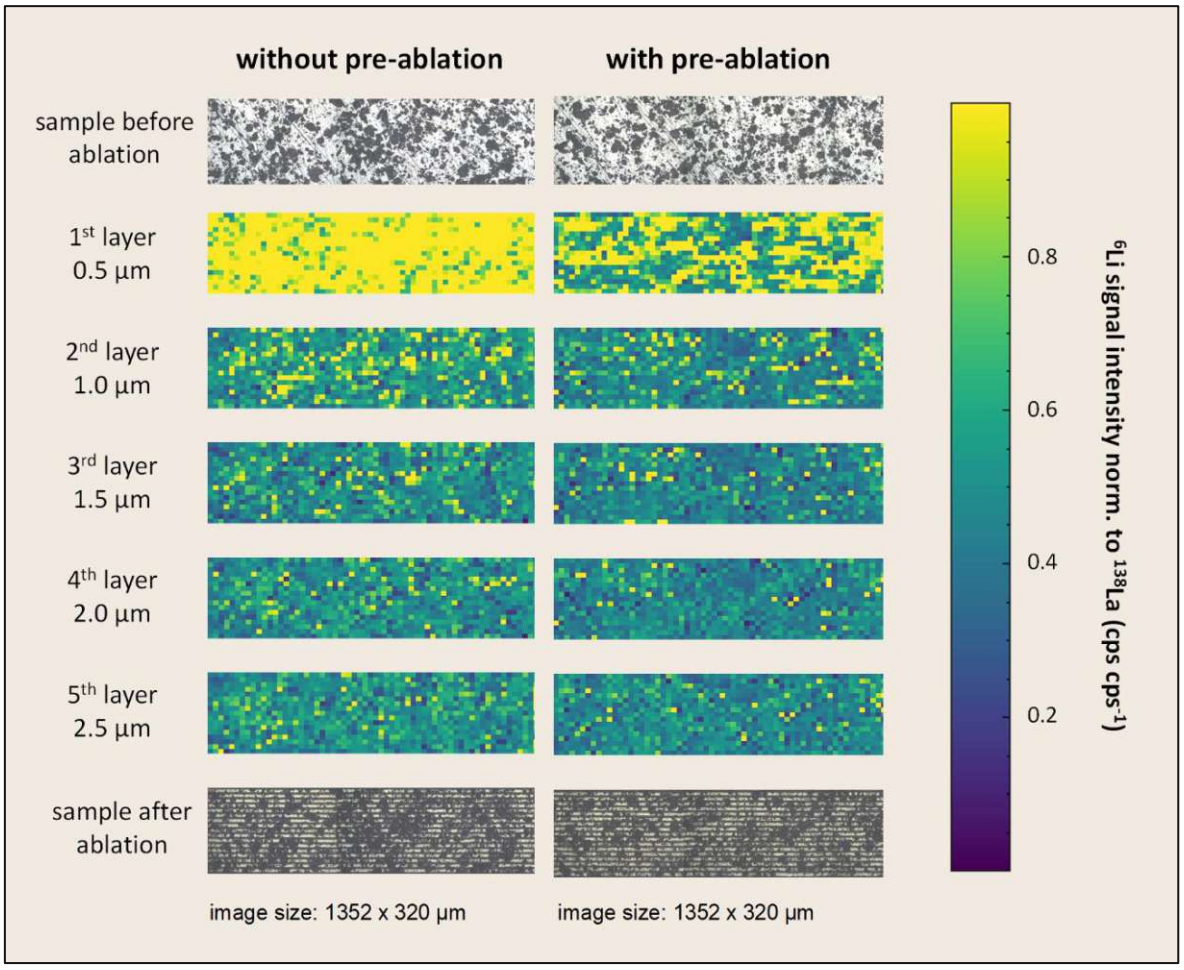


*Figure 4-12: Lithium distribution images of a sample area of LLTO with and without pre-ablation*

### 4.3.2 Leaching of LLTO substrates in an ultrasonic bath

Apart from the before mentioned method to remove the lithium enrichment in surface-near layers, a second approach was developed for this purpose. If it is assumed that the lithium accumulation occurs due to the deposition of soluble lithium compounds in pores during the manufacturing process, then leaching in an ultrasonic bath could be an option for the removal of this excess lithium. LLTO substrates were leached for different time periods in ultrapure water in an ultrasonic bath. As a reference, an LLTO substrate without pre-treatment in an ultrasonic bath was investigated to be able to evaluate the success of this approach.

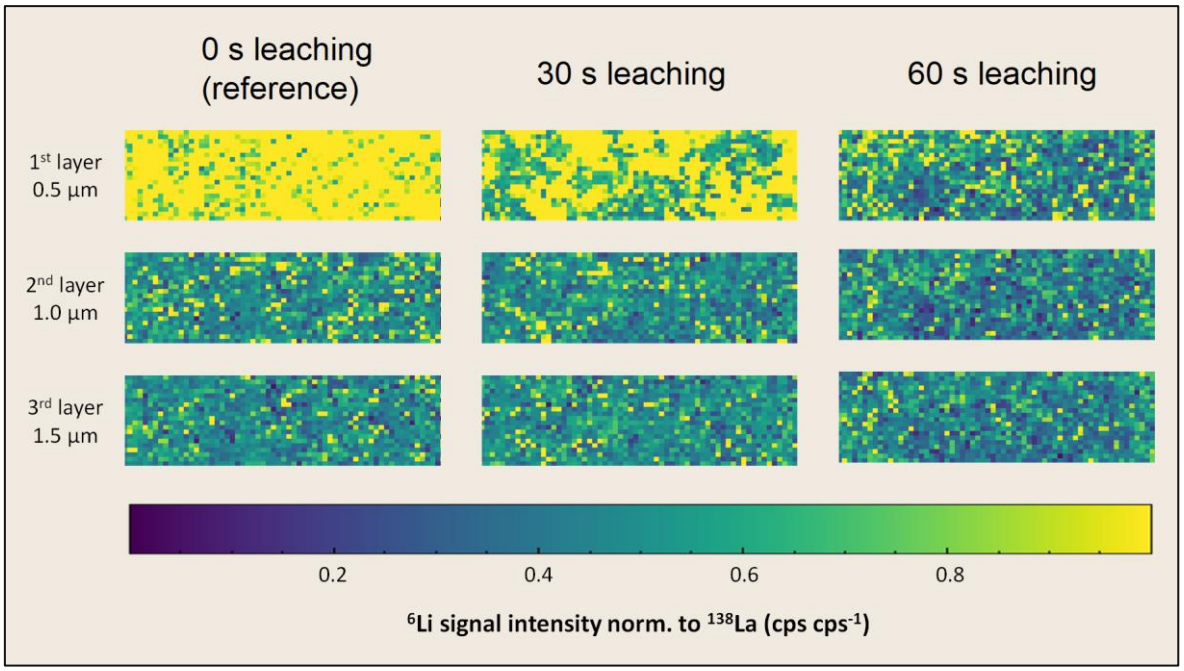


*Figure 4-13: Lithium distribution images of an LLTO substrate before and after leaching in an ultrasonic bath*

In Figure 4-13, the outcomes of the measurements of LLTO substrates after pre-treatment in an ultrasonic bath and the reference are shown. When comparing the first layers of the reference (0 s leaching) and both leached samples, it can be concluded that after a 60 second stay in an ultrasonic bath the lithium excess will be removed completely. 30 seconds of leaching in an ultrasonic bath only leads to a partial removal of the lithium enrichment in the first layer. The following layers seem to be approximately equal in all three cases. Leaching in an ultrasonic bath also results in the removal of the lithium accumulation and is, therefore an appropriate approach to improve the investigation of the lithium depletion within the first layer.

### 4.3.3 Application of both approaches on LLTO substrates and ageing effects

To conclude the chapter on the removal of lithium enrichment at the surface, both above mentioned approaches were applied individually and in combination on LLTO substrates and line scans were performed. Additionally, the effect of ageing of the already leached sample was investigated by performing the leaching process in an ultrasonic bath one week before the measurement. The findings of these experiments are depicted in Figure 4-14.

For each substrate, 10 layers into depth were measured. The normalized lithium signals of these 10 layers are shown in Figure 4-14. On the x-axis, the layer number and on the y-axis, the $^{6}$Li signal intensity (normalized to the $^{138}$La signal intensity) are plotted. It is important to remark that the scale of the y-axis is scaled different in the four diagrams.

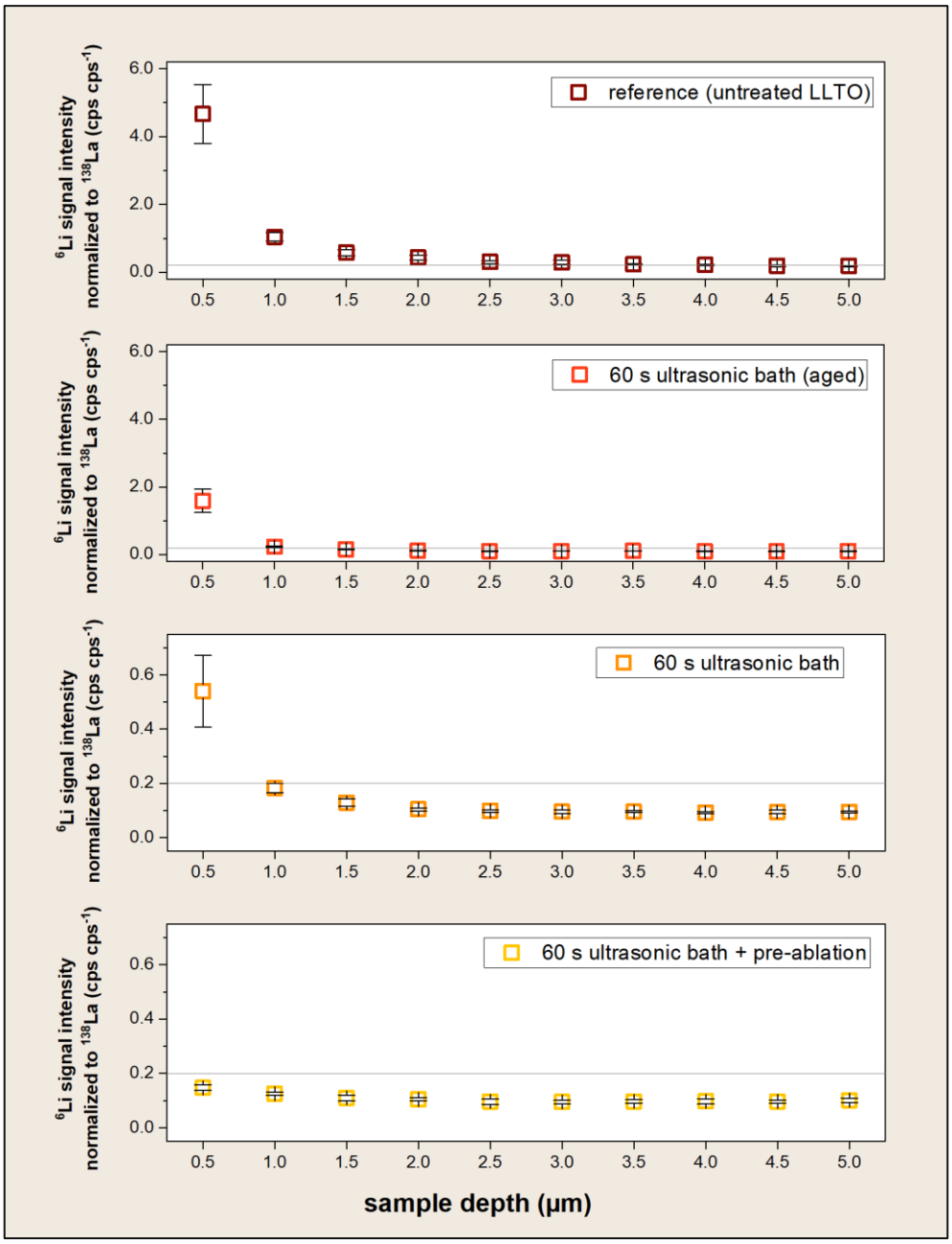


*Figure 4-14: Removal of the lithium accumulation in surface-near layers through different approaches*

Looking at the results of the reference (diagram at the top in Figure 4-14), it can be seen that most of the lithium enrichment is removed after ablating the first layer. However, a constant normalized lithium signal of about 0.2 is only reached after four to five layers. If the results of the reference sample are compared with those of the LLTO substrate that was leached for 60 seconds in an ultrasonic bath, it is noticeable that the lithium enrichment in the first layer is about one order of magnitude smaller after leaching. Additionally, a roughly stable signal is already obtained after the first ablated layer. The graph indicates that the normalized lithium signal decreases compared to the reference due to leaching in the ultrasonic bath. After a removal of 2 µm the normalized lithium signal of the untreated LLTO (reference) does not change anymore. The grey auxiliary lines in every diagram correspond to this constant normalized lithium signal of the reference (0.2). The diagram at the bottom (60 s ultrasonic

bath + pre-ablation), where in addition to leaching, also a pre-ablation was carried out, shows that this approach is a very effective method to remove the lithium accumulation. Finally, a leached and afterwards aged sample was investigated. Here, it is noticeable that there is a higher lithium enrichment in the first layer compared to the accumulation of the unaged, leached substrate. Indicating a Li diffusion from the bulk to the surface if given enough time.

The discussed findings lead to the assumption that it can be assumed that lithium enrichment does not only originate from soluble lithium compounds adsorbed in the pores. If this would be the case, the increase in enrichment due to ageing could not be explained. The effect that occurs during ageing suggests that the lithium accumulation in the surface-near areas arises also due to the Li diffusion from the bulk to the surface and reactions of LLTO with parts of the ambient atmosphere. Especially moisture and $CO_2$ may react with Li-ions and form $Li_2CO_3$ and LiOH. For these reasons, pre-ablation immediately before the actual ablation is an efficient method. However, leaching in an ultrasonic bath and immediate measurement of the sample is also an option.

## 4.4 Preparation of solid standards for quantitative LA-ICP-MS analysis

### 4.4.1 Optimization of the standard preparation procedure

To study the stochiometric changes during polarization more quantitatively, quantification of lithium is necessary. Therefore, matrix-matched standards were produced. Two different approaches were developed, both having in common that solid pellets were pressed out of powders. The pellet preparation is accompanied by many pre-treatment steps, such as milling in an oscillating mill or homogenising in a mortar. To achieve a sufficiently homogeneous pellet required for a constant signal and low standard deviations, three different standard preparation procedures were trialled:

(i) Initial powders were individually milled, then weighed out, and finally homogenised together in a mortar.

(ii) Initial powders were weighed out and ground together afterwards.

(iii) Initial powders were weighed out and then only homogenised together in a mortar.

After the preparation of pellets with LLTO- and $Li_2CO_3$-powders using the mentioned three approaches, LA-ICP-MS line scan measurements were performed. The outcome of this experiment is shown in Figure 4-15. The signal stability in depth and the extent of the standard deviation were compared between the three approaches. The two upper diagrams show that if milling was included in the preparation procedure, a constant signal in the depth is obtained.

However, an unstable signal is received, if the milling step was skipped, and the powders were only homogenised in a mortar, as in pellet 3. Especially after 15 layers, the normalized lithium signal starts to be unstable and varies significantly. When evaluating the quality of the pellet preparation based on the extent of the standard deviation, approach 2 leads to the best results. The highest standard deviations of the normalized lithium signals were obtained when the powders were only homogenized in a mortar, without milling. Based on these results, the preparation procedure of the second pellet, including a milling process after mixing the powders, was used for the further preparations of matrix-matched standards.

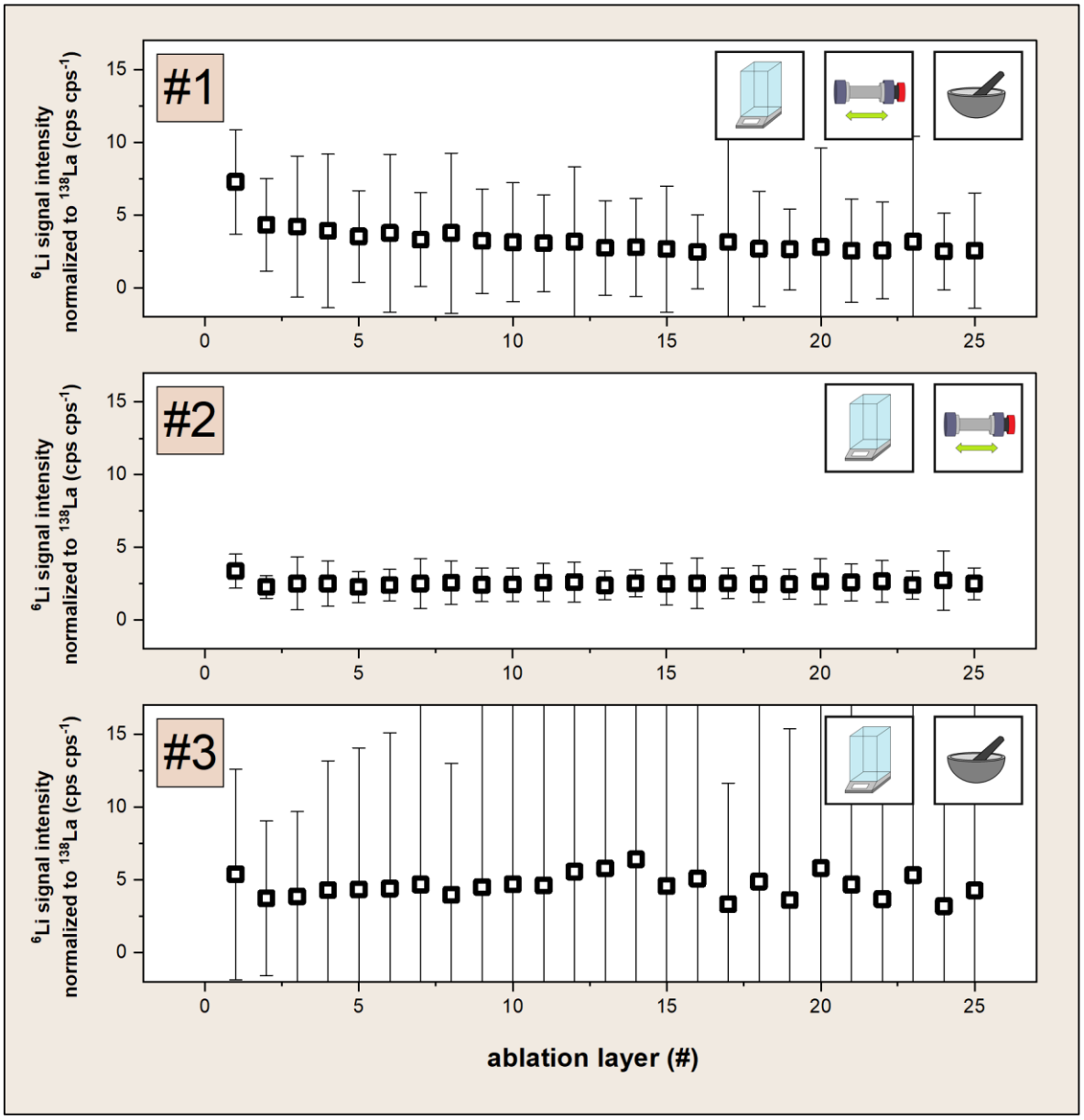


*Figure 4-15: Homogeneity of solid pellets of different standard preparation procedures*

In Figure 4-16, the time-dependent $^{6}$Li signals of one single ablated line of the three differently prepared standards are shown. The first and third standard preparation approach leads to a high signal variation within one line scan. While in the second approach, where the initial

powders were weighted out before milling, the signal variation is significantly lower than in the other approaches. The graphs on the right side in Figure 4-16 are an enlargement of the time-dependent $^{6}Li$ signals for a better comparison between the three signal variations.

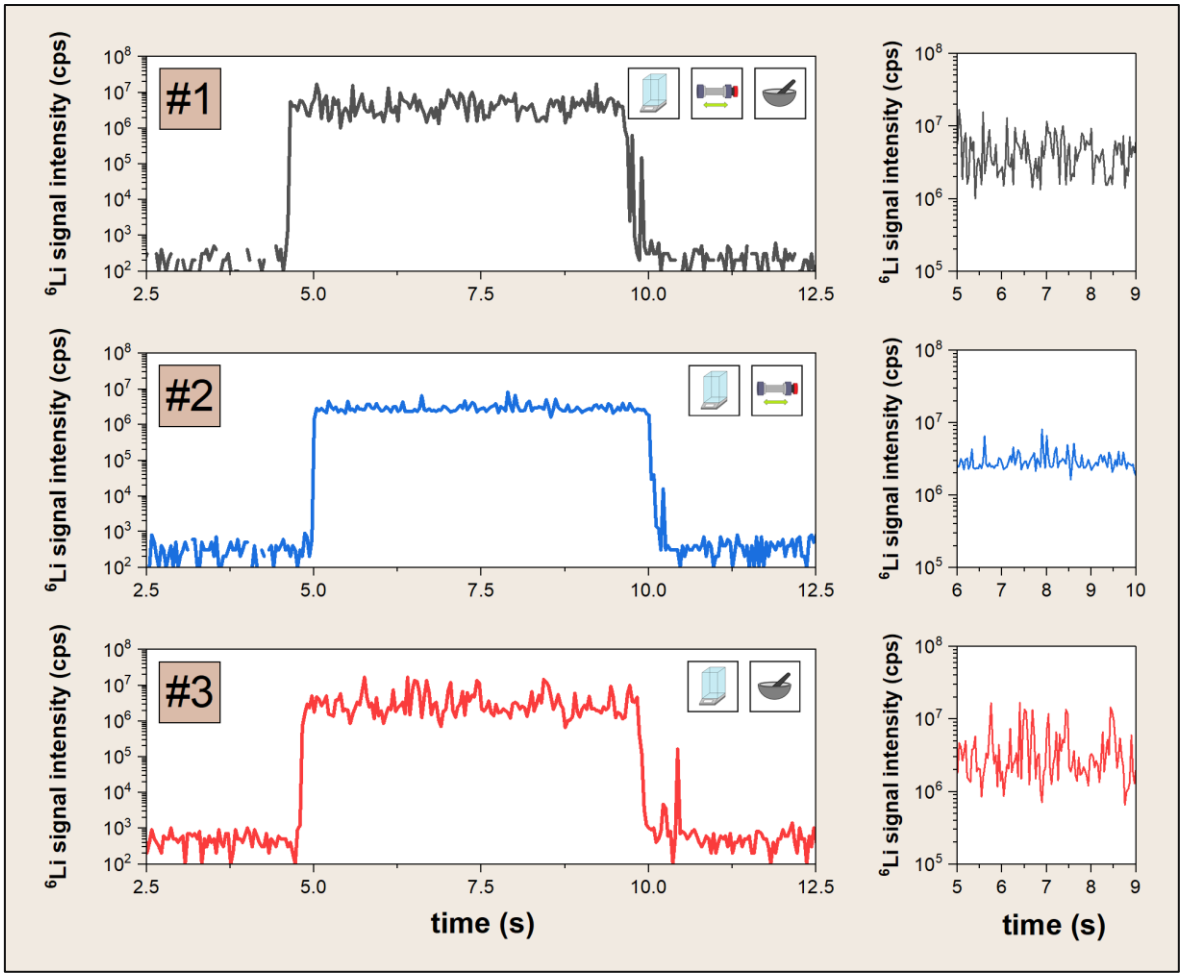


*Figure 4-16: Time-dependent $^{6}Li$ signals of the differently prepared standards. The signal variations in the second approach are significantly lower than in the other two approaches.*

### 4.4.2 Matrix-matched standards made of LLTO powder and $Li_2CO_3$

After finding the optimal strategy for the preparation of matrix-matched standards in the form of pellets, a series of standards between 1 wt.% lithium and 3 wt.% lithium was prepared with the optimized procedure. The results of the lithium signal, the normalized lithium signal as well as the normalized titanium signal can be seen in Figure 4-17. Calibration functions were plotted using the $^{6}Li$ signal and the normalized $^{6}Li$ signal. Additionally, the normalized $^{46}Ti$ signals were investigated.

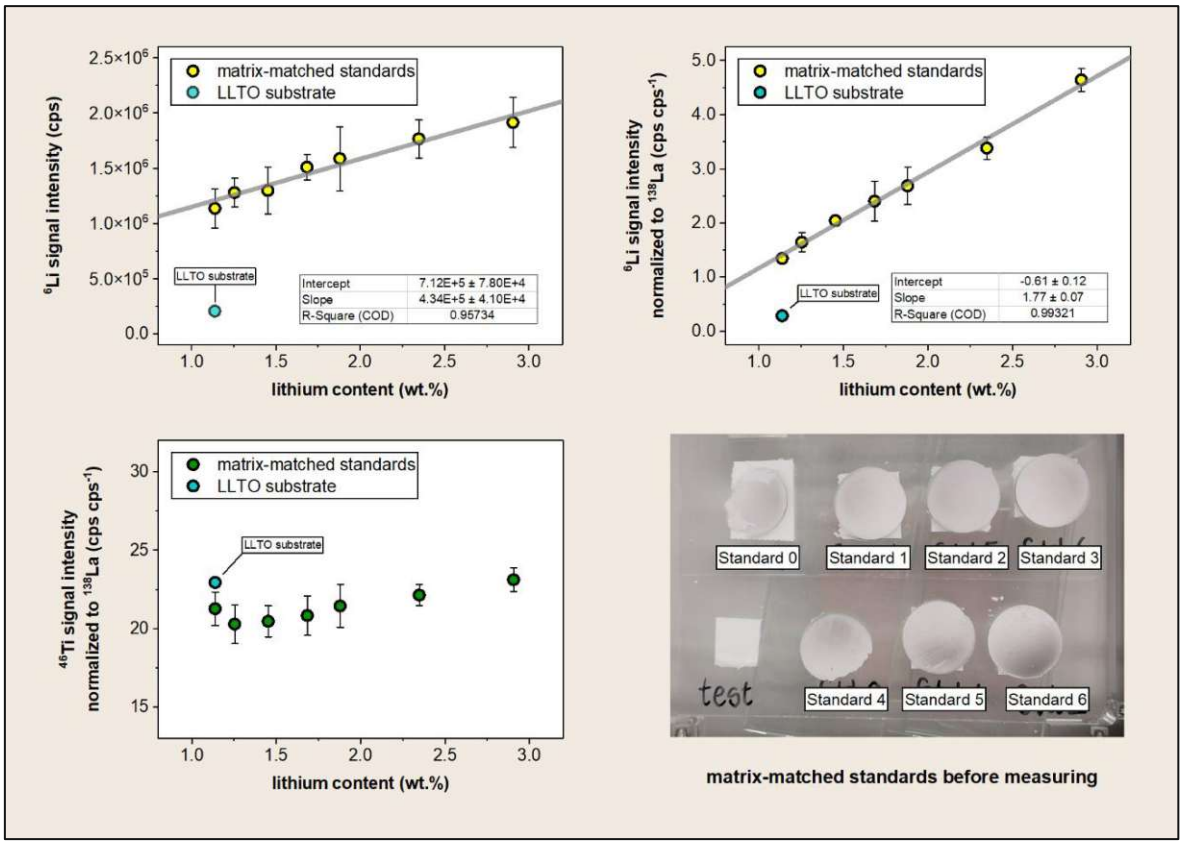


*Figure 4-17: Findings of the measurement of matrix-matched standards out of LLTO powder and $Li_2CO_3$*

Both, the $^6$Li signal as well as the normalized $^6$Li signal exhibit a linear relationship between the lithium concentration and the signal. In both cases the coefficient of determination (COD) is greater than 0.95, for the normalized signal even greater than 0.99. The COD is a number which predicts the quality of fit of a linear regression. A high COD means that in this case the lithium concentration can be accurately predicted based on the lithium signal. The error bars of the lithium signal value correspond to the standard deviation of the measurements. It can be seen from the diagram of the $^6$Li signal intensity depending on the lithium content that the error bars of the different standards overlap. Indeed, when using the normalized $^6$Li signal for quantification, less overlap between the error bars of the data points was obtained.

In the diagram in the bottom left corner of Figure 4-17, the outcome of the Ti/La signal ratio is shown. The ratio between these two elements is approximately constant compared to the lithium signals. This is because of the nature of the produced pellets. For the preparation of the pellets LLTO powder was spiked with lithium carbonate, and when adding $Li_2CO_3$ in different quantities to LLTO, the Ti/La ratio is unaffected, independent of the amount of $Li_2CO_3$.

Besides the matrix-matched standards, an LLTO substrate was also measured to compare the result of the pellet made from pure LLTO powder without lithium carbonate and the result of the LLTO substrate. The outcome of the LLTO substrate is represented as a turquoise data point. An obvious gap between the signal value of the LLTO substrate and the signal value of the pellet out of pure LLTO powder was obtained. One possible explanation for this deviation is that the ablation behaviour is different between a non-sintered pellet and a sintered LLTO substrate. Sintering the standard pellets is a possible solution for this but it leads to further

problems due to the volatility of lithium. This would require the dissolution of the pellet and subsequent reference analysis for accurate quantification. In order to avoid this workload and the other sources of errors, a second quantification approach using different initial powders for pellet preparation was developed. The findings of the second quantification method are described in the next paragraph.

### 4.4.3 Matrix-matched standards made of $Li_2O$, $La_2O_3$, and $TiO_2$

In the second quantification approach, the matrix-matched standards were produced in the same way as in the first approach, but instead of LLTO powder and lithium carbonate, lithium oxide ($Li_2O$), titanium oxide ($Ti_2O$), and lanthanum oxide ($La_2O_3$) were used as initial powders. After the preparation of the pellets, LA-ICP-MS measurements of them were performed, and the resulting calibration functions are shown in Figure 4-18.

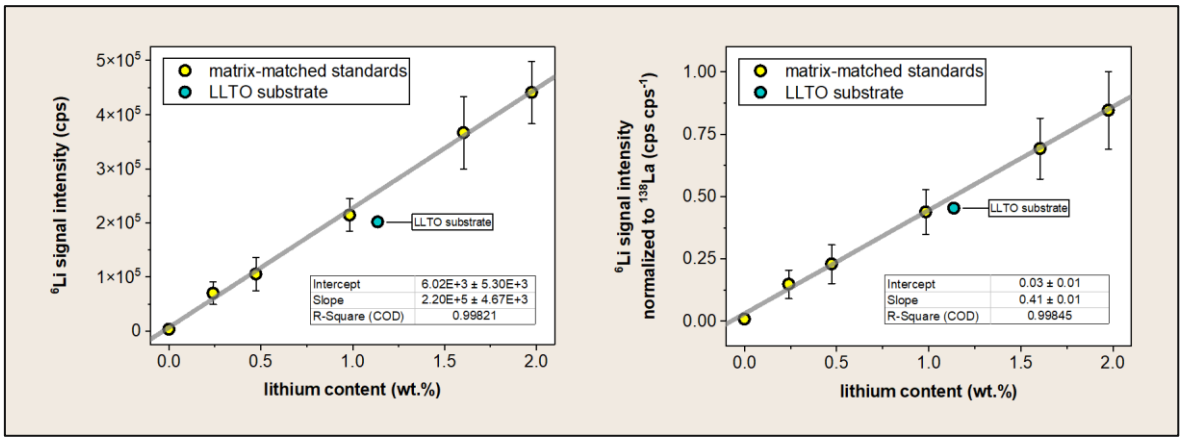


*Figure 4-18: Calibration functions of matrix-matched standards out of oxide powders*

In the left diagram, the lithium signal intensity of all six matrix-matched standards is depicted. The high COD (> 0.998) of this model indicates that the lithium content can be predicted well through the measured $^6$Li signal intensity. This graph also includes the measurement of an LLTO substrate with a lithium content of about 1.14 wt.% as a reference. The reference data point is turquoise and additionally labelled. Here the remaining gap between the reference point and the calibration line is significantly smaller compared to the quantification approach before (Figure 4-17).

The relationship between the normalized lithium signal and the lithium content shows the same trend as the lithium signal. Besides small error bars, also a high COD (> 0.998) was achieved. The reference data point of the LLTO substrate is still closer to the regression line. That indicates that the difference in the ablation behaviour of the pellet and the bulk material is less.

Both quantification approaches show a linear relationship between the lithium signal as well as the normalized lithium signal and the lithium content in the matrix-matched standards. However, in the first approach, the value of the signal of an LLTO substrate does not coincide

with the signal of a standard out of pure LLTO powder due to matrix effects or other processes during ablation. Hence, the first quantification approach using LLTO powder and $Li_2CO_3$ is not applicable to this task. In the second quantification approach, the data point of the measured LLTO substrate is suitable for the calibration line. Therefore, the following quantitative LA-ICP-MS measurements were performed using $Li_2O$, $TiO_2$ and $La_2O_3$ as initial powders for the preparation of matrix-matched standards.

## 4.5 Quantitative LA-ICP-MS measurements of field-stressed LLTO substrates

### 4.5.1 Comparison of vacuum and atmospheric pressure field-stressed LLTO substrates

Quantitative LA-ICP-MS measurements were conducted of LLTO substrates which were field-stressed in atmospheric pressure and in high vacuum ($10^{-5}$ mbar). Before the experiments were performed with the instrument, matrix-matched standards with lithium contents between 0 wt.% and 1.5 wt.% were prepared. The exact concentrations of the pellets can be found in Table 0.13 in the appendix, where in Figure 0-1, also the resulting calibration lines of the $^6Li$ signal and the normalized $^6Li$ signal are depicted.

The resulting quantitative elemental distribution images of the first nine ablated layers of the LLTO substrate, which was polarized with 10 V in a vacuum for 90 minutes at 100 °C, are shown in Figure 4-19. The yellow colouration corresponds to a high lithium content, and the blue colouration means a low lithium amount. The first measured layer (marked with a star) corresponds to the left colour scale (also marked with a star). The second colour scale on the right side corresponds to all further ablated layers.

Through the images of the vacuum field-stressed LLTO substrates in Figure 4-19, the lithium depletion beneath the anode is clearly visible. The intensity of the depletion decreases with an increasing number of ablated layers until hardly any depletion is visible in the $9^{th}$ layer. Additionally, in the first two layers at the position of the cathodic terminal, a higher lithium content is obtained compared to the area between the anode and cathode. The lithium accumulation in surface-near layers might be due to the interaction of the diffused lithium with residual particles ($CO_2$, etc.) in the vacuum and results most likely in the formation of $Li_2CO_3$. Although the LLTO substrate was leached in an ultrasonic bath before preparation, due to the ageing effects, lithium enrichment is evident in layers close to the surface. However, after ablation of the first three to four layers the expected lithium concentration of about 1.14 wt.% is measured.

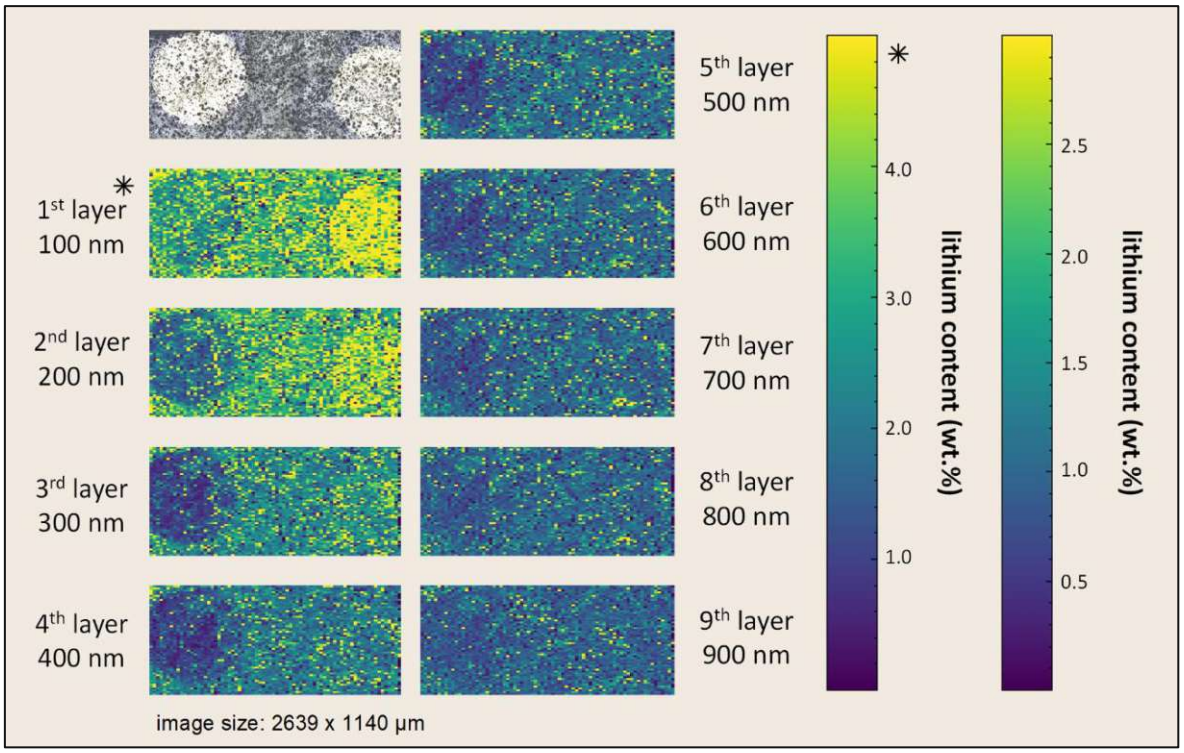


*Figure 4-19: Elemental distribution images of an in a vacuum field-stressed LLTO substrate. In the quantitative images, the lithium content in weight percentage is depicted, whereby a yellow colouration corresponds to a high lithium content, and a dark blue colouration means a low lithium amount. An intensive lithium depletion beneath the anode was observed in the first five layers. In the first two layers, an increased lithium content underneath the cathodic terminal was discovered. Additionally, the lithium accumulation over the whole sample surface in surface-near layers due to ageing effects is visible.*

In Figure 4-20, the elemental maps of an LLTO substrate, which was polarized under atmospheric pressure, are shown. The colour scaling in these images is done in the same way as described in the discussion of the vacuum field-stressed LLTO substrates. However, the scale of the first layer reaches up to 8 wt.% lithium instead of 6 wt.%. There are slight differences between the outcomes of the in a vacuum and the in atmospheric pressure polarized LLTO substrates. An intensive lithium depletion beneath the anode is clearly visible in all layers. In contrast, the depletion zone in the LLTO substrate, which was polarized in a vacuum, shows a smaller expansion into depth. The lithium accumulation at the cathode looks, in both cases, nearly the same. However, looking at the lithium concentration more closely, it becomes clear that the lithium enrichment is significantly higher in the case of the non-evacuated atmosphere. The pre-treatment of the LLTO substrate and the ageing duration were the same in both cases, hence the lithium accumulation over the whole surface in surface-near layers is very similar.

To conclude, the results of the comparison between under vacuum and under atmospheric pressure field-stressed LLTO substrates are illustrated in the form of profiles. Therefore, the created image is cut into sections, and all data points in each rectangular section are averaged. For every layer, a lithium content depending on the lateral sample position, is obtained. The profiles of all 10 investigated layers of LLTO substrates, which were polarized under vacuum and under atmospheric pressure, are shown in Figure 4-21.

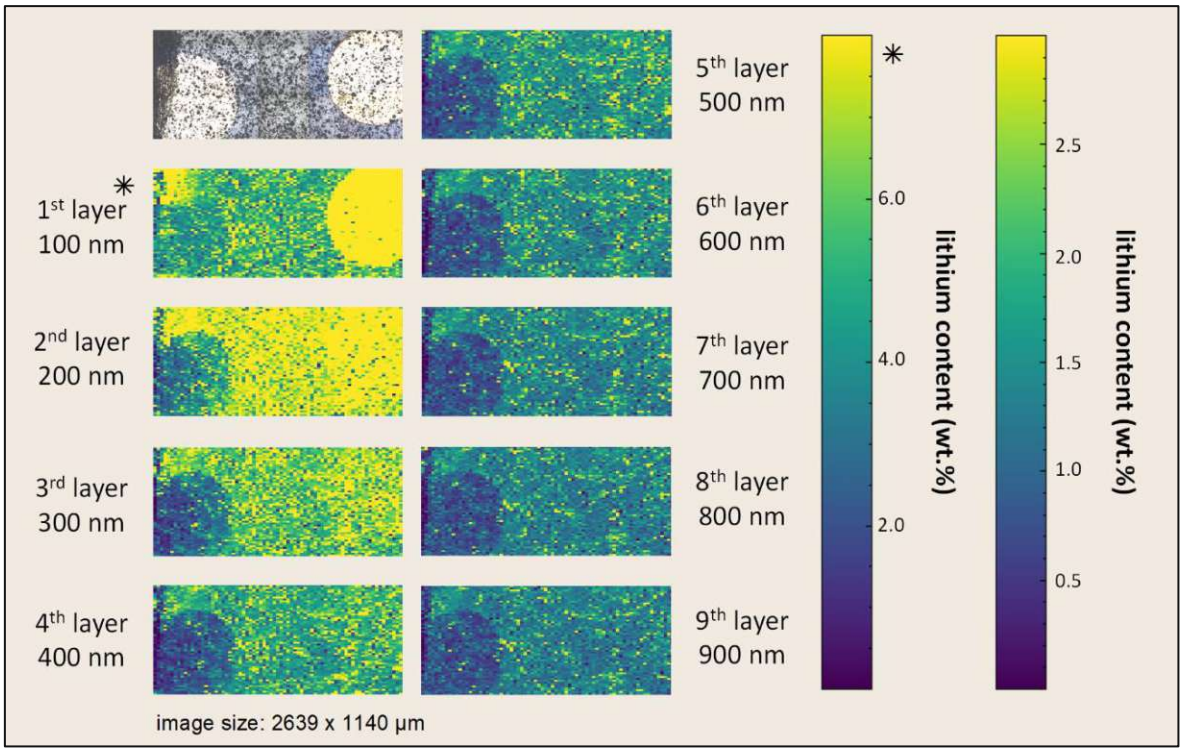


*Figure 4-20: Elemental distribution images of an in atmospheric pressure field-stressed LLTO substrate. A yellow colouration in the image means a high lithium value, and a dark blue colouration has a low lithium content. The first layer is scaled differently, with the star marked scale belonging to the first layer. A really intensive lithium accumulation was observed beneath the cathodic terminal in the first three layers, especially in the first layer (>> 8 wt.%). Below the area of the anode, a lithium depletion was received in all measured layers. Besides the two effects due to polarization, lithium enrichment homogeneous over the whole sample surface in surface-near layers is visible.*

In the upper half of Figure 4-21, the lithium content depending on the lateral sample position of an under vacuum polarized LLTO substrate is depicted. The orange and green areas represent the locations of the sample beneath the anode and the cathode. In the profiles, the three above-described effects are clearly visible: (i) lithium depletion beneath the anode, (ii) lithium accumulation beneath the cathode in the first few layers, and (iii) lithium enrichment over the whole sample surface in surface-near layers. If lithium depletion is defined as the difference between the lithium content below the anode and the lithium content in the intermediate area between the anode and cathode, then it can be seen that the depletion decreases with the increasing layer depth. While in the image of the LLTO substrate polarized under vacuum (Figure 4-19), hardly any depletion is visible in the last layer investigated, one can still clearly see an existing lithium depletion in this type of display.

The outcomes of the under atmospheric pressure polarized LLTO substrates in form of profiles show the same trends as the above discussed images. Compared to the in vacuum field-stressed LLTO substrate a more intense lithium enrichment in surface-near layers was observed, especially the accumulation of lithium in the area of the cathodic terminal is higher. Besides the more intensive lithium accumulation, also the lithium amount in the region of the anode is strongly depleted. In the tenth and last investigated layer, the lithium depletion amounts to a difference of approximately 0.50 wt.%, while in the case of under vacuum polarized LLTO the depletion is only about 0.25 wt.%.

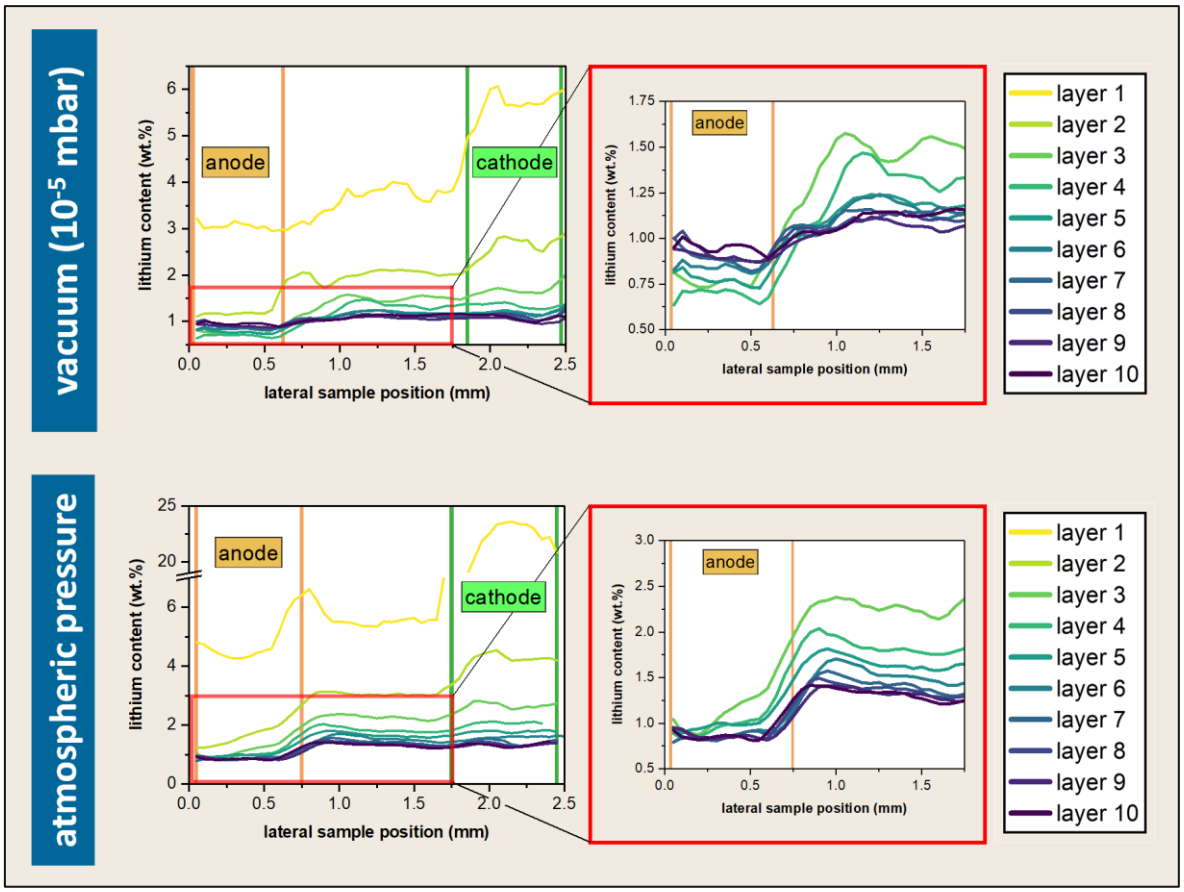


*Figure 4-21: Profiles of LLTO substrates which were polarized in a vacuum and in atmospheric pressure. The first ten ablated layers of the investigated LLTO substrates are depicted. Additionally, an enlargement of the area under the anode is shown in order to see the lithium depletion better.*

Finally, the data points of the three occurring areas (anode, in-between, cathode) in the images (Figure 4-19 and Figure 4-20) were averaged and presented in the form of depth profiles. In depth profiles the lithium content is shown in dependence on the sample depth, which can be seen in Figure 4-22. The green triangles correspond to the area beneath the cathode, the orange squares to the area beneath the anode, and the grey circles represent the zone between the anode and the cathode. In the in a vacuum as well as the under atmospheric pressure polarized LLTO substrate, the general lithium enrichment in the surface-near layers is visible due to the bending of the curves. Additionally, in both cases, a lithium accumulation underneath the cathode is observed. The accumulation in this area can be seen through the effect that the green triangles are at greater lithium contents than the grey circles in the first four to five layers. After these layers were removed, the lithium content in the region of the cathodic terminal was approximately the same as the lithium content in the intermediate area between the anode and cathode. However, the local enrichment under atmospheric pressure is much stronger than the enrichment in a vacuum. The last effect to consider is the depletion below the anode. The substrate, which was polarized in atmospheric pressure indicates a more significant gap between the lithium content in the anode and the region between the anode and cathode, hence the lithium depletion for this sample is higher compared to the lithium depletion in the in a vacuum polarized LLTO substrate. In the atmospheric pressure polarized LLTO substrate a lithium depletion beneath the anode can still be seen at a maximum measured depth of 1 µm.

While the propagation of Li depletion in the vacuum polarized LLTO substrate extends to a depth of 900 nm.

The significant difference between vacuum and atmosphere-polarized samples in terms of amount of transported Li is probably caused by the reaction of Li with atmospheric gases, e.g.

$$2Li^+ + CO_2 + \frac{1}{2}O_2 + 2e^- \rightarrow Li_2CO_3.$$

The formation of $Li_2CO_3$ on the surface would explain the strong Li enrichment, which is most prominent in the first layer. However, also the temperature of the atmospheric polarized sample might have been slightly higher, due to the better thermal contact between sample and heater under atmospheric pressure.

The higher level of Li accumulation/depletion after polarization in air is in line with the much larger charge that was flowing during the coloration experiments. During vacuum polarization the charge was only 0.00164 Coulombs, while 0.0179 Coulombs were measured during the atmospheric polarization. If we assume all this charge corresponds to Li-ion migration, according to equation 3.3, the depletion zone would be 5.3 (in vacuum) and 58 (in air) micrometres deep. Since much shallower depletion zones were observed, the major portion of the current during the field stress is carried by electrons.

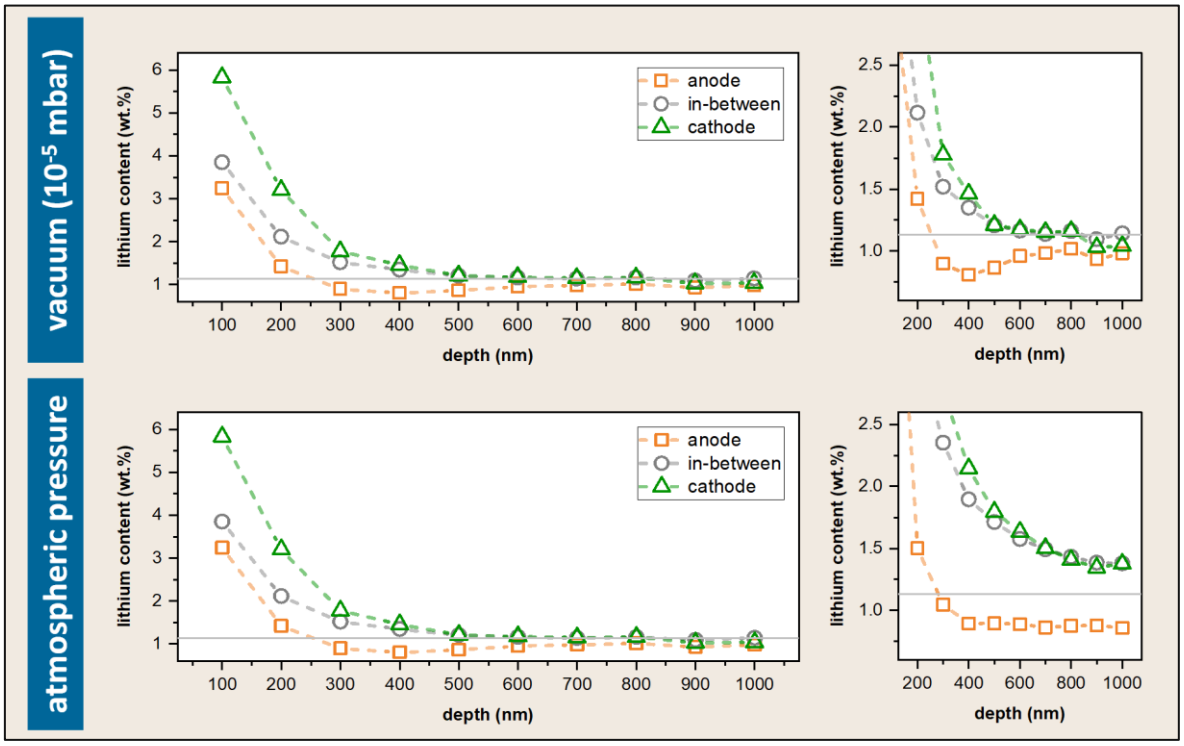


*Figure 4-22: Depth profiles of in a vacuum and under atmospheric pressure field-stressed LLTO substrates*

### 4.5.2 Comparison of field-stressed LLTO substrates with different applied voltages

In this measurement series, different polarization voltages (2.5 V, 4.0 V, 6.0 V, and 8.0 V) were applied to the LLTO substrates. To compare the depth of the lithium depletion zone beneath the anode of differently prepared LLTO sheets, an area with the dimensions of 800 µm x 200 µm underneath the anode was measured. Additionally, the field-stressed LLTO substrate, which was polarized with 2.5 V, was measured entirely so that elemental distribution images could be created.

In Figure 4-23, the findings of these experiments are depicted. The lithium content in dependence on the depth is represented. The samples which were polarized with 4.0 V, 6.0 V, and 8.0 V are shown in this graph, while the LLTO substrate where 2.5 V voltage was applied is shown in greater detail in Figure 4-25. The grey horizontal line corresponds to the nominative lithium amount in a non-polarized LLTO substrate (1.14 wt.% lithium) and serves as a reference. From Figure 4-23, it can be concluded that with higher applied polarization voltages, the lithium depletion zone reaches deeper into the sample. This is observed because more lithium ions migrate from the anode to the cathode during polarization due to a higher current flow. During the polarization experiments, also the total charge during the polarization experiment increased from 0.00082 C at 4 V to 0.004 C at 6 V and 0.023 C at 8 V. The approximate depth of the lithium depletion zone below the anode (Figure 4-24) is 4 µm for 4.0 V, 6 µm for 6.0 V, and higher than 9 µm for 8.0 V. The charge of the depleted Li-ions can be calculated by integrating the Li deficiency under the anode, according to

$$\Delta Q(Li^+) = \frac{F}{M(Li)} \rho_{LLTO} A_{anode} * \int c(Li)_{anode} - c(Li)_{unpol} dz,$$

Where z is the depth, M(Li) is the molar mass of Li (6.941 u) and $\rho_{LLTO}$ is the gravimetric density of LLTO (5 g cm$^{-3}$).

Another interesting observation is that the green and the blue curve in Figure 4-24 show a lithium enrichment in the first layer and hence a decrease in the lithium content in the first few nanometres. At the same time, the red curve does not show this enrichment but an immediate increase in the lithium content. This deviation between the samples could be explained by the different time of production and measurement. All LLTO substrates were leached in water for 60 seconds in an ultrasonic bath before polarizing. However, the 2.5 V sample was measured immediately after polarization, while the other samples were stored and measured at a later time. Reactions that occur during ageing result in a lithium enrichment in surface near layers, as already discussed in chapter *4.3 Removal of the Li accumulation in surface-near layers.*

As mentioned above the depth profile of the LLTO substrate, which was polarized with a voltage of 2.5 V, is described in greater detail in this paragraph. The lithium content in an area beneath the anode in dependency on the depth and the lithium concentrations underneath the cathode and in the area between the anode and cathode are shown in Figure 4-24. When comparing the lithium amount of the anode with the amount of the intermediate area between the anode and cathode, a gap within the first 600 to 700 nm is observed between these two curves. In a depth of 800 nm and deeper, the lithium content in the anode and the intermediate area is similar.

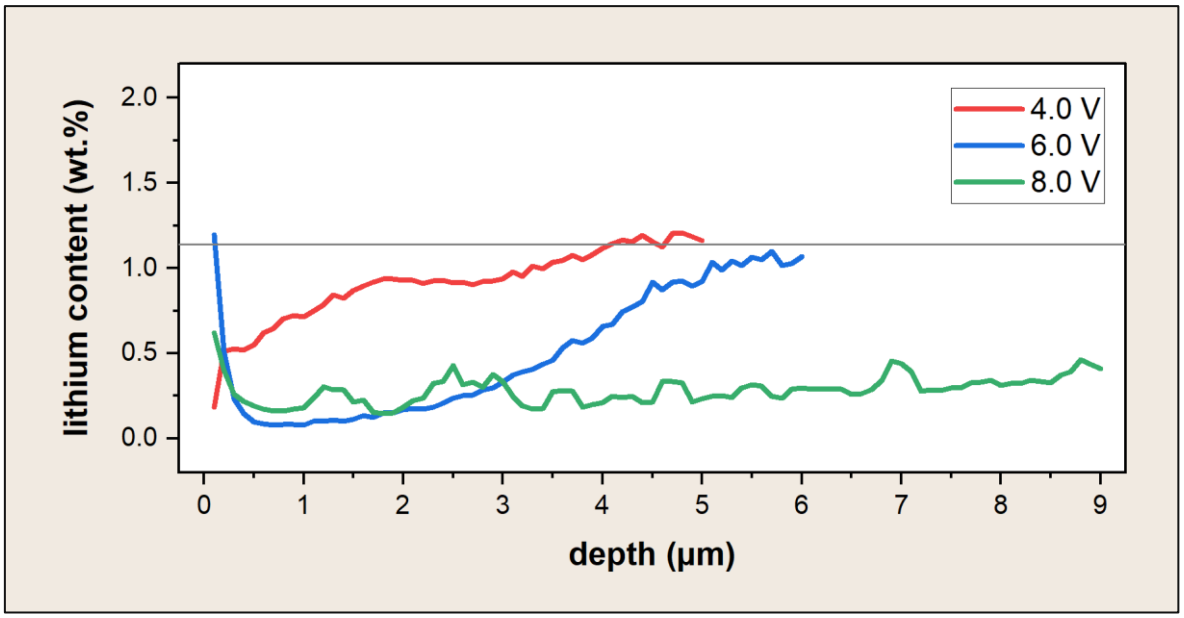


*Figure 4-23: Depth profiles of field-stressed LLTO substrates to which different voltages were applied. The coloured lines represent the measurement results of the different applied voltages, and the grey horizontal line corresponds to the nominal lithium content of non-polarized LLTO (1.14 wt.% lithium). Different depths of lithium depletion of different applied voltages were observed. The higher the applied voltage the deeper the lithium depletion zone underneath the anode.*

Interestingly, no marked Li depletion beneath the anode is observed, but rather an absence of Li enrichment. Probably, 2.5 V are a bit less than the electrochemical stability window of LLTO, and therefore no Li depletion zone is forming. However, the voltage at the anode is sufficient to supress the formation of Li-rich phases at the anode, and therefore prevent the Li enrichment. Visible in Figure 4-24, the lithium concentration increase under the cathode relative to the sample centre is about 0.50 wt.% in the first ablated layer and 0.10 wt.% in the last ablated layer (1 000 nm depth) higher compared to the concentration in the intermediate area. This local accumulation at the area of the cathode was even observed in earlier measurements and is due to the migration of lithium ions to the cathode and probably reaction with components of the ambient air. As already shown in the previous chapter, polarization under atmosphere leads to even more intensive enrichment. In the first 100 nm, a lower lithium content compared to the following 100 nm was gained, which is because of surface remnants of the Pt-electrode. When removing the first layer, a big part of the ablated material was Pt-particles, and therefore, fewer Li-particles were ablated and subsequently detected. The effect of lithium enrichment over the whole sample surface in surface-near layers is also seen in the figure due to the bending of the curves and the decrease of the lithium content in the intermediate area between the anode and cathode.

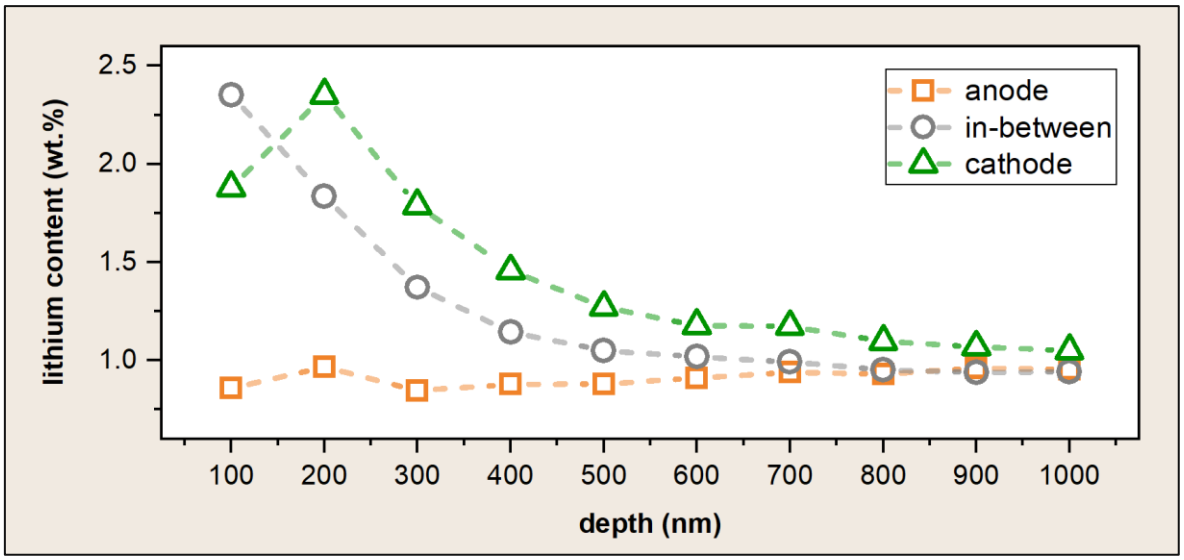


*Figure 4-24: Depth profile of the area of the anode, cathode, and the area between anode and cathode (in-between)*

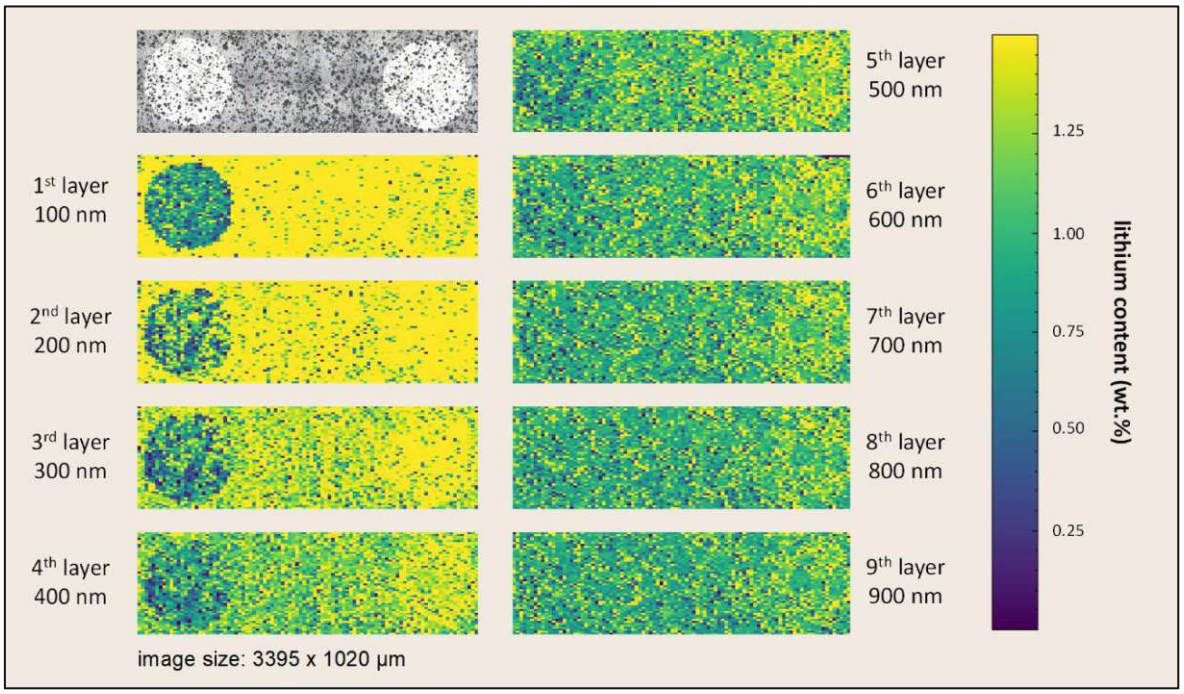


*Figure 4-25: Lithium distribution image of an LLTO substrate where 2.5 V voltage was applied*

The lithium distribution images of the LLTO substrate, which was polarized with a voltage of 2.5 V, are shown in Figure 4-25. The same findings as in the depth profile are observable in the images. The lithium depletion zone beneath the anode is visible in the first six to seven layers. Afterwards, the lithium content of the area below the anode and in the intermediate area seems to be equal. A slight local lithium accumulation underneath the area of the cathode was observed in all nine investigated layers. Finally, the homogenous lithium enrichment over the whole surface in the first few surface-near layers is also received.

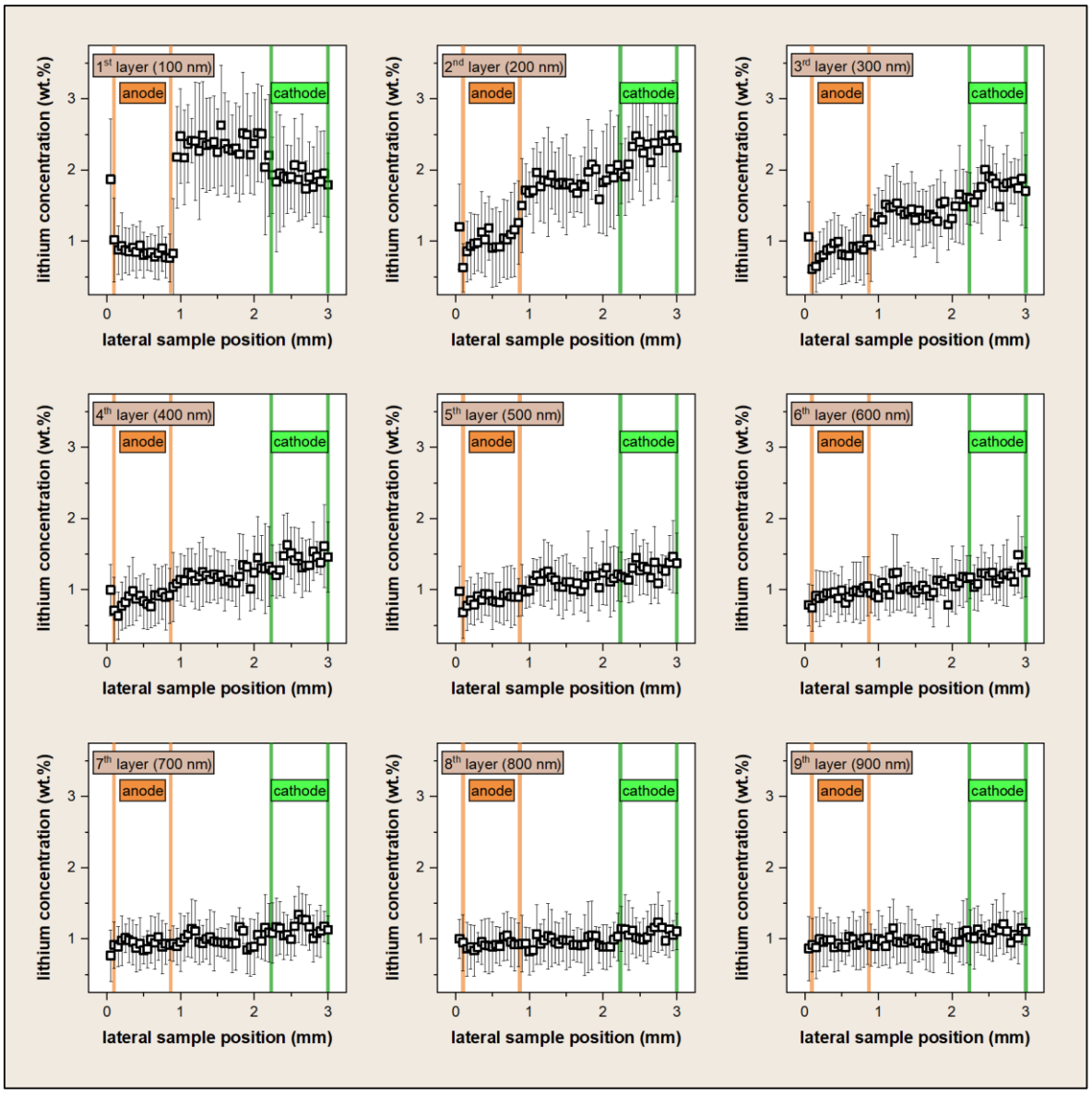


*Figure 4-26: Profiles of a field-stressed LLTO substrate where a voltage of 2.5 V was applied. The findings of the first nine ablated layers are shown. The orange area belongs to the anode, and the green to the cathode. In the surface-near layers, the lithium depletion beneath the anode is clearly obtained, while from the 7th to 8th layer, no lithium depletion is visible.*

The profiles of nine ablated layers of the before discussed LLTO substrate can be seen in Figure 4-26. In the first layer, the lithium depletion under the anodic terminal is clearly visible from the graph. The lithium amount beneath the cathode is inferior to the amount in the area between the anode and cathode due to the additional ablation of the Au-electrode. With increasing depth (layer number), the lithium depletion underneath the anode decreases until finally, there is no more difference in the lithium content between the anode and the intermediate area between the anode and cathode. In the first few layers, the most intensive lithium depletion was observed. As can be seen from the following figure, the lithium content difference between the area under the anode and the intermediate area in the first layer comes to approximately 1.50 wt.%. While from the 7th layer onwards, a difference in the lithium concentration is hardly visible.

### 4.5.3 Electrochemical conclusions regarding stability window and degradation mechanisms

Overall, we found Li enrichment at the surface of LLTO after ageing in air, which was strongly enhanced under the cathode of the polarized samples. Due to the strong surface confinement of the Li enrichment at the surface, it is very likely that it stems from reaction products with the ambient atmosphere. The Gibbs energy of these reactions can be calculated from data that is available online (https://webbook.nist.gov/chemistry/), and the corresponding equilibrium voltage of a Li/atmosphere cell can be calculated by $U_{eq} = \Delta_R G/zF$.

Potential reactions of Li-ions are:

Formation of lithium peroxide ($U_{eq}$ = 2.9 V):

$$2Li^+ + O_2 + 2e^- \rightarrow Li_2O_2.$$

Formation of lithium hydroxide ($U_{eq}$ = 3.7 V)

$$2Li^+ + H_2O + \frac{1}{2}O_2 + 2e^- \rightarrow 2LiOH.$$

Formation of lithium carbonate ($U_{eq}$ = 3.9 V)

$$2Li^+ + CO_2 + \frac{1}{2}O_2 + 2e^- \rightarrow Li_2CO_3.$$

From these reactions, the formation of lithium carbonate has the highest driving force.

On the free LLTO surface, electronic charge carriers may be the reduction of a transition metal (e.g. $Fe^{3+} \rightarrow Fe^{2+}$). During polarization, the chemical potential of electrons at the cathode is increased, thereby accelerating the formation of Li-rich phases at the surface. Interestingly, the cathodic Li-enrichment occurs even in under high vacuum, most likely due to the residual molecules that are present at $10^{-5}$ mbar.

The Li depletion under the anode occurs when the applied voltage exceeds the electrochemical stability window, and decomposition reactions deplete the electrolyte of lithium. These reactions were so far only calculated by density functional theory (DFT) calculations, and predict an electrochemical stability window of 1.7-3.7 V vs. Li metal [39]– i.e. a width of 2 V. According to these calculations, Li-rich phases will form at the cathode, and Li-depleted phases at the anode, when the applied voltage exceeds 2 V.

Our measurements have, however, shown that no pronounced Li depletion, but rather a mere absence of accumulation, is observed after polarization with 2.5 V, indicating that the electrochemically usable stability window of LLTO is in the range of 2.5 V. When the applied voltage significantly exceeds 2.5 V, Li depletion beneath the anode can be observed. Noteworthy, the extent of this depletion increases strongly nonlinearly with voltage, as seen in Figure 4-23, and exhibits a pronounced thermal activation. Consequently, the decomposition kinetics at room temperature are likely much more sluggish than at 150 °C. Moreover, the comparison of the amounts of depleted/accumulated Li-ions and electrical charge showed that also.

In summary, our measurements suggest that the electrochemical stability window of LLTO towards high voltage cathodes is higher than expected from ab-initio calculations. These findings are in line with the observed beneficial effect of LLTO coating on high voltage cathode materials in liquid-based Li-ion batteries [53], which enabled good cycling performance up to 4.4 V.

# 5 Conclusion and Outlook

The aim of this master thesis was to examine stoichiometric inhomogeneities in field-stressed LLTO electrolytes. An appropriate method for the investigation of material composition changes caused by polarization of LLTO is laser ablation inductively coupled plasma mass spectrometry (LA-ICP-MS). The excimer laser based LA-ICP-MS device is capable of mapping such stoichiometric inhomogeneities as it provides the required lateral as well as depth resolution, which makes it a powerful tool for a better understanding of the mechanisms of decomposition kinetics and the exact voltage limitations, which are yet unknown.

A suitable measurement and quantification method was developed using LA-ICP-MS with a lateral resolution of 20 µm and a depth resolution of approximately 100 nm was developed. In summary, the following results were obtained: During the qualitative analysis of LLTO substrates two different effects were observed. Firstly, a spatially confined lithium depletion zone underneath the anode at voltages of 8.0-10.0 V was obtained. Next, a general lithium enrichment in surface-near layers of native LLTO, as well as field-stressed LLTO, was detected. This enrichment complicates the measurement of the lithium depletion zone beneath the anode in surface-near layers due to strong fluctuations in signal intensity. A procedure for effective removal of surplus Li from the sample surface has been developed.

After qualitative LA-ICP-MS analysis, a quantification approach for a better examination of these observations was developed by preparing matrix-matched standards out of lithium oxide ($Li_2O$), titanium oxide ($TiO_2$), and lanthanum oxide ($La_2O_3$). A linear behaviour of the signal intensity depending on the lithium concentration in the concentration range 0.0 – 1.5 wt.% Li was obtained, enabling assessment of even minor changes in the Li content of LLTO samples.

In quantitative LA-ICP-MS analysis, the effects of polarization in a vacuum and under atmospheric pressure and of the application of different voltages were investigated. The findings of the polarization under atmospheric pressure indicate a more substantial lithium accumulation in the first few layers at the area of the cathode, and a deeper depletion layer below the anode, compared to polarization under reduced pressure. In the experiments of applying different voltages, the dependency of the depth of the lithium depletion on the applied voltage was examined.

It was observed that the decomposition of a field-stressed LLTO electrolytes manifests itself through a lithium depletion zone underneath the anode. Pronounced Li depletion is observable after polarization at 4 V, and this depletion strongly increases with higher applied potentials. When the potential is reduced to 2.5 V, and the time is increased to 18 h at elevated temperatures (150 °C), neither the typical surface-near lithium accumulation, nor a pronounced depletion can be observed below the anode. This finding suggests that the stability window width is about 2.5 V. However, also the decomposition kinetics may be too sluggish at lower potentials. A complete answer to the question of the exact voltage stability limit cannot be given if only the analytical measurements carried out are considered.

At this point, further investigations are required to exactly determine the stability limit. However, this work has already developed the method to perform this determination. Besides the application of the developed method to a wide range of polarized samples, in-situ

measurements of field-stressed LLTO electrolytes can lead to promising results in the future. Furthermore, the storage of the matrix-matched standards can be improved, so that they can be used more often and had not been prepared for every measurement. Storage in other atmospheres than the ambient atmosphere can be a possible solution and can lead to a higher stability.

# Appendix

*Table 0.1: Laser ablation (LA) and inductively coupled plasma mass spectrometry (ICP-MS) operating parameters during the optimization of the laser fluence*

| Laser ablation | | Inductively coupled plasma mass spectrometry | |
|---|---|---|---|
| Laser fluence | 0.25 – 2.5 J $cm^{-2}$ | RF power | 1 550 W |
| Beam size | 20 µm | Auxiliary gas flow | 0.80 mL $min^{-1}$ |
| Repetition rate | 200 Hz | Cool gas flow | 13.85 mL $min^{-1}$ |
| Overlap | 0 µm | Nebulizer gas flow | 0.95 L $min^{-1}$ |
| Scan speed | 600 µm $s^{-1}$ | Dwell time per mass | 10 ms |
| He flow | 800 mL $min^{-1}$ | Measured Isotopes | $^{6}Li$, $^{46}Ti$, $^{138}La$ |

*Table 0.2: LA and ICP-MS operating parameters during the optimization of the helium flow*

| Laser ablation | | Inductively coupled plasma mass spectrometry | |
|---|---|---|---|
| Laser fluence | 1.5 J $cm^{-2}$ | RF power | 1 550 W |
| Beam size | 20 µm | Auxiliary gas flow | 0.80 mL $min^{-1}$ |
| Repetition rate | 200 Hz | Cool gas flow | 13.85 mL $min^{-1}$ |
| Overlap | 0 µm | Nebulizer gas flow | 0.95 L $min^{-1}$ |
| Scan speed | 600 µm $s^{-1}$ | Dwell time per mass | 10 ms |
| He flow | 300 - 900 mL $min^{-1}$ | Measured Isotopes | $^{6}Li$, $^{46}Ti$, $^{138}La$ |

*Table 0.3: LA and ICP-MS operating parameters during the optimization of the overlap*

| Laser ablation | | Inductively coupled plasma mass spectrometry | |
|---|---|---|---|
| Laser fluence | 1.5 J $cm^{-2}$ | RF power | 1 550 W |
| Beam size | 10, 20 µm | Auxiliary gas flow | 0.80 mL $min^{-1}$ |
| Repetition rate | 100, 200 Hz | Cool gas flow | 13.80 mL $min^{-1}$ |
| Overlap | 0, 10, 17 µm | Nebulizer gas flow | 0.78 L $min^{-1}$ |
| Scan speed | 0.6, 1.0, 2.0 mm $s^{-1}$ | Dwell time per mass | 10 ms |
| He flow | 800 mL $min^{-1}$ | Measured Isotopes | $^{6}Li$, $^{46}Ti$, $^{138}La$ |

*Table 0.4: LA and ICP-MS operating parameters during single spot measurement of pre-ablation*

| Laser ablation | | Inductively coupled plasma mass spectrometry | |
|---|---|---|---|
| Laser fluence | 1.5 J $cm^{-2}$ | RF power | 1 550 W |
| Beam size | 10, 20 µm | Auxiliary gas flow | 0.80 mL $min^{-1}$ |
| Repetition rate | 100, 200 Hz | Cool gas flow | 13.85 mL $min^{-1}$ |
| Overlap | 0, 10, 17 µm | Nebulizer gas flow | 0.88 L $min^{-1}$ |
| Scan speed | 0.6, 1.0, 2.0 mm $s^{-1}$ | Dwell time per mass | 10 ms |
| He flow | 800 mL $min^{-1}$ | Measured Isotopes | $^{6}Li$, $^{46}Ti$, $^{138}La$ |

*Table 0.5: LA and ICP-MS operating parameters during imaging of pre-ablation*

| Laser ablation | | Inductively coupled plasma mass spectrometry | |
|---|---|---|---|
| Laser fluence | 1.5 J $cm^{-2}$ | RF power | 1 550 W |
| Beam size | 10, 20 µm | Auxiliary gas flow | 0.80 mL $min^{-1}$ |
| Repetition rate | 100, 200 Hz | Cool gas flow | 13.85 mL $min^{-1}$ |
| Overlap | 0, 10, 17 µm | Nebulizer gas flow | 0.95 L $min^{-1}$ |
| Scan speed | 0.6, 1.0, 2.0 mm $s^{-1}$ | Dwell time per mass | 10 ms |
| He flow | 800 mL $min^{-1}$ | Measured Isotopes | $^{6}Li$, $^{46}Ti$, $^{138}La$ |

*Table 0.6: LA and ICP-MS operating parameters during imaging of the leaching approach*

| Laser ablation | | Inductively coupled plasma mass spectrometry | |
|---|---|---|---|
| Laser fluence | 1.5 J $cm^{-2}$ | RF power | 1 550 W |
| Beam size | 10, 20 µm | Auxiliary gas flow | 0.80 mL $min^{-1}$ |
| Repetition rate | 100, 200 Hz | Cool gas flow | 13.85 mL $min^{-1}$ |
| Overlap | 0, 10, 17 µm | Nebulizer gas flow | 0.95 L $min^{-1}$ |
| Scan speed | 0.6, 1.0, 2.0 mm $s^{-1}$ | Dwell time per mass | 10 ms |
| He flow | 800 mL $min^{-1}$ | Measured Isotopes | $^{6}Li$, $^{46}Ti$, $^{138}La$ |

*Table 0.7: LA and ICP-MS operating parameters during the removal of the Li accumulation - summary*

| Laser ablation | | Inductively coupled plasma mass spectrometry | |
|---|---|---|---|
| Laser fluence | 1.5 J $cm^{-2}$ | RF power | 1 550 W |
| Beam size | 10, 20 µm | Auxiliary gas flow | 0.80 mL $min^{-1}$ |
| Repetition rate | 100, 200 Hz | Cool gas flow | 13.80 mL $min^{-1}$ |
| Overlap | 0, 10, 17 µm | Nebulizer gas flow | 1.0 L $min^{-1}$ |
| Scan speed | 0.6, 1.0, 2.0 mm $s^{-1}$ | Dwell time per mass | 10 ms |
| He flow | 800 mL $min^{-1}$ | Measured Isotopes | $^{6}Li$, $^{46}Ti$, $^{138}La$ |

*Table 0.8: LA and ICP-MS operating parameters during optimization of standard preparation*

| Laser ablation | | Inductively coupled plasma mass spectrometry | |
|---|---|---|---|
| Laser fluence | 1.5 J $cm^{-2}$ | RF power | 1 550 W |
| Beam size | 10, 20 µm | Auxiliary gas flow | 0.80 mL $min^{-1}$ |
| Repetition rate | 100, 200 Hz | Cool gas flow | 13.85 mL $min^{-1}$ |
| Overlap | 0, 10, 17 µm | Nebulizer gas flow | 0.90 L $min^{-1}$ |
| Scan speed | 0.6, 1.0, 2.0 mm $s^{-1}$ | Dwell time per mass | 10 ms |
| He flow | 800 mL $min^{-1}$ | Measured Isotopes | $^{6}Li$, $^{46}Ti$, $^{138}La$ |

*Table 0.9: Operating parameters of LA and ICP-MS during the evaluation of quantitative approach I*

| Laser ablation | | Inductively coupled plasma mass spectrometry | |
|---|---|---|---|
| Laser fluence | 1.50 J $cm^{-2}$ | RF power | 1 550 W |
| Beam size | 20 µm | Auxiliary gas flow | 0.80 mL $min^{-1}$ |
| Repetition rate | 200 Hz | Cool gas flow | 14.0 mL $min^{-1}$ |
| Overlap | 17 µm | Nebulizer gas flow | 0.97 L $min^{-1}$ |
| Scan speed | 600 µm $s^{-1}$ | Dwell time per mass | 10 ms |
| He flow | 800 mL $min^{-1}$ | Measured Isotopes | $^{6}Li$, $^{46}Ti$, $^{138}La$ |

*Table 0.10: Operating parameters of LA and ICP-MS during the evaluation of quantitative approach II*

| Laser ablation | | Inductively coupled plasma mass spectrometry | |
|---|---|---|---|
| Laser fluence | 1.50 J $cm^{-2}$ | RF power | 1 550 W |
| Beam size | 20 µm | Auxiliary gas flow | 0.80 mL $min^{-1}$ |
| Repetition rate | 200 Hz | Cool gas flow | 13.85 mL $min^{-1}$ |
| Overlap | 17 µm | Nebulizer gas flow | 0.95 L $min^{-1}$ |
| Scan speed | 600 µm $s^{-1}$ | Dwell time per mass | 10 ms |
| He flow | 800 mL $min^{-1}$ | Measured Isotopes | $^{6}Li$, $^{46}Ti$, $^{138}La$ |

*Table 0.11: Outcomes of the measurement of the matrix-matched standards (approach I)*

| Standard (#) | Lithium content (wt.%) | $^{6}$Li signal intensity (cps) | Standard deviation (cps) | $^{6}$Li signal norm. to $^{138}$La (cps cps$^{-1}$) | Standard deviation (cps cps$^{-1}$) |
|---|---|---|---|---|---|
| 0 | 1.14 | 1.13*10$^{6}$ | 1.76*10$^{5}$ | 1.35 | 0.10 |
| 1 | 1.25 | 1.28*10$^{6}$ | 1.32*10$^{5}$ | 1.65 | 0.18 |
| 2 | 1.45 | 1.30*10$^{6}$ | 2.12*10$^{5}$ | 2.04 | 0.09 |
| 3 | 1.68 | 1.51*10$^{6}$ | 1.17*10$^{5}$ | 2.40 | 0.37 |
| 4 | 1.88 | 1.59*10$^{6}$ | 2.92*10$^{5}$ | 2.68 | 0.35 |
| 5 | 2.35 | 1.77*10$^{6}$ | 1.73*10$^{5}$ | 3.38 | 0.20 |
| 6 | 2.91 | 1.91*10$^{6}$ | 2.25*10$^{5}$ | 4.64 | 0.22 |

*Table 0.12: Outcomes of the measurements of the matrix-matched standards (approach II)*

| Standard (#) | Lithium content (wt.%) | $^{6}$Li signal intensity (cps) | Standard deviation (cps) | $^{6}$Li signal norm. to $^{138}$La (cps cps$^{-1}$) | Standard deviation (cps cps$^{-1}$) |
|---|---|---|---|---|---|
| 0 | 0.00 | 3.47*10$^{3}$ | 1.93*10$^{3}$ | 0.01 | 0.01 |
| 1 | 0.26 | 7.00*10$^{4}$ | 2.10*10$^{4}$ | 0.15 | 0.06 |
| 2 | 0.47 | 1.05*10$^{5}$ | 3.07*10$^{4}$ | 0.23 | 0.08 |
| 3 | 0.98 | 2.14*10$^{5}$ | 2.98*10$^{4}$ | 0.44 | 0.09 |
| 4 | 1.61 | 3.66*10$^{5}$ | 6.73*10$^{4}$ | 0.69 | 0.12 |
| 5 | 1.97 | 4.40*10$^{5}$ | 5.74*10$^{4}$ | 0.85 | 0.16 |

*Table 0.13: Matrix-matched standards for quantification of polarized LLTO substrates (comparison I)*

| Standard (#) | Lithium content (wt.%) | $^{6}$Li signal intensity (cps) | Standard deviation (cps) | $^{6}$Li signal norm. to $^{138}$La (cps cps$^{-1}$) | Standard deviation (cps cps$^{-1}$) |
|---|---|---|---|---|---|
| 0 | 0.00 | 7.05*10$^{1}$ | 1.94*10$^{1}$ | 0.00 | 0.00 |
| 1 | 0.24 | 9.85*10$^{4}$ | 9.27*10$^{3}$ | 0.04 | 0.01 |
| 2 | 0.56 | 1.98*10$^{5}$ | 8.66*10$^{3}$ | 0.08 | 0.01 |
| 3 | 0.73 | 2.60*10$^{5}$ | 1.66*10$^{4}$ | 0.13 | 0.01 |
| 4 | 0.95 | 3.41*10$^{5}$ | 5.16*10$^{4}$ | 0.17 | 0.02 |
| 5 | 1.27 | 4.88*10$^{5}$ | 5.57*10$^{4}$ | 0.25 | 0.02 |
| 6 | 1.49 | 5.90*10$^{5}$ | 5.70*10$^{4}$ | 0.32 | 0.03 |

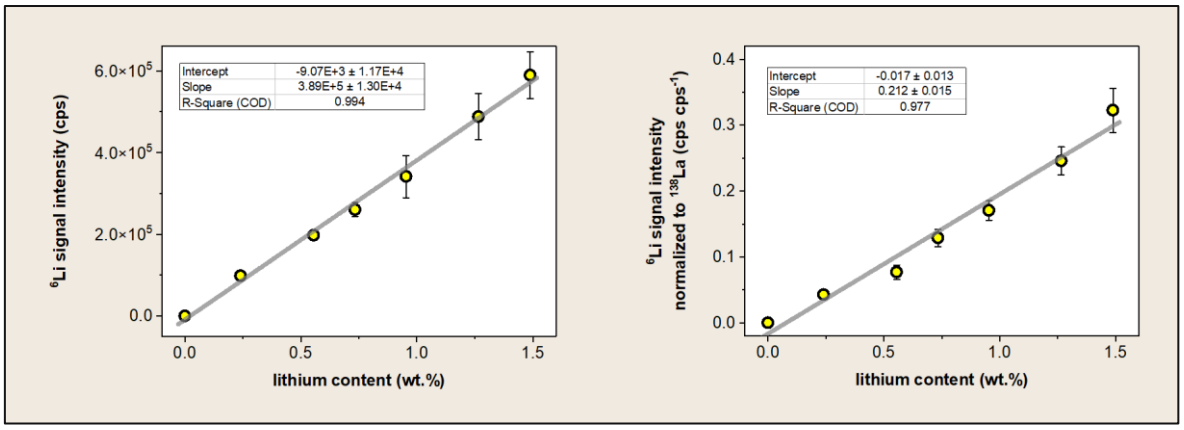


*Figure 0-1: Calibration lines of the quantitative LA-ICP-MS measurement of polarized LLTO substrates (comparison I)*

*Table 0.14: Matrix-matched standards for quantification of polarized LLTO substrates (comparison II)*

| Standard (#) | Lithium content (wt.%) | $^{6}$Li signal intensity (cps) | Standard deviation (cps) | $^{6}$Li signal norm. to $^{138}$La (cps cps$^{-1}$) | Standard deviation (cps cps$^{-1}$) |
|---|---|---|---|---|---|
| 0 | 0.00 | 5.34*10$^{1}$ | 1.22*10$^{1}$ | 0.00 | 0.00 |
| 1 | 0.25 | 9.62*10$^{4}$ | 8.81*10$^{3}$ | 0.08 | 0.02 |
| 2 | 0.50 | 1.97*10$^{5}$ | 1.88*10$^{4}$ | 0.18 | 0.04 |
| 3 | 0.77 | 3.22*10$^{5}$ | 3.15*10$^{4}$ | 0.24 | 0.04 |
| 4 | 1.02 | 4.19*10$^{5}$ | 1.94*10$^{4}$ | 0.37 | 0.05 |
| 5 | 1.31 | 4.79*10$^{5}$ | 2.77*10$^{4}$ | 0.43 | 0.04 |
| 6 | 1.53 | 5.77*10$^{5}$ | 3.70*10$^{4}$ | 0.55 | 0.07 |

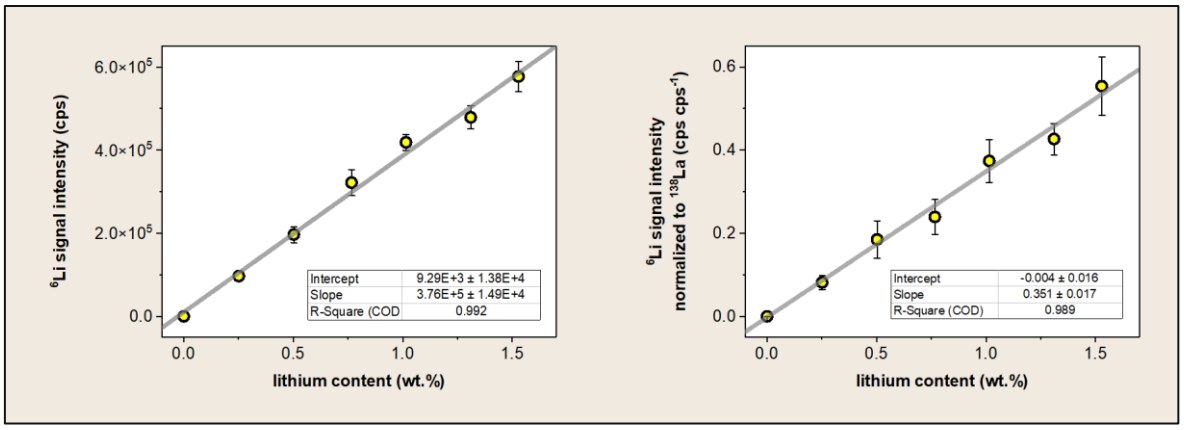


*Figure 0-2: Calibration lines of the quantitative LA-ICP-MS measurement of polarized LLTO substrates (comparison II)*

# List of figures

## List of tables

# References


1. Lu, J. and Y. Li, *Perovskite-type Li-ion solid electrolytes: a review.* Journal of Materials Science: Materials in Electronics, 2021. **32**(8): p. 9736-9754.

2. Danish, Z., *wang Investigation of the ecological footprint's driving factors: what we learn from the experience of emerging economies Sustain.* Cities Soc, 2019. **49**.

3. Waheed, R., S. Sarwar, and C. Wei, *The survey of economic growth, energy consumption and carbon emission. Energy Rep 5: 1103–1115*. 2019.

4. Lin, B. and Z. Jia, *The energy, environmental and economic impacts of carbon tax rate and taxation industry: A CGE based study in China.* Energy, 2018. **159**: p. 558-568.

5. Goodenough, J.B. and Y. Kim, *Challenges for Rechargeable Li Batteries.* Chemistry of Materials, 2010. **22**(3): p. 587-603.

6. Knauth, P., *Inorganic solid Li ion conductors: An overview.* Solid State Ionics, 2009. **180**(14): p. 911-916.

7. Bruce, P. and A. West, *Ionic conductivity of LISICON solid solutions, Li2+ 2xZn1− xGeO4.* Journal of Solid State Chemistry, 1982. **44**(3): p. 354-365.

8. Murugan, R., V. Thangadurai, and W. Weppner, *Fast lithium ion conduction in garnet-type Li7La3Zr2O12.* Angewandte Chemie International Edition, 2007. **46**(41): p. 7778-7781.

9. Inaguma, Y., et al., *Candidate compounds with perovskite structure for high lithium ionic conductivity.* Solid State Ionics, 1994. **70**: p. 196-202.

10. Inaguma, Y., et al., *High ionic conductivity in lithium lanthanum titanate.* Solid State Communications, 1993. **86**(10): p. 689-693.

11. Bachman, J.C., et al., *Inorganic solid-state electrolytes for lithium batteries: mechanisms and properties governing ion conduction.* Chemical reviews, 2016. **116**(1): p. 140-162.

12. Belous, A., et al., *The crystal-chemical and electrophysical characteristics of the complex oxides Ln2/3-xM3xTiO3.* Russian J. Inorg. Chem, 1987. **32**: p. 156-157.

13. Cao, C., et al., *Recent advances in inorganic solid electrolytes for lithium batteries.* Frontiers in energy research, 2014. **2**: p. 25.

14. Bohnke, O., *The fast lithium-ion conducting oxides Li3xLa2/3−xTiO3 from fundamentals to application.* Solid State Ionics, 2008. **179**(1): p. 9-15.

15. Chen, C. and K. Amine, *Ionic conductivity, lithium insertion and extraction of lanthanum lithium titanate.* Solid State Ionics, 2001. **144**(1-2): p. 51-57.

16. Chen, C.H. and K. Amine, *Ionic conductivity, lithium insertion and extraction of lanthanum lithium titanate.* Solid State Ionics, 2001. **144**(1): p. 51-57.

17. Kharton, V., F. Marques, and A. Atkinson, *Transport properties of solid oxide electrolyte ceramics: a brief review.* Solid State Ionics, 2004. **174**(1-4): p. 135-149.

18. Takada, K., *Progress and prospective of solid-state lithium batteries.* Acta Materialia, 2013. **61**(3): p. 759-770.

19. Wu, J.-F. and X. Guo, *Origin of the low grain boundary conductivity in lithium ion conducting perovskites: Li3xLa0.67–xTiO3.* Physical Chemistry Chemical Physics, 2017. **19**(8): p. 5880-5887.

20. Zinkevich, T., et al., *Effect of sintering temperature on Li diffusivity in Li0.29La0.57TiO3: Local hopping and long-range transport.* Solid State Ionics, 2020. **357**: p. 115486.

21. Ibarra, J., et al., *Influence of composition on the structure and conductivity of the fast ionic conductors La2/3– xLi3xTiO3 (0.03≤ x≤ 0.167).* Solid State Ionics, 2000. **134**(3-4): p. 219-228.

22. Tilley, R.J.D.Q.T.R.J.D., *Perovskites : structure-property relationships*. First edition.. ed. 2016, Chichester, West Sussex, United Kingdom: Chichester, West Sussex, United Kingdom : : Wiley. 1 online resource (330 p.).

23. Stramare, S., V. Thangadurai, and W. Weppner, *Lithium Lanthanum Titanates: A Review.* Chemistry of Materials, 2003. **15**(21): p. 3974-3990.

24. Mahato, N., et al., *Progress in material selection for solid oxide fuel cell technology: A review.* Progress in Materials Science, 2015. **72**: p. 141-337.

25. Sun, C., R. Hui, and J. Roller, *Cathode materials for solid oxide fuel cells: a review.* Journal of Solid State Electrochemistry, 2010. **14**(7): p. 1125-1144.

26. Sun, Y., et al., *Recent Progress in Lithium Lanthanum Titanate Electrolyte towards All Solid-State Lithium Ion Secondary Battery.* Critical Reviews in Solid State and Materials Sciences, 2019. **44**(4): p. 265-282.

27. Yan, S., et al., *Perovskite Solid-State Electrolytes for Lithium Metal Batteries.* Batteries, 2021. **7**(4): p. 75.

28. Korthauer, R.Q.R., *Lithium-Ion Batteries: Basics and Applications*. 2018, Berlin Heidelberg: Berlin : Heidelberg : Springer Berlin Heidelberg : Imprint: Springer. 1 Online-Ressource (XX, 413 Seiten), 228 Illustrationen, 18 Illustrationen.

29. Warner, J.T., *Lithium-ion battery chemistries: a primer*. 2019: Elsevier.

30. Korthauer, R.Q.K.R., *Lithium-Ion Batteries: Basics and Applications*. 2018, Berlin Heidelberg: Berlin : Heidelberg : Springer Berlin Heidelberg : Imprint: Springer. 1 Online-Ressource (XX, 413 Seiten), 228 Illustrationen, 18 Illustrationen.

31. Famprikis, T., et al., *Fundamentals of inorganic solid-state electrolytes for batteries.* Nature materials, 2019. **18**(12): p. 1278-1291.

32. Zheng, F., et al., *Review on solid electrolytes for all-solid-state lithium-ion batteries.* Journal of Power Sources, 2018. **389**: p. 198-213.

33. Nazri, G.-A. and G. Pistoia, *Lithium batteries: science and technology*. 2008: Springer Science & Business Media.

34. Scrosati, B., F. Croce, and L. Persi, *Impedance spectroscopy study of PEO-based nanocomposite polymer electrolytes.* Journal of the Electrochemical Society, 2000. **147**(5): p. 1718.

35. Yu, X., et al., *A stable thin-film lithium electrolyte: lithium phosphorus oxynitride.* Journal of the electrochemical society, 1997. **144**(2): p. 524.

36. Harada, Y., et al., *Lithium ion conductivity of polycrystalline perovskite La0. 67–xLi3xTiO3 with ordered and disordered arrangements of the A-site ions.* Solid State Ionics, 1998. **108**(1-4): p. 407-413.

37. Bernuy-Lopez, C., et al., *Atmosphere controlled processing of Ga-substituted garnets for high Li-ion conductivity ceramics.* Chemistry of materials, 2014. **26**(12): p. 3610-3617.

38. Porz, L., et al., *Mechanism of lithium metal penetration through inorganic solid electrolytes.* Advanced Energy Materials, 2017. **7**(20): p. 1701003.

39. Zhu, Y., X. He, and Y. Mo, *Origin of Outstanding Stability in the Lithium Solid Electrolyte Materials: Insights from Thermodynamic Analyses Based on First-Principles Calculations.* ACS Applied Materials & Interfaces, 2015. **7**(42): p. 23685-23693.

40. Hitz, C.B.Q.C.B., *Introduction to laser technology*. 4th . ed, ed. J.Q.J. Hecht and J.J.Q.J.J. Ewing. 2012, Hoboken [New Jersey]

[Piscataqay, New Jersey]: Hoboken [New Jersey] : : John Wiley and Sons, [Piscataqay, New Jersey] : : IEEE Xplore. 1 online resource (312 p.).

41. Taylor, T.S.Q.T.S., *Introduction to laser science and engineering*. First edition. ed. 2020, Boca Raton, FL: Boca Raton, FL : CRC Press/Taylor & Francis Group. 1 Online-Ressource.

42. Eichler, H.J.Q.E.H.J., *Laser : Bauformen, Strahlführung, Anwendungen*. 8., aktualisierte u. überarb. Aufl. 2015. ed, ed. J.Q.E.J. Eichler. 2015, Berlin, Heidelberg: Berlin, Heidelberg : Springer Berlin Heidelberg : Imprint: Springer Vieweg. 1 Online-Ressource (XI, 491 S. 297 Abb).

43. Sigrist, M.W.Q.S.M.W., *Laser : Theorie, Typen und Anwendungen*. 8. Auflage. ed. 2018, Berlin: Berlin : Springer Spektrum. 1 Online-Ressource (XVI, 452 Seiten), Illustrationen.

44. Ammann, A.A., *Inductively coupled plasma mass spectrometry (ICP MS): a versatile tool.* Journal of mass spectrometry, 2007. **42**(4): p. 419-427.

45. Worthy, A.N. *The 30-Minute Guide to ICP-MS*. 2001.

46. Gałązka, R., *MODERN ANALYTICAL METHODS IN ENVIRONMENTAL ANALYSIS – ICP-MS TECHNIQUE*. 2011.

47. Nelms, S.Q.S., *Inductively coupled plasma mass spectrometry handbook*. 2005, [Place of publication not identified]: [Place of publication not identified] : Blackwell.

48. Thomas, R.Q.R., *Practical guide to ICP-MS : a tutorial for beginners*. 3. . ed. Practical spectroscopy. 2013, Boca Raton, Fla. [u.a.]: Boca Raton, Fla. [u.a.] : CRC Press. XXVII, 418 S., Ill., graph. Darst., 24 cm.

49. Günther, D. and B. Hattendorf, *Solid sample analysis using laser ablation inductively coupled plasma mass spectrometry.* TrAC Trends in Analytical Chemistry, 2005. **24**(3): p. 255-265.

50. Russo, R.E., et al., *Laser ablation in analytical chemistry—a review.* Talanta, 2002. **57**(3): p. 425-451.

51. Bubert, H.Q.B.H., *Surface and Thin Film Analysis : A Compendium of Principles, Instrumentation and Applications*. 2nd . ed, ed. H.Q.J.H. Jenett. 2011, Hoboken: Hoboken : : Wiley. 1 online resource (559 p.).

52. Limbeck, A., et al., *Recent advances in quantitative LA-ICP-MS analysis: challenges and solutions in the life sciences and environmental chemistry.* Analytical and bioanalytical chemistry, 2015. **407**(22): p. 6593-6617.

53. Qian, D., et al., *Lithium lanthanum titanium oxides: a fast ionic conductive coating for lithium-ion battery cathodes.* Chemistry of Materials, 2012. **24**(14): p. 2744-2751.